

Fabrication, Characterization, and Investigation into the Wear Behavior of  
NiTi-based Nanolaminate Coatings

by

Nicole Cameron

Submitted in partial fulfilment of the requirements  
for the degree of Master of Applied Science

at

Dalhousie University  
Halifax, Nova Scotia  
August 2019

© Copyright by Nicole Cameron, 2019

# Table of Contents

<i>Table of Contents</i> .....	<i>ii</i>
<i>List of Tables</i> .....	<i>v</i>
<i>List of Figures</i> .....	<i>vi</i>
<i>Abstract</i> .....	<i>xi</i>
<i>List of Abbreviations Used</i> .....	<i>xii</i>
<i>Acknowledgments</i> .....	<i>xiii</i>
<b>1.0 Introduction</b> .....	<b>1</b>
<b>1.1 Objectives</b> .....	<b>2</b>
<b>2.0 Literature Review</b> .....	<b>4</b>
<b>2.1 NiTi Shape Memory Alloys</b> .....	<b>4</b>
2.1.1 NiTi Phase .....	4
2.1.2 Reversible Phase Transformation .....	6
2.1.3 Shape Memory Effect.....	9
2.1.4 Superelasticity Effect.....	10
<b>2.2 Production of NiTi</b> .....	<b>12</b>
2.2.1 Ni-Ti Diffusion Couples.....	12
2.2.2 NiTi Powder Metallurgy.....	14
2.2.3 NiTi Surface Coatings .....	17
2.2.4 Factors Influencing NiTi Formation .....	19
<b>2.3 Contact and Fracture Mechanics</b> .....	<b>23</b>
2.3.1 Hertzian Contact.....	23
2.3.2 Multilayered Structures .....	27
<b>2.4 Wear Behavior</b> .....	<b>28</b>
2.4.1 Monolithic Materials .....	29
2.4.2 Multilayered Materials .....	33
2.4.3 Wear Behavior of NiTi Alloys .....	35
<b>3.0 Experimental Procedure</b> .....	<b>38</b>

<b>3.1</b>	<b>Fabrication of the Coatings .....</b>	<b>38</b>
<b>3.2</b>	<b>Microstructural Characterization of Coatings .....</b>	<b>40</b>
<b>3.3</b>	<b>Nanoindentation Testing.....</b>	<b>43</b>
<b>3.4</b>	<b>Scratch Testing .....</b>	<b>45</b>
<b>3.5</b>	<b>Hertzian-Type Testing .....</b>	<b>47</b>
<b>3.6</b>	<b>Single Particle Erosion Testing .....</b>	<b>48</b>
<b>4.0</b>	<b><i>Results and Discussion .....</i></b>	<b><i>51</i></b>
<b>4.1</b>	<b>Fabrication and Characterization of Coatings .....</b>	<b>51</b>
4.1.1	Design and Fabrication of the NiTi Nanolaminate Coatings .....	51
4.1.2	XRD of Nanolaminate Coatings .....	53
4.1.3	Characterization of Monolayered NiTi Coating .....	60
4.1.4	Nanoindentation Hardness and Elastic Modulus of the Coatings .....	62
<b>4.2</b>	<b>Scratch Behavior of the Coatings.....</b>	<b>68</b>
4.2.1	Single Pass Fracture Mechanisms .....	69
4.2.2	Multiple Passes Fracture Mechanisms.....	73
4.2.3	Increasing Load Scratch Test .....	78
<b>4.3</b>	<b>Hertzian-Type Indentation .....</b>	<b>81</b>
4.3.1	Fracture Mechanisms Under Hertzian-Type Indentation .....	83
4.3.2	Cracking Events.....	85
<b>4.4</b>	<b>Single Particle Impact Erosion.....</b>	<b>87</b>
4.4.1	High-Angle Fracture Mechanisms.....	88
4.4.2	Low-Angle Fracture Mechanisms .....	90
4.4.3	Erosion Mechanisms .....	92
<b>4.5</b>	<b>Dent Resistance Comparative Analysis .....</b>	<b>97</b>
<b>5.0</b>	<b><i>Conclusion.....</i></b>	<b><i>100</i></b>
<b>5.1</b>	<b>Summary .....</b>	<b>100</b>
<b>5.2</b>	<b>List of Publications From This Work.....</b>	<b>101</b>
<b>5.3</b>	<b>Future Research.....</b>	<b>101</b>
<b>6.0</b>	<b><i>References .....</i></b>	<b><i>102</i></b>

<b>7.0</b>	<b><i>Appendix A – Nanoindentation Data</i></b> .....	<b>113</b>
<b>8.0</b>	<b><i>Appendix B – Scratch Test Scars</i></b> .....	<b>116</b>
<b>9.0</b>	<b><i>Appendix C – Hertzian Type Indents</i></b> .....	<b>118</b>
<b>10.0</b>	<b><i>Appendix D – Single Particle Erosion</i></b> .....	<b>119</b>

## **List of Tables**

Table 4.1 – ICP composition of as-sputtered laminate coatings.....	52
Table 4.2 – Material properties of individual layers in the laminate and substrate .....	57
Table 4.3 – Mean contact pressure during scratch testing.....	68
Table 4.4 – Hertzian indentation mean pressure.....	83
Table 4.5 – Single particle impact mean contact pressure.....	87

## List of Figures

Figure 2.1 – Ni and Ti phase diagram [12].....	5
Figure 2.2 – NiTi crystal structures a) austenite b) martensite [15] .....	6
Figure 2.3 – Temperature-induced phase transformation without mechanical loading [7] 7	
Figure 2.4 – Three transformation paths in Ti – Ni-based alloys [14] .....	8
Figure 2.5 – Schematic of the shape memory effect of an SMA showing the detwinning of the material with applied stress [7].....	9
Figure 2.6 – Shape memory effect transformation path [20].....	10
Figure 2.7 – Superelasticity effect transformation path [7] .....	11
Figure 2.8 – Back-scattered electron micrograph of products layers of sample reacted at 650°C for 8 hours with a current density of 1527 A cm <sup>-2</sup> [35] .....	13
Figure 2.9 – SEM micrographs of Ni-Ti interface under different temperatures [30] .....	14
Figure 2.10 – SEM micrograph of the specimen sintered at 800°C for 3 hours [38] .....	15
Figure 2.11 – SEM images of the specimen sintered from the Ni-Ti compact at (a) 900°C, (b) enlarged square area in (a) [39].....	16
Figure 2.12 – Backscattered SEM micrographs and EDS analysis of the phases of specimens sintered at different temperatures: a and b 750 C for 6 hours [40] .....	16
Figure 2.13 – TEM image and diffraction patterns of as-sputtered Ni and Ti multilayers thin films (1). (a) bright field TEM image, (b) the corresponding selected area diffraction pattern, and (c) NBD pattern of the cross-section including the Ti and Ni layers [37]....	18
Figure 2.14 – TEM image and diffraction patterns of Ni and Ti multilayers thin films annealed at 750K (1); (a) bright field TEM image, (b) the corresponding selected area diffraction pattern [37].....	19
Figure 2.15 – Schematic illustration of the Kirkendall’s experiment [47] .....	20
Figure 2.16 – Movement of the inert markers with the increase in annealing time, where $t_2 > t_1 > t = 0$ [47].....	21
Figure 2.17 – Illustration of a) coherent b) semi-coherent and c) incoherent interfaces [57].....	22
Figure 2.18 – Hertzian cone model [60] .....	24

Figure 2.19 – Morphology of a) radial b) lateral c) median and d) half-penny cracks [58]	27
Figure 2.20 – Theory of delamination wear [72]	28
Figure 2.21 – Adhesive wear [75]	29
Figure 2.22 – Abrasion wear a) cutting b) fracture c) fatigue d) grain pull-out [78]	31
Figure 2.23 – Erosion mechanisms by a) abrasion b) fatigue and c) plastic deformation [78]	32
Figure 2.24 – Wear rates behavior for a) ductile and b) brittle materials [78]	33
Figure 2.25 – Composite wear behavior a) bridging, b) deflection and c) transformation toughening mechanisms [70]	34
Figure 3.1 – Schematic of the sputtering process	38
Figure 3.2 – Schematic of Ni/Ti nanolaminate	39
Figure 3.3 – R.D. Webb vacuum furnace	40
Figure 3.4 – Buelher IsoMet 1000 precision saw	41
Figure 3.5 – Bruker D8 advanced x-ray diffraction system	42
Figure 3.6 – Principles of x-ray diffractometry stress measurement at an angle of a) $0^\circ$ and b) $\psi = \psi$ [103]	43
Figure 3.7 – Typical nanoindentation load-depth curve [105]	44
Figure 3.8 – Scratch test apparatus	46
Figure 3.9 – Hertzian- type indentation apparatus	48
Figure 3.10 – Single particle erosion apparatus	49
Figure 3.11 – Calibration curve of single particle erosion tester	50
Figure 4.1 – HiM image of the as-sputtered coating	52
Figure 4.2 – Mixed EDS map of nanolaminate coating annealed at $650^\circ\text{C}$	53
Figure 4.3 – XRD patterns of as-sputtered and annealed nanolaminate coatings and substrate	54
Figure 4.4 – Slow XRD scans of a) $650^\circ\text{C}$ and b) $800^\circ\text{C}$ nanolaminate coatings	55
Figure 4.5 – Equivalent stresses as a function of annealing temperature	56
Figure 4.6 – EDS composition of $650^\circ\text{C}$ nanolaminate	58
Figure 4.7 – Schematic of the diffusion process of Ni and Ti	59
Figure 4.8 – SEM cross-sections images of a) as-sputtered and b) $650^\circ\text{C}$	59

Figure 4.9 – SEM cross-section image of superelastic NiTi monolayer coating.....	60
Figure 4.10 – XRD patterns of monolayered superelastic NiTi and steel substrate .....	61
Figure 4.11 – Surface roughness of the nanolaminate and monolayer of NiTi coatings..	62
Figure 4.12 – Nanoindentation curves for a) as-sputtered b) 650°C c) 800°C d) superelastic NiTi coatings.....	63
Figure 4.13 – Hardness data for a) as-sputtered b) 650°C c) 800°C and d) superelastic NiTi coatings.....	64
Figure 4.14 – Elastic moduli data for a) as-sputtered b) 650°C c) 800°C and d) superelastic NiTi coatings.....	65
Figure 4.15 – Hardness and elastic modulus values at a depth of 200nm .....	66
Figure 4.16 – Elastic recovery and E/H ratios .....	67
Figure 4.17 – $H^3/E^2$ ratio of the coatings .....	68
Figure 4.18 – 2kgf a) as-sputtered b) 150°C and c) 500°C scars .....	70
Figure 4.19 – 2kgf scars of a) 650 °C b) 800 °C and c) superelastic NiTi coating.....	71
Figure 4.20 – Transformation toughening in laminate structures.....	72
Figure 4.21 – Constant load a) mean COF values and b) volume loss for nanolaminate coatings and superelastic NiTi monolayer.....	73
Figure 4.22 – Sliding distance 25mm a) as-sputtered b) 150°C c) 500°C scars .....	74
Figure 4.23 – Sliding distance of 25mm of a) 650 °C b) 800 °C and c) superelastic NiTi coating.....	75
Figure 4.24 – Multiple passes of a 1kgf load mean COF values for nanolaminate and monolayer superelastic NiTi coatings.....	76
Figure 4.25 – Wear rates of nanolaminates and superelastic NiTi coating .....	77
Figure 4.26 – E/H and elastic recovery ratios influence on wear rates.....	78
Figure 4.27 – Load at first crack.....	79
Figure 4.28 – Acoustic emission signal from the coatings .....	80
Figure 4.29 – XRD of a) 650 °C and b) 800°C nanolaminates before and after scratch testing.....	81
Figure 4.30 – R/a ratios for nanolaminate and monolayered coatings .....	82
Figure 4.31 – 1000N indent of a) as-sputtered b) 150°C and c) 500°C annealed nanolaminate coatings.....	84

Figure 4.32 – Schematic of delamination occurring in the coating .....	84
Figure 4.33 – 1000N indent of a) 650 °C b) 800°C annealed nanolaminate coatings and c) superelastic monolayer of superelastic NiTi coating .....	85
Figure 4.34 – 1000N load-displacement curves for a) as-sputtered b) 150°C c) 500°C d) 650°C e) 800°C nanolaminate coating and f) monolayered superelastic NiTi coating.....	86
Figure 4.35 – Single particle 90-degree impact a) as-sputtered b) 150°C and c) 500°C nanolaminate coating .....	88
Figure 4.36 – Single particle 90-degree impact a) 650°C b) 800°C and c) monolayer of NiTi coating .....	89
Figure 4.37 – Impact site of 650 °C nanolaminate a) SEM and b) EDS map of 90° impact .....	90
Figure 4.38 – Single particle 30-degree impact a) as-sputtered b) 150°C and c) 500°C nanolaminate coating .....	91
Figure 4.39 – Single particle 90-degree impact a) 650°C b) 800°C and c) monolayer of NiTi coating .....	92
Figure 4.40 – Nanolaminate annealed at 150°C impact profiles at 90° a) confocal image b) depth profile and 30° impacts c) confocal image and d) depth profile.....	93
Figure 4.41 – WC ball used to impact as-sputtered coating .....	94
Figure 4.42 – Superelastic NiTi monolayer coating impact profiles at 90° a) confocal image b) depth profile and 30° impacts c) confocal image and d) depth profile .....	95
Figure 4.43 – Nanolaminate annealed at 650°C impact profiles at 90° a) confocal image b) depth profile and 30° impacts c) confocal image and d) depth profile.....	96
Figure 4.44 – Volume loss at different impact angles for all coatings .....	97
Figure 4.45 – 1500N indents of a) Ni-P [124] b) hard chromium [123] and c) 650°C annealed nanolaminate coatings .....	98
Figure 7.1 – As-sputtered load-depth curves .....	113
Figure 7.2 – 650°C load-depth curves.....	113
Figure 7.3 – 800°C load-depth curves.....	114
Figure 7.4 – Superelastic NiTi load-depth curves .....	114
Figure 7.5 – Elastic Modulus values for as-sputtered, 650°C, and 800 °C nanolaminates and superelastic NiTi monolayer .....	115

Figure 7.6 – Hardness values for as-sputtered, 650°C, and 800°C nanolaminates and superelastic NiTi monolayer .....	115
Figure 7.7 – Single pass scars .....	116
Figure 7.8 – Multiple pass scars .....	117
Figure 7.9 – Hertzian indentations.....	118
Figure 7.10 – Single particle impact sites.....	119

## **Abstract**

NiTi is a shape memory alloy possessing a stress-induced reversible martensitic transformation. NiTi alloys are used in a variety of industrial applications, however, is prevalent in the automotive, aerospace, and medical sectors. The main challenge of using NiTi is its poor machinability and formability. Applying NiTi as a surface coating may be an alternate manufacturing method that will require limited machining. The objective of this study is to produce a superelastic NiTi surface coating that still possesses excellent wear and dent resistance while reducing forming and machining processes. Ni and Ti were sputtered deposited in layers and annealed to form the NiTi intermetallic phase. NiTi coating was also fabricated through the sputtered deposition of a superelastic NiTi monolayer. The wear behavior of the coatings was studied through scratch, Hertzian-type indentation, and single particle erosion testing. Residual stress and XRD analysis suggest that superelastic NiTi phase precipitated at elevated temperatures which resulted in the excellent dent, scratch, and erosion resistance compared to as-deposited Ni/Ti nanolaminate coating. The as-sputtered, 650°C, and 800°C nanolaminate coatings and the monolayer of superelastic NiTi were further subjected to nanoindentation testing. This showed that the elastic modulus to hardness ratio and wear resistance of the nanolaminate annealed at 650°C is comparable to the sputtered superelastic NiTi monolayer coating. Furthermore, the annealed nanolaminate coating is found to exhibit higher hardness than the monolayered NiTi and comparable dent resistance. The present findings reveal the superiority of the 650°C annealed nanolaminate NiTi coating over the monolayer NiTi. This study has shown that superelastic NiTi can be produced by annealing Ni and Ti nanolaminates having excellent protective properties in applications where high wear damage is expected.

## List of Abbreviations Used

$A_s/A_f$	Austenitic Start and Finish Temperature
AE	Acoustic Emission
COF	Coefficient of Friction
CTE	Coefficient of Thermal Expansion
E	Elastic Modulus
EDS	Energy Dispersive Spectrometry
H	Hardness
HiM	Helium ion Microscope
ICP-OES	Inductively Coupled Plasma Optical Emission Spectrometry
$M_s/M_f$	Martensite Start and Finish Temperature
PVD	Physical Vapor Deposition
SEM	Scanning Electron Microscope
SIM	Stress-Induced Martensitic Phase Transformation
SMA	Shape Memory Alloy
XRD	X-Ray Diffractometry

## **Acknowledgments**

I would like to thank my supervisor, Professor Dr. Zohier Farhat, director of the Advanced Tribology Laboratory (ATL) for his guidance and mentorship throughout the duration of this degree. I would also like to acknowledge the past and current ATL members for the continuous support. Finally, I am greatly indebted to my friends and family – those who have suffered the most.

I would also like to express my gratitude to those that have aided me in the success of this degree. My graduate study supervisory committee, Dr. Paul Bishop and Dr. Hany El Naggari, and the administrative secretary, Kate Hide. Also, my sincerest thanks to the technicians at Dalhousie University: Patricia Scallion, Peter Jones, Albert MacDonald, Angus MacPherson, and Mark MacDonald.

Lastly, this study was made possible due to the financial support from the Natural Sciences and Engineering Research Council of Canada (NSERC). The findings are herein are solely the responsibility of the authors.

Nicole Cameron

August 2019

## 1.0 Introduction

The wear of components costs industries millions of dollars each year. The effects of wear can lead to a loss of process efficiency, plant shutdowns, and safety risks [1]; ultimately causing production delays which result in a significant increase in costs. A common method to prevent erosion and wear is to protect the material by applying a surface coating. To be effective, this coating must have the ability to withstand impacting, denting, and eroding forces to be considered wear-resistant. These types of coatings are commonly found in the aerospace, oil and gas, medical, and automotive industries.

Metallic materials such as nickel, cobalt, and chromium have been extensively researched as wear-resistant coatings due to their high hardness [2], [3]; however, a higher hardness also causes the coating to behave in a brittle manner. The key parameter into evaluating the wear resistance of a material is its elastic modulus to hardness ratio; which accounts for resilience and toughness of the material [4]. A material with a low elastic modulus can withstand more strain, which results in an effective wear-resistant coating [5]. Suggesting both hardness and elastic modulus influence the wear resistance of a material.

Chromium coatings are often found in aerospace applications because of the high hardness they possess, however, a higher hardness comes with low ductility. Industries have been searching for a replacement for electroplated chromium coatings as they are fabricated in a solution that produces hexavalent chromium [Cr(VI)] which poses a significant environmental and health risk [6]. Thus, creating a need to develop an alternative coating that has comparable wear resistance and is resilient.

An alloy that has not been fully exploited for wear-resistant purposes in industrial applications is bulk NiTi. Despite this, equiatomic NiTi is proven to have high strength and excellent wear resistance that surpasses that of steels, cobalt-based, and nickel-based alloys [2], [3]. NiTi can undergo a stress-induced reversible martensitic phase transformation [7]; which prohibits crack propagation that minimizes the overall damage

to the coating [8]. However, bulk NiTi is generally not desired in many applications because of its poor formability and machinability [9]. To be exploited in commercial applications, the production method of NiTi must limit the amount of machining required.

An alternative fabrication method is to deposit NiTi as a surface coating; thus, reducing the amount of machining. Vacuum deposition processes have been used with varying successes; despite this, there is no commercial method to deposit NiTi as a surface coating. Sputtering of superelastic NiTi is extremely sensitive to metallurgical factors and sputtering conditions such as alloy composition, contamination, and gas pressure [10]; a slight change could result in the absence of the superelasticity effect. Additionally, the fabrication of the superelastic NiTi target used in the sputtering process will require non-traditional machining methods, which are costly. The complex and difficult process of depositing NiTi further restricts its applicability in industries. However, it was found that NiTi can be attained through the annealing of Ni and Ti diffusion couples. The main challenge associated with solid-state diffusion of Ni and Ti is controlling the formation and growth of the NiTi phase. Currently, a full and comprehensive understanding of the formation of the superelastic NiTi phase during coating development is non-existent.

## **1.1 Objectives**

The objectives of this research are as follows:

- Produce a superelastic NiTi surface coating by subjecting sputtered deposited layers of Ni and Ti to a heat treatment process, promoting the solid-state diffusion to form a NiTi layer;
- Perform an in-depth and comprehensive microstructural and property assessment of the coatings;
- Investigate the scratch resistance of the coatings to determine the wear mechanisms that occur during sliding wear;

- Assess the cracking behavior and dent resistance of the coatings through Hertzian-type indentation;
- Conduct single particle erosion testing to determine the erosion trends that occur in the coatings;
- Validate the behavior of the Ni-Ti nanolaminates by comparing them to other wear resistant coatings (i.e. chromium-based, nickel-based).

Applying NiTi as a surface coating allows for a machinable substrate to be formed prior to the coating and annealing processes; accordingly, this will limit the amount of machining required. The nanolaminate coating can be a viable option for components that experience a high rate of wear in industrial and commercial applications. NiTi coatings have the potential to provide wear resistance to steels in oil and gas fields in components such as pipelines, pumps, impellers, joints, couples, and pipe bends. Applications of a NiTi coating could even potentially expand into the aerospace industry where components such as rotors, compressor blades, landing gears, hydraulic components, and bearings are made of titanium-based alloys.

## **2.0 Literature Review**

### **2.1 NiTi Shape Memory Alloys**

Shape memory alloys (SMA) exhibit two unique characteristics; the shape memory effect and the superelastic effect. These effects make SMA ideal for applications such as sensing and actuation, impact absorption, and vibration damping [7]. There are numerous shape memory alloys, however, the most researched is equiatomic NiTi. NiTi was first discovered by Buehler *et al.* [11] in the Naval Ordnance Laboratory in California, while testing materials for heat-shielding applications.

#### ***2.1.1 NiTi Phase***

The NiTi intermetallic phase is located in the equiatomic region of the nickel-titanium phase diagram, as seen in Figure 2.1. There are three equilibrium intermetallic phases that can form within the Ni-Ti system, which are NiTi<sub>2</sub>, NiTi, and Ni<sub>3</sub>Ti. However, the superelasticity and shape memory effects are exclusively found within the NiTi phase.

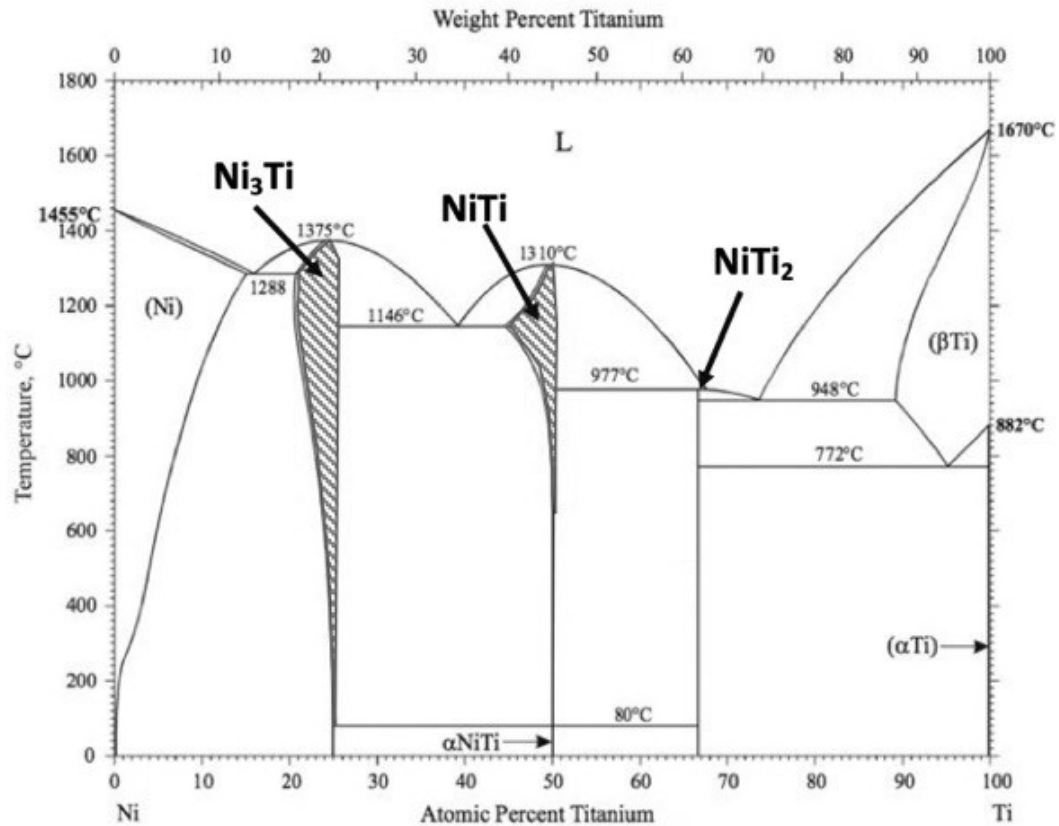


*Figure 2.1 – Ni and Ti phase diagram [12]*

Shape memory alloys typically have a high-temperature austenite phase and low-temperature martensite phase. Occasionally, in NiTi alloys, there is an additional intermediate R-phase that can occur. These phases are further defined below.

- **Austenite** – has a B2 (CsCl) crystal structure with a lattice parameter of 0.3015nm at room temperature [13], [14]. The CsCl structure is shown in Figure 2.2(a), where the Ti atom (red) is surrounded by Ni atoms (blue) [15]. This phase exists at a higher temperature in relation to the other phases, otherwise known as a parent phase. The austenite phase plays a fundamental role in the stressed induced superelasticity and shape memory effects.
- **Martensite** – is polymorphic and the structure can change depending on the temperature [7]. There are two crystal structures of martensite a orthorhombic

B19 phase and a trigonal or monoclinic B19' phase. It was found by Heheman *et al.* [16] that the B19' phase is a result of cooling binary NiTi alloys from solution treatment. The crystal structure of B19' in martensite can be seen in Figure 2.2(b) where Ni atoms are blue and Ti are red [15].

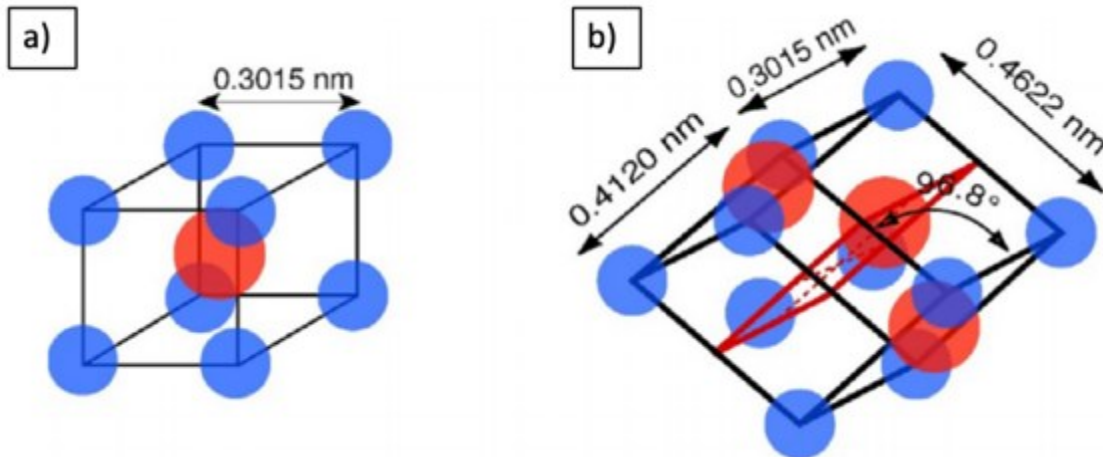


**Figure 2.2 – NiTi crystal structures a) austenite b) martensite [15]**

- **R-Phase** – exhibits a trigonal phase that can appear in the transformation from austenite to martensite [12]. The R-phase will typically occur when there is an increase in nickel concentration or in the presence of crystal defects such as coherent, nonequilibrium  $\text{Ni}_3\text{Ti}_4$  precipitates [17], [18]. Zamponi *et al.* [19] found that the R-phase appears when NiTi is heat treated below  $500^\circ\text{C}$  and its existence supports the stress-induced martensite phase transformation.

### 2.1.2 Reversible Phase Transformation

The superelasticity and shape memory effect is directly influenced by the reversible phase transformation. Upon cooling of a SMA, in the absence of an external force or stress, the austenite phase will begin to transform into twinned martensite, as seen in Figure 2.3. The martensitic start temperature ( $M_s$ ) indicates that the austenite will begin to transform, and the transformation will be complete with the temperature reaches the martensitic finish temperature ( $M_f$ ). The transformation from austenite to martensite

occurs by shear lattice distortion, not through diffusion mechanisms [7]. Likewise, when heating under a zero load, the martensite phase will begin to transform back to its parent phase at the austenitic start temperature ( $A_s$ ) and the material will be in its austenitic state when the temperature surpasses the austenitic finish temperature ( $A_f$ ).

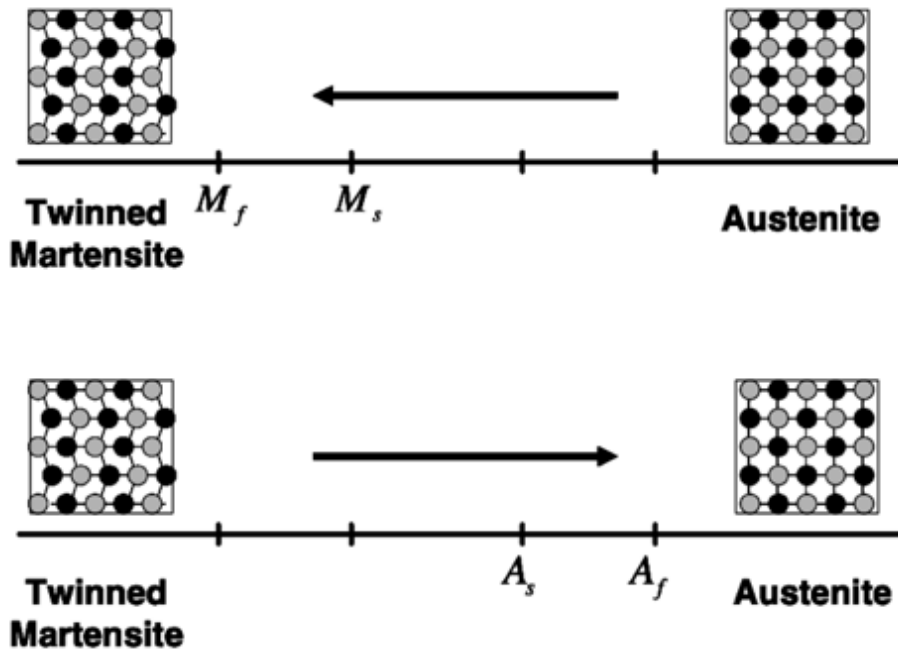


*Figure 2.3 – Temperature-induced phase transformation without mechanical loading [7]*

In NiTi alloys, the main transformation path, when cooling, is the direct austenitic NiTi (B2) phase transforming to martensitic NiTi (B19') phase. Depending on the alloy composition and heat-treatment processes, an intermediate step could occur; especially, if the alloy has a low  $M_s$  transformation temperature below 0K [14]. These transformation paths are illustrated in Figure 2.4. The intermediate B19 (orthorhombic) step will usually occur when NiTi is alloyed with copper. The intermediate R-phase (trigonal) will occur if Fe is alloyed with NiTi or if a NiTi alloy undergoes an aging process. The transformation path between austenite and martensite is critical to both the superelasticity and the shape memory effects.

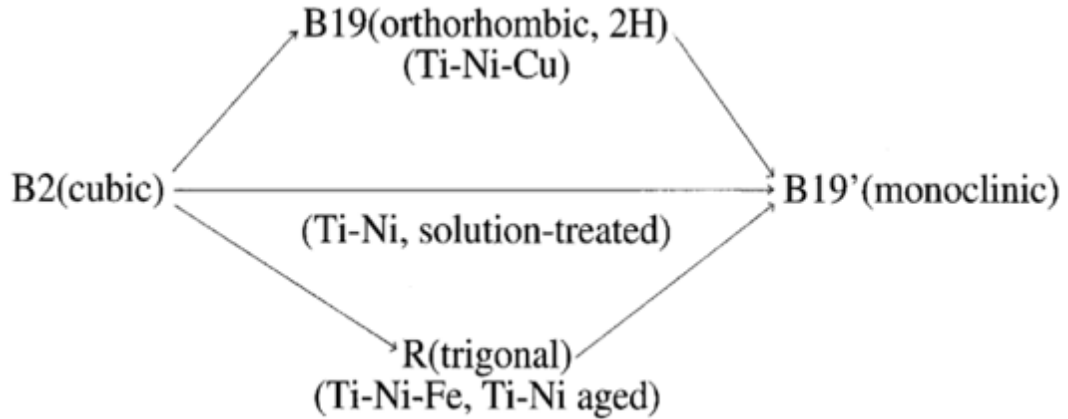


*Figure 2.4 – Three transformation paths in Ti – Ni-based alloys [14]*

Since the phase transformation is a diffusionless process, the atoms in the martensitic phase can have various arrangements; these different arrangements are called variants. For example, in NiTi alloys, the martensite phase can have up to 24 variants [7]. There are two main forms of variants: twinned and detwinned. The twinned variant is a “self-accommodated” arrangement and the detwinned variant occurs when a specific arrangement dominates [7]. Variants can be altered under an applied load, which is seen in Figure 2.5. When a load is applied to the twinned martensitic phase, it rearranges the atoms into a detwinned variant. The variant that martensite takes will directly influence the superelasticity and shape memory transformation paths.

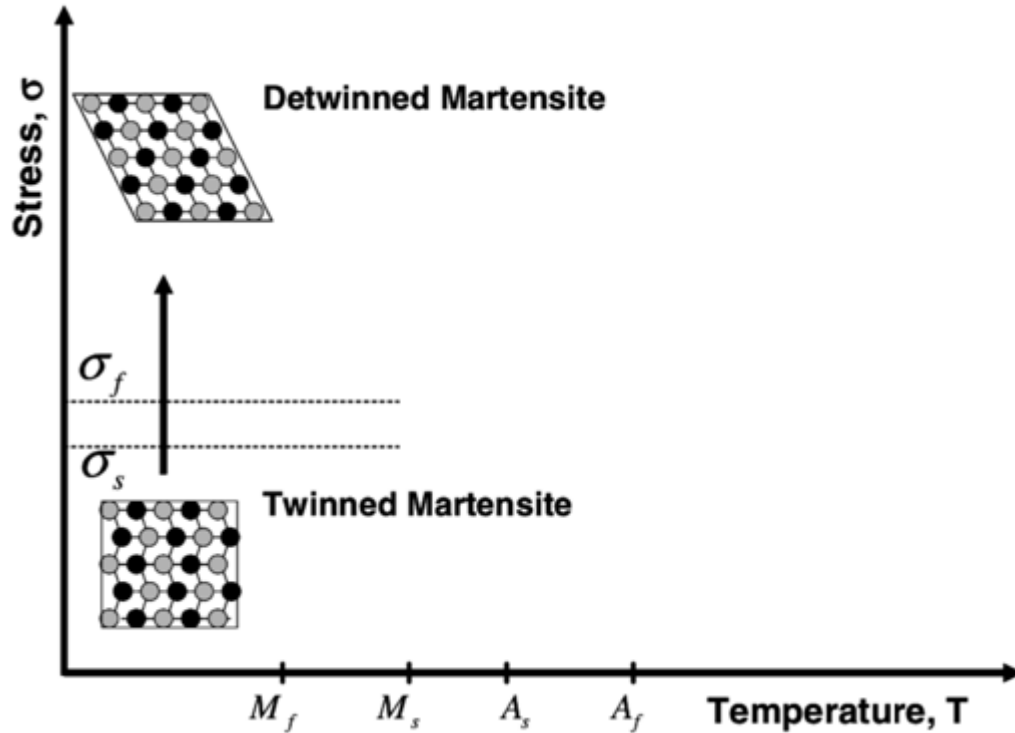


*Figure 2.5 – Schematic of the shape memory effect of an SMA showing the detwinning of the material with applied stress [7]*

### **2.1.3 Shape Memory Effect**

The transformation path of a shape memory effect in a SMA is depicted in Figure 2.6. Initially, the SMA will be present in its austenitic phase (i.e. above  $A_f$  temperature) and is cooled below the  $M_f$  temperature, fully transforming for the material to be in its twinned martensite phase. An external stress needs to be applied to the twinned martensite phase to prompt the rearrangement to detwinned martensite [20]. To recover its original shape the detwinned martensite should be heated above the  $A_f$  temperature, which will prompt the reversible phase transformation to austenite [7]. If the material is then cooled below  $M_f$  temperature, it can be deformed, and the process can continue.

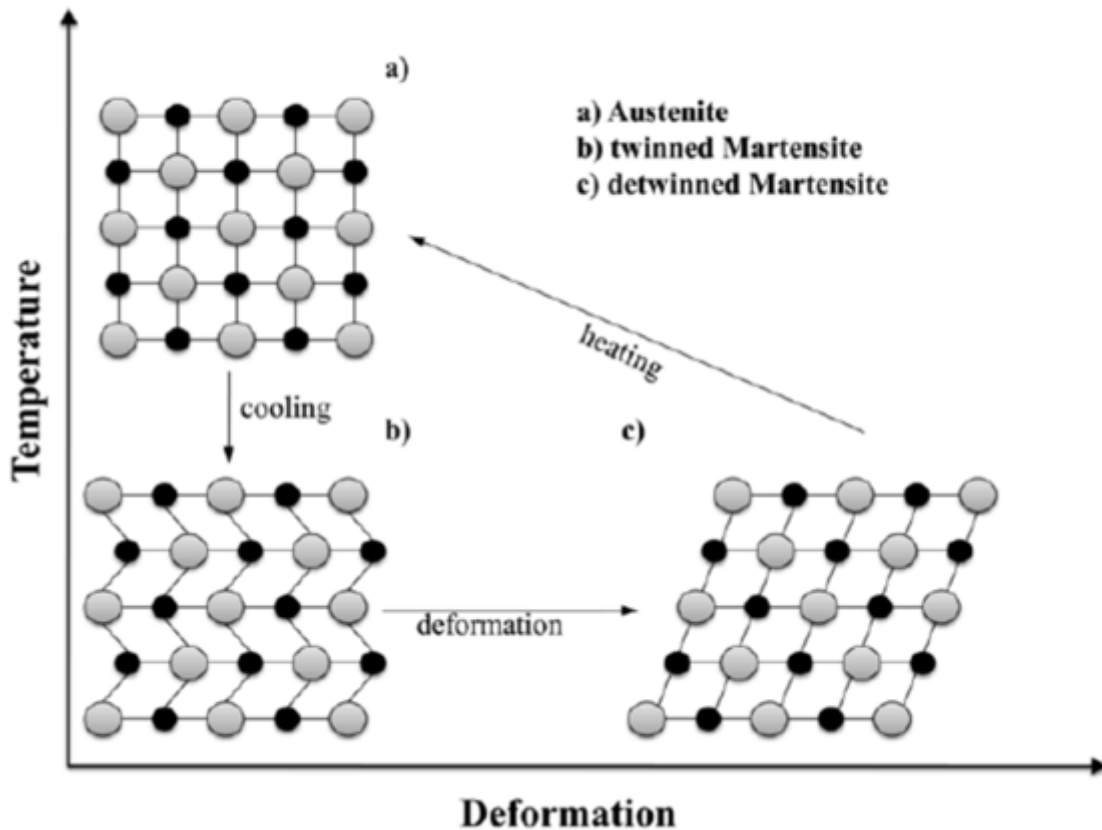


Figure 2.6 – Shape memory effect transformation path [20]

#### 2.1.4 Superelasticity Effect

The transformation path for a superelastic SMA is illustrated in Figure 2.7. Initially, the SMA will be in its austenitic phase, when an external stress is applied and surpasses the  $\sigma^{Ms}$ , the material will undergo the stress-induced martensite phase transformation (SIM) to detwinned martensite [21]. The transformation is complete when the applied stress surpasses  $\sigma^{Mf}$ . Upon unloading the stress, the reverse phase transformation back to austenite will start when the stress is below that of  $\sigma^{As}$  and can be complete when the stress is below  $\sigma^{Af}$ . Noting that this transformation occurs without any external thermal changes within the system, indicating that the superelasticity effect is independent of the ambient temperature.

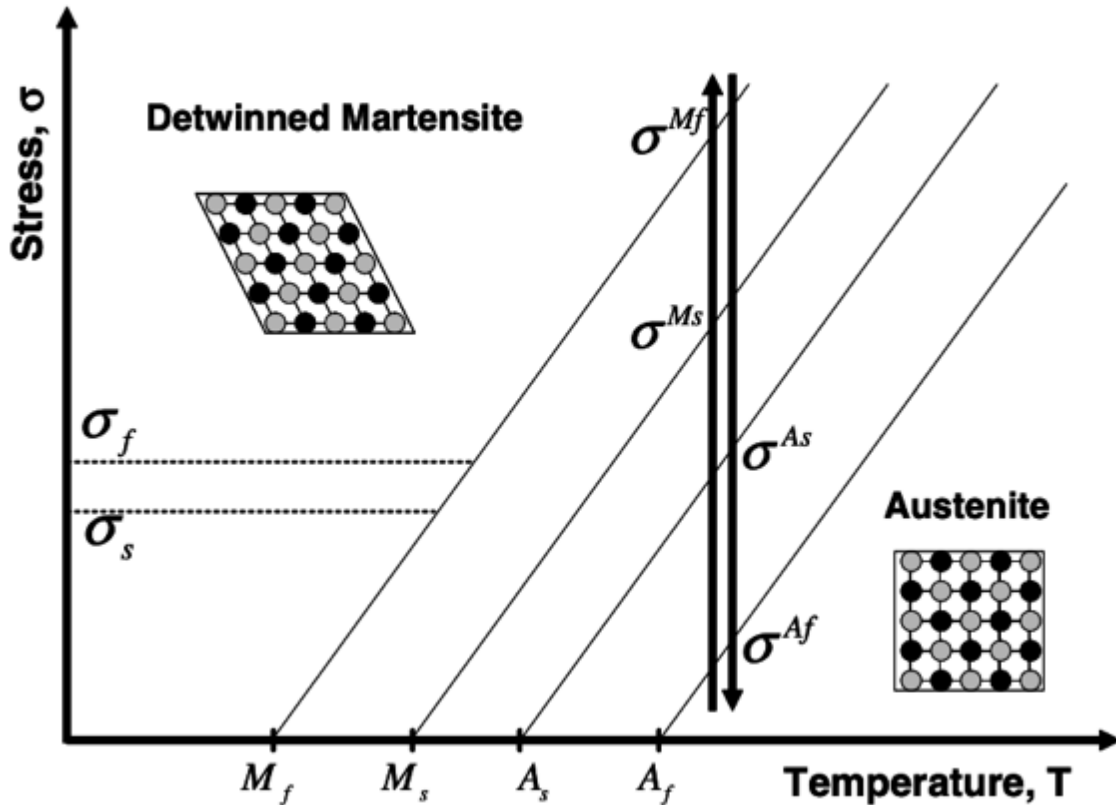


Figure 2.7 – Superelasticity effect transformation path [7]

A superelastic NiTi alloy has the capability to recover large strains from 6 % to 8 % [22], [21], which is much greater than other metallic alloys. Through research, it has been established that the superelasticity effect improves the mechanical properties, such as strength and hardness [9], [23]–[26]; in addition, it also has excellent biocompatibility [27]. Despite this, the stress-induced superelasticity effect has not been fully exploited in wear-resistant applications due to the difficulty of machining and forming bulk NiTi components.

Machining bulk NiTi results in high work hardening and stress-induced phase transformation within the material [28], [29]. Consequently, the superelasticity of NiTi causes machining and forming processes to be more complex and difficult compared to other alloys. Traditional machining (i.e. drilling, milling) of bulk NiTi results in unacceptable surface finishes and higher surface roughness. When employing traditional machining methods, it will increase both the fabrication time and the wear rate of the

tools used, which results in an increase in the overall production cost. Alternatively, the fabrication of NiTi products can be done through non-traditional machining methods [28]; such as water-jet and laser cutting, which are costly. The challenges of machining and forming NiTi restricts the applicability in industries. Therefore, there is a need for an alternative fabrication method to limit the amount of machining needed to form a product.

## **2.2 Production of NiTi**

There have been several studies that attempt to form the NiTi phase through metallic diffusion of elemental Ni and Ti through various fabrication methods. Most research studies employ Ni-Ti diffusion couples, powder metallurgy, and vacuum deposition processes to achieve the NiTi phases.

### ***2.2.1 Ni-Ti Diffusion Couples***

The sequence and growth of Ni and Ti intermetallic phases in diffusion couples have been studied in the literature [30]–[36]. Garay *et al.* [35] annealed elemental Ni and Ti foils at 650°C for 8 hours with a current density of 1527A cm<sup>-2</sup> and formed the Ni<sub>3</sub>Ti, NiTi, and NiTi<sub>2</sub> equilibrium phases as seen in Figure 2.8. The current density was applied to act as a catalyst for faster diffusion between the Ni and Ti elements.

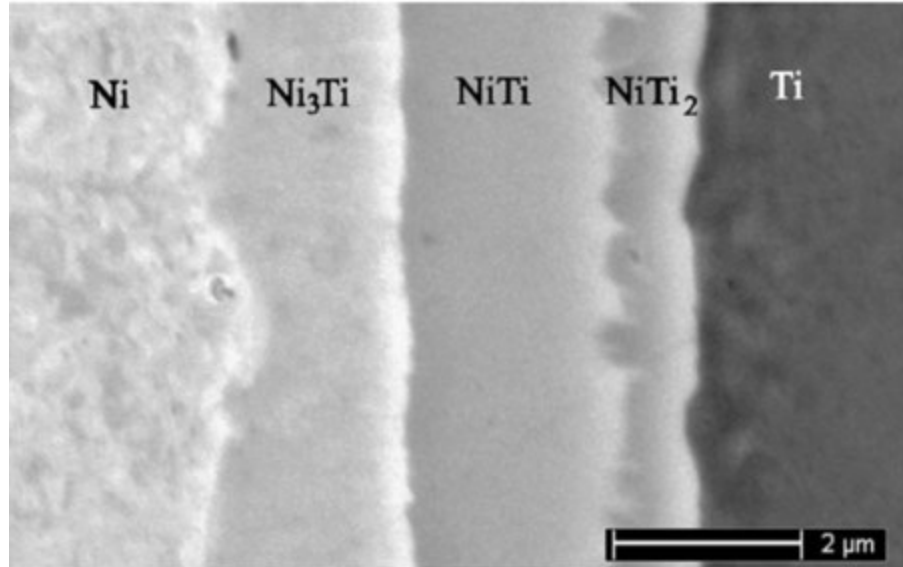


*Figure 2.8 – Back-scattered electron micrograph of products layers of sample reacted at 650°C for 8 hours with a current density of 1527 A cm<sup>-2</sup> [35]*

Hu *et al.* [30] also employed solid state diffusion of elemental Ni and Ti foils to prepare an intermetallic NiTi alloy. They found that the intermetallic NiTi compounds, namely, NiTi<sub>2</sub>, NiTi, and Ni<sub>3</sub>Ti were formed at the Ni-Ti interface at 650°C. The SEM micrographs of Ni-Ti interface under different temperatures are shown in Figure 2.9 [30].

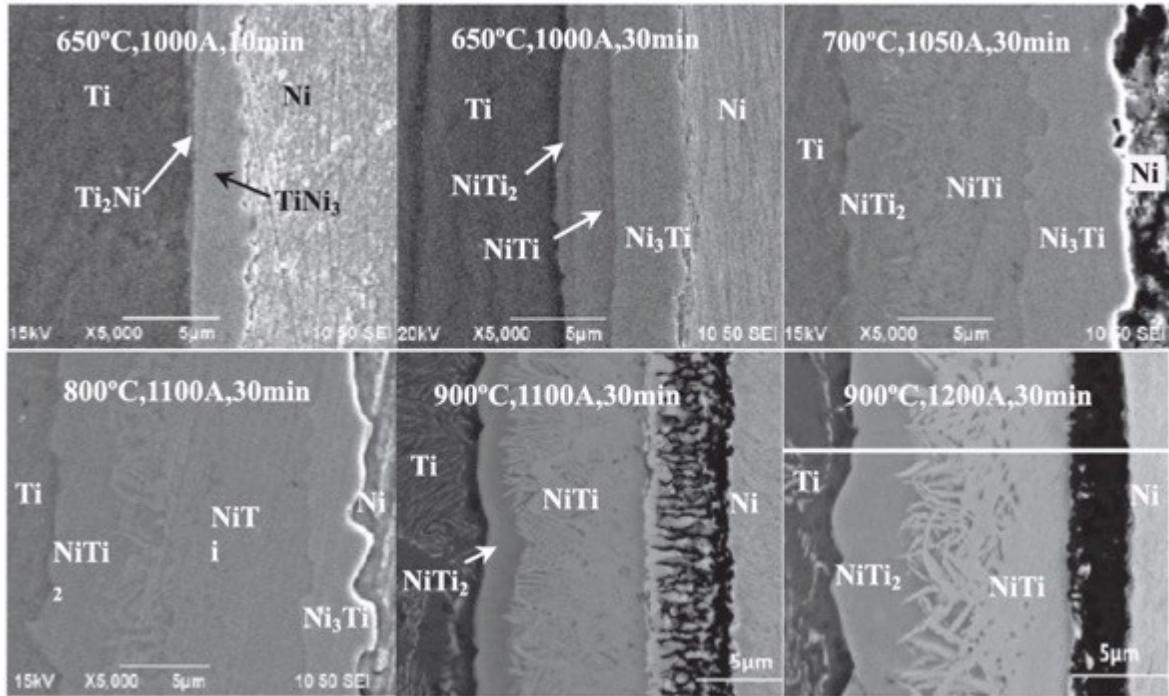


**Figure 2.9 – SEM micrographs of Ni-Ti interface under different temperatures [30]**

The study performed by Hu *et al.* [30] proposed that the precipitation of intermetallic phases occurred according to the following equations:



Indicating that the formation of NiTi is a result of the diffusion between NiTi<sub>2</sub> and Ni<sub>3</sub>Ti intermetallic phases and the Ni<sub>3</sub>Ti and Ti phases. It was also suggested that the intermetallic phases grow parabolically with respect to time, however, with prolonged diffusion NiTi is preferentially formed [30].

### **2.2.2 NiTi Powder Metallurgy**

The fabrication of NiTi has been attempted through the pressing and sintering of elemental Ni and Ti powders [37]–[39]. Mohd *et al.* [38], employed powder metallurgy

technology to prepare the NiTi alloy. They first mixed Ni and TiH<sub>2</sub> powders, then sintered at 800°C for 3 hours. They confirmed that the intermetallic NiTi alloy had formed, which can be seen in the SEM micrograph of the specimen sintered at 800°C for 3 hours is shown in Figure 2.10 [38].

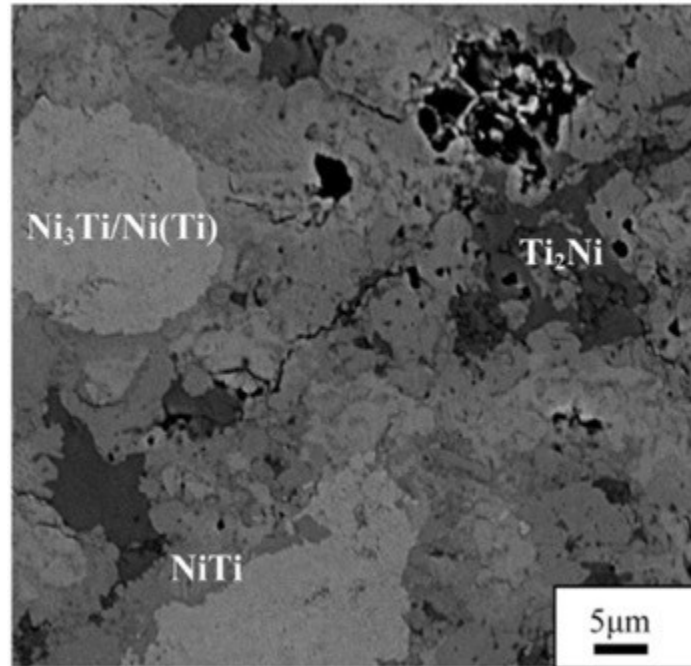


*Figure 2.10 – SEM micrograph of the specimen sintered at 800°C for 3 hours [38]*

Chen *et al.* [39] also prepared the intermetallic NiTi alloy using powder metallurgy technology. In their study, Ni (16.4μm) and Ti (32.2μm) compact was sintered at 900°C for 2 hours. The SEM micrographs of the sintered specimen containing NiTi, Ni<sub>3</sub>Ti, and NiTi<sub>2</sub> phases are shown in Figure 2.11 [39].

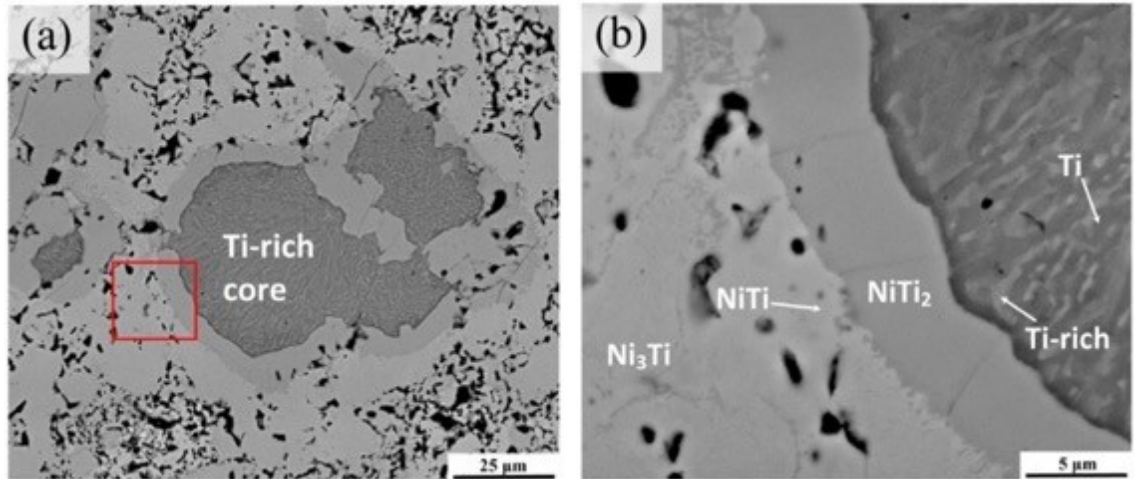


**Figure 2.11 – SEM images of the specimen sintered from the Ni-Ti compact at (a) 900°C, (b) enlarged square area in (a) [39]**

Recently, Laeng *et al.* [40] sintered 70μm Ni and Ti elemental powders at 750°C for 6 hours in a vacuum furnace. Through SEM and EDS analysis it was shown that this produced the NiTi and NiTi<sub>2</sub> intermetallic phases. Backscattered SEM images of the alloy can be seen in Figure 2.12 [40].

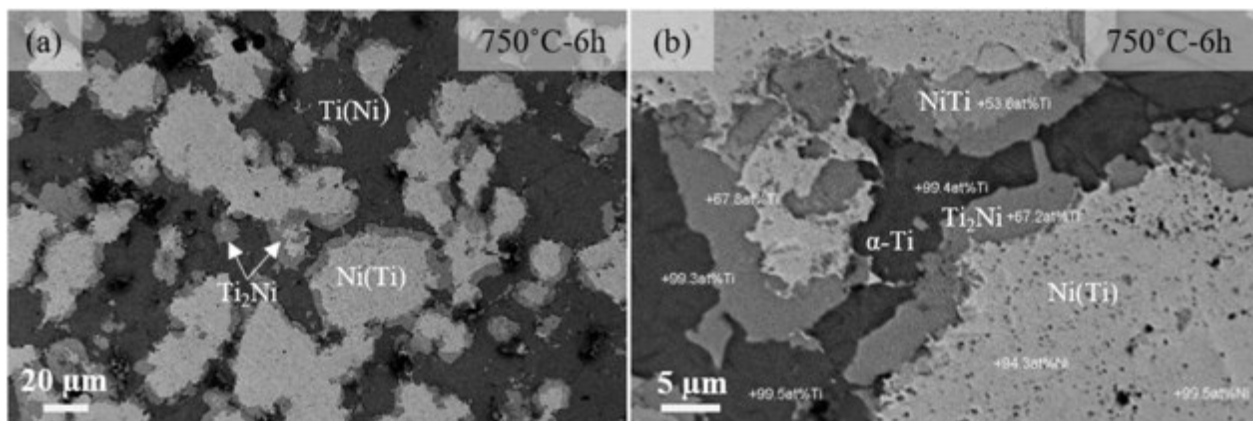
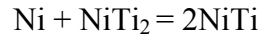


**Figure 2.12 – Backscattered SEM micrographs and EDS analysis of the phases of specimens sintered at different temperatures: a and b 750 C for 6 hours [40]**

Laeng *et al.* [40], proposed the sequence and formation of NiTi through the following equations:



According to these equations NiTi is formed through the reactions of Ti and Ni<sub>3</sub>Ti. However, Hu *et al.* [30] proposed that NiTi is also formed between NiTi<sub>2</sub> and Ni<sub>3</sub>Ti interfaces, whereas, Laeng *et al.* [40] predicted the reaction between Ni and NiTi<sub>2</sub>. Indicating that the formation of Ni and Ti intermetallic phases through solid-state diffusion is not fully understood. Despite this, it is proven that NiTi can be fabricated through annealing processes between elemental Ni and Ti.

### 2.2.3 NiTi Surface Coatings

A study performed by Zamponi *et al.* [19] states that the most prominent technique for applying monolithic superelastic NiTi as a coating is through sputtering vacuum deposition processes. Consequently, studies performed by Rumpf *et al.* [41] and Zamponi *et al.* [19] observed that magnetron sputtering a NiTi alloy directly results in a characteristic loss of Ti in the composition in the deposited coating. Composition control is vital because a slight change in the composition could result in the lack of the superelasticity effect; if the nickel content exceeds 54wt.%, then the superelastic property ceases to exist [42]. The sputtering deposition process of superelastic NiTi from a bulk NiTi target is extremely sensitive to multiple factors as outlined in literature [10], [43], [44], such as:

- Metallurgical factors – alloy composition, annealing temperature, ageing temperature, ageing time, and impurities;
- Sputtering conditions – target power, gas pressure, working distance between target and substrate, deposition temperature, and substrate temperature.

Despite this, several systematic studies were performed [37], [45], [46]. Behera *et al.* [46] sputtered a bilayer of Ni and Ti on a Si substrate, which was annealed at 500°C and 600°C for 1 hour, to successfully create the NiTi, Ni<sub>3</sub>Ti, and NiTi phases. Furthermore,

Miyazaki *et al.* [37], [45] also confirms the NiTi can be achieved in thin films by annealing sputtered Ni and Ti multilayers at 750K. It is found that the superelastic NiTi phase (B2) was formed after annealing. The TEM images and diffraction patterns of the thin films before and after annealing are shown in Figure 2.13 and Figure 2.14 [37]. Noting that the diffraction patterns confirm the presence of NiTi and neither residual Ni nor Ti were observed to be present in the final composition [45].

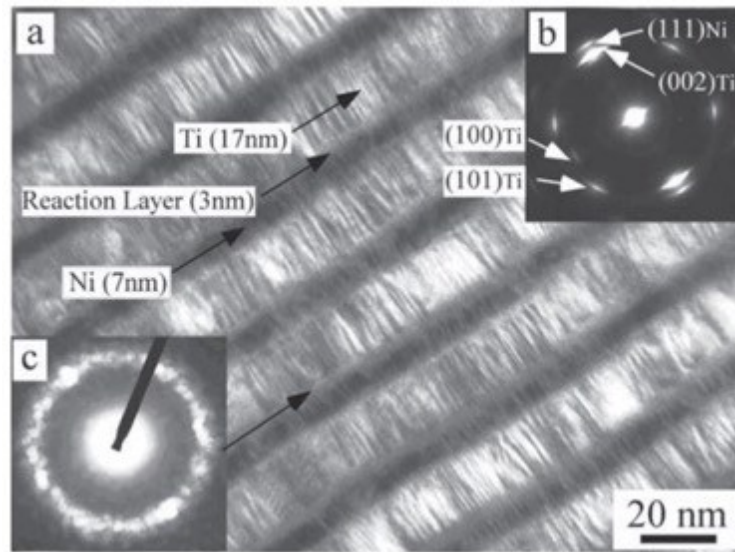


**Figure 2.13 – TEM image and diffraction patterns of as-sputtered Ni and Ti multilayers thin films (1). (a) bright field TEM image, (b) the corresponding selected area diffraction pattern, and (c) NBD pattern of the cross-section including the Ti and Ni layers [37]**

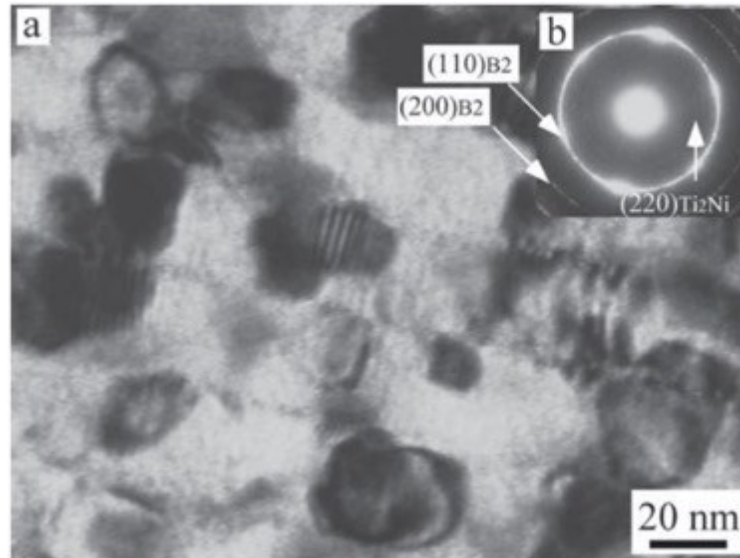


**Figure 2.14 – TEM image and diffraction patterns of Ni and Ti multilayers thin films annealed at 750K (1); (a) bright field TEM image, (b) the corresponding selected area diffraction pattern [37]**

#### **2.2.4 Factors Influencing NiTi Formation**

The production of the intermetallic NiTi phase is possible through solid-state diffusion of elemental Ni and Ti, however, there is limited information on the factors that can affect the formation and development of the NiTi intermetallic precipitate. Some effects include the Kirkendall effect and the residual stresses.

##### **2.2.4.1 Kirkendall Effect**

Bastin *et al.* [36] gained significant insight into the semi-infinite linear diffusion process in a Ni-Ti diffusion couple. This study suggested that NiTi<sub>2</sub> growth rate was lower compared to the growth rate of the NiTi phase, however, both phases are diffusion controlled. It was also found the Ni<sub>3</sub>Ti phase initially grew rapidly then stabilized at a thickness of 20μm [36]. This study was able to compare the Ni and Ti intrinsic diffusion coefficients, which found that Ni diffuses more rapidly compared to the Ti within the system. This finding is important because it signifies that there is an imbalance in diffusivities, which prompts the Kirkendall effect.

The Kirkendall effect was discovered when annealing between brass and copper, with molybdenum (Mo), wires placed at the interfaces [47], seen in Figure 2.15. It was observed after diffusion, that the distance between the inert molybdenum wires gradually decreased. Concluding that the zinc in the brass alloy diffused more rapidly out than the copper species diffused inwards. This imbalance of fluxes between the copper and zinc resulted in the discovery of a phenomenon termed the Kirkendall Effect.

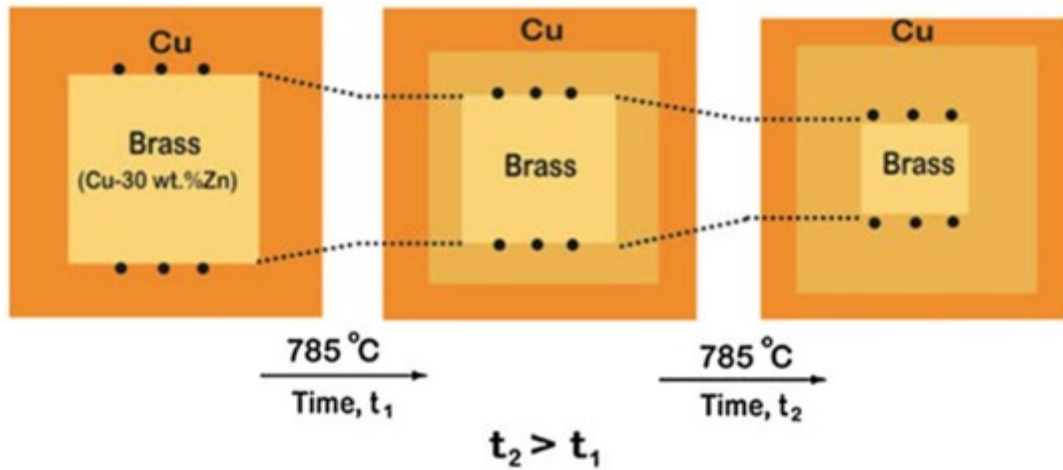


*Figure 2.15 – Schematic illustration of the Kirkendall's experiment [47]*

The Kirkendall effect in a binary alloy can be seen in Figure 2.16. The Kirkendall plane ( $X_k$ ) begins at the interface between the two species. Annealing at elevated temperature results in the shift of the  $X_k$  interface, this is a consequence of species  $NB^-$  having a more rapid diffusion rate than the  $NB^+$  species. The  $X_k$  interface continues to shift due to the inequality of diffusivities of the two elements.

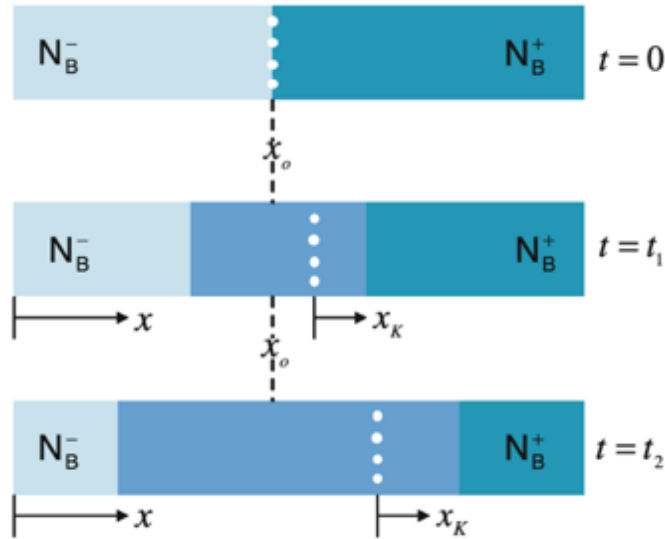


**Figure 2.16 – Movement of the inert markers with the increase in annealing time, where  $t_2 > t_1 > t = 0$  [47]**

The Kirkendall effect can also lead to porosity in binary systems. The element with the higher diffusivity will diffuse out of the material more rapidly, which may cause an influx of vacancies that coagulate to form a void [48]. The presence of voids, even at low fractions, dramatically reduces overall properties of the material; specifically, shear strength [49]. If many voids are present it can weaken the material.

#### 2.2.4.2 Residual Stresses

It has been proved that the distributions of residual stress significantly impacts the adhesion and the fracture toughness of thin films [50]. According to the study performed by Fu *et al.* [51], the deposition of a thin film monolayer of NiTi results in high residual stresses. Residual stresses are a combination of both thermal stresses and intrinsic stresses that form during fabrication and heat treatment processes.

Thermal stresses arise as a result of the coefficient of thermal expansions (CTE) of the materials. In multilayer structures, due to the non-homogeneous material properties, large tensile stresses may arise due to the non-linear thermal gradient when heating and cooling [52]. The material with a higher coefficient will experience tensile stress and as a result,

it will generate compressive stresses in the other material. If the CTE values of the materials greatly differ, it will induce large tensile stresses. The thermal stresses in materials arise from the fabrication process and the cooling rates associated with the heat treatment processes.

On the other hand, intrinsic stresses occur due to the stresses that are generated during the deposition process. In multilayered structures, intrinsic stress occurs in thin films due to the difference in lattice spacing between the layers [53]. If the stresses surpass the overall yield strength of the coating, fracture or plastic deformation may occur [52], [54]. Intrinsic stresses also occur depending on the coherency state of the precipitates as they form and grow when subjected to a heat treatment process.

#### 2.2.4.3 Coherency State of Precipitates

The precipitation of a phase may increase the residual stresses in a material, due to the ‘mismatch’ in atomic spacing between the precipitate and the matrix. According to studies done by Bernard *et al.* [55] on LiH alloys, and Sijacki-Zeravcic *et al.* [56] on Al-Cu alloys, precipitates are likely to be coherent with the matrix if the atomic lattice parameters are similar. There are three states that the precipitate can be: coherent, semi-coherent or incoherent shown in Figure 2.17(a), (b), and (c), respectively, which are described below.

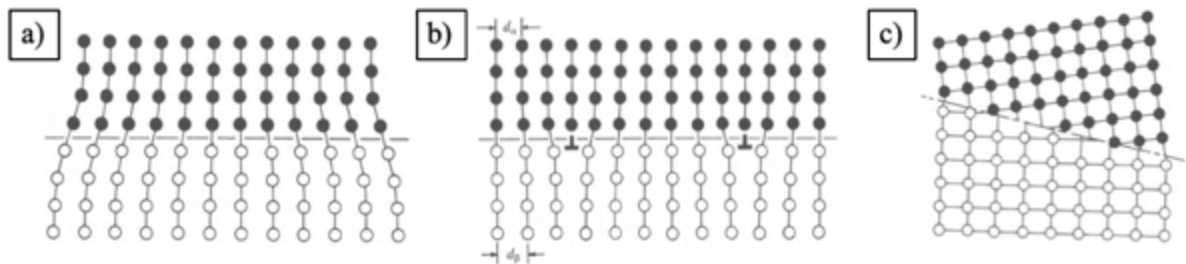


**Figure 2.17 – Illustration of a) coherent b) semi-coherent and c) incoherent interfaces [57]**

A coherent interface indicates that the precipitate is perfectly bonded to the matrix, as seen in Figure 2.17(a). At the interface, there is usually an increase in interfacial energy

due to the different spacings between the atoms [57], generating stress fields around the precipitate to accommodate the “mismatch”. As the precipitate increases in size, the interfacial energy will also increase.

The total energy will reach a point where it will be energetically favorable to change the coherent interface to a semi-coherent interface (Figure 2.17(b)). To reduce the interfacial energy, edge dislocations are generated, these are called misfit dislocations [57]. The misfit between lattices,  $\delta$ , can be calculated through Equation (1). Where  $d$  is the unstresses interplanar spacing of the respective materials.

$$\delta = \frac{d_{\beta} - d_{\alpha}}{d_{\alpha}} \quad (1)$$

As the precipitate continues to grow, more edge dislocations are needed to relieve the interfacial stresses. Finally, the stresses exceed the strength of the matrix it will break the bonds to the surrounding atoms [57], as seen in Figure 2.17(c). This is an incoherent interface where there are no interfacial energies or stress fields around the precipitate.

## **2.3 Contact and Fracture Mechanics**

When assessing the wear behavior of materials, it is necessary to understand contact and fracture mechanics that occur under wear conditions. This is practical in certain applications such as hardness, wear, and impact testing [58]. The cracks that occur during wear testing can change depending on the indenter and the nature of the material, which is further explained in this section.

### **2.3.1 Hertzian Contact**

Elastic contact was studied by Hertz, who examined the localized deformation and pressure distribution between two elastic bodies coming into contact [59]; this is termed Hertzian contact. Hertzian contact occurs upon the indentation of a rigid sphere, a region of compressive stress forms under the indenter and a region of tensile stress is generated at the edge of the contact area. Hertzian contact is typically used to determine the properties of brittle materials and ceramics. Two modes of failure can occur in Hertzian contact, these modes are Hertzian cracks and a network of micro-cracks in the quasi-plastic zone. Hertzian (or cone) cracks are generated if the load,  $P$ , is applied and exceeds the critical load. The ring cracks appear on the surface and extend downwards in a cone-like shape [58]–[60], as seen in Figure 2.18.

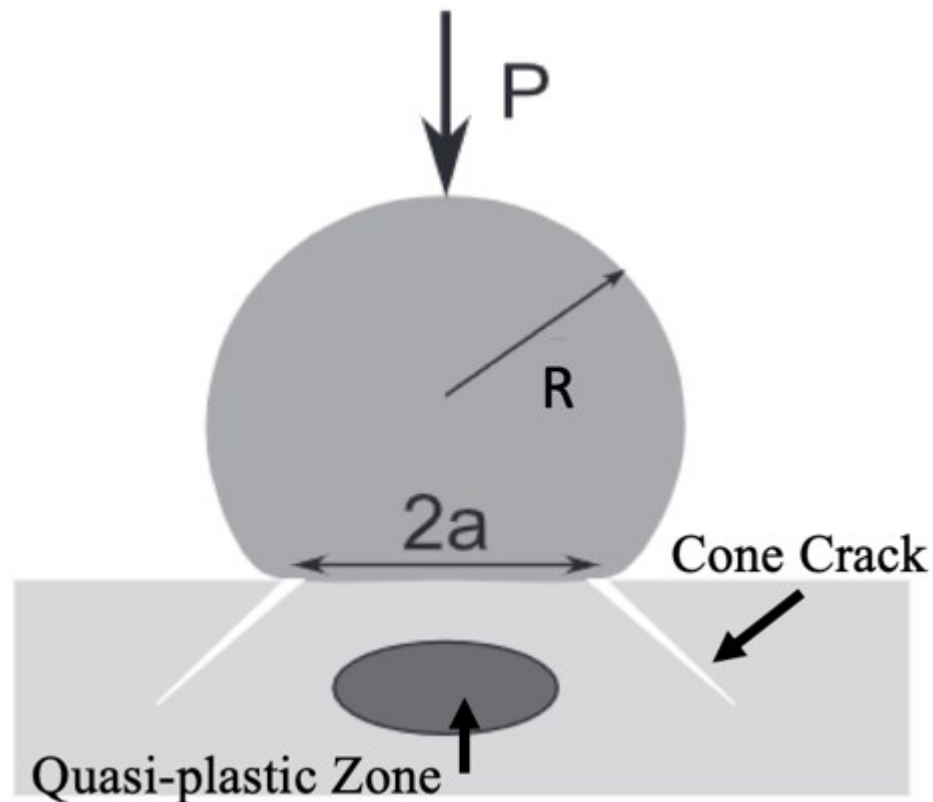


*Figure 2.18 – Hertzian cone model [60]*

Following this development, Hertz established equations that study the relationship where the radius of contact radius ( $a$ ) is related to the indenter load ( $P$ ), the indenter

radius  $R$ , and maximum tensile stress ( $\sigma_{\max}$ ). The contact radius can be described in Equation (2).

$$a^3 = \frac{3PR}{4E^*} \quad (2)$$

Where the reduced modulus,  $E^*$ , can be calculated using Equation (3), where  $E$  and  $\nu$  are the elastic modulus and Poisson's ratio for the coating, respectively. Likewise,  $E_i$  and  $\nu_i$  are the elastic modulus and Poisson's ratio for the indenter.

$$\frac{1}{E^*} = \frac{(1 - \nu^2)}{E} + \frac{(1 - \nu_i^2)}{E_i} \quad (3)$$

Mean contact pressure ( $p_m$ ) is the pressure induced by the indenter divided by the contact area, described in Equation (4). Noting that the equation is only valid when assuming that the two bodies will behave elastically.

$$p_m = \frac{P}{\pi a^2} \quad (4)$$

Hertzian ring cracks initiate if the maximum tensile stress,  $\sigma_{\max}$ , exceeds the strength of the material being indented. The maximum tensile stress can be found in Equation (5).

$$\sigma_{\max} = \frac{1}{2} (1 - 2\nu)p_m \quad (5)$$

The second failure mode is the quasi-plastic zone occurring subspace below the indenter and has the appearance of plastic deformation, however, it is a network of microcracks

that are shear driven [61]. The maximum shear stress,  $\tau_{max}$ , is located within the quasi-plastic zone and be calculated through Equation (6).

$$\tau_{max} = 0.47 p_m \quad (6)$$

The maximum shear stress is located at a depth,  $x$ , that can be calculated through Equation (7).

$$x = 0.49 a \quad (7)$$

### *2.3.1.1 Cracking Modes*

There are a variety of cracks that may form upon contact with brittle materials. The five main types of cracks are radial, lateral, median and half-penny, which are depicted in Figure 2.19(a), (b), (c), and (d), respectively. These cracks form under elastic-plastic contact, which leaves a plastic impression on the surface. Both the lateral and radial cracks appear close to the surface and can influence the fracture toughness of the material [58]. The different cracks are further defined below.

- Radial cracks are generated when a sharp indenter or high loading of a blunt indenter is applied. They are initiated at the edges of the indent and extend parallel to the loading axis;
- Lateral cracks are formed beneath the plastic deformation zone, parallel to the surface;
- Median cracks are formed subsurface in the quasi-plastic zone and propagate parallel to the loading axis;
- Half-penny cracks are a combination of both median and radial cracks that develop during unloading of an applied load.

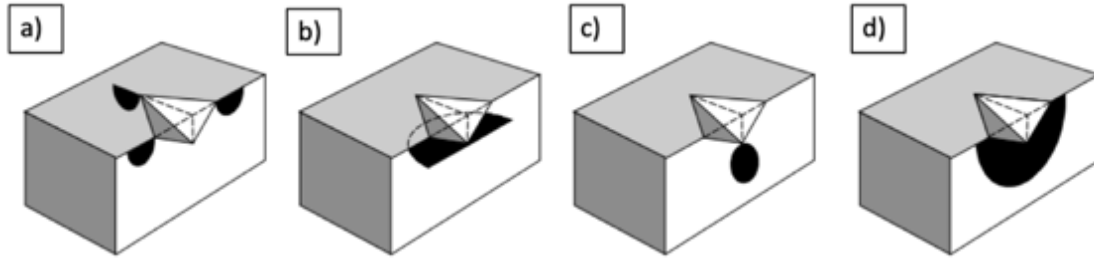


*Figure 2.19 – Morphology of a) radial b) lateral c) median and d) half-penny cracks [58]*

### **2.3.2 Multilayered Structures**

The fracture response of a multilayered structure is influenced by the material property gradient and layer thickness within the multilayered material. Indentation testing can be used as a method to identify weaknesses in multilayered materials [61], [62]. In multilayered materials, failure modes are influenced by a multitude of factors, such as mechanical properties of the testing materials, indenter geometry, and loading conditions [63]. The response to indentation of the multilayered material depends on the bonding between the interfaces and mechanical properties of the layers [64].

Indentation testing on multilayered structures can generate micro-cracks in the quasi-plastic region. It is difficult to detect these pre-existing cracks during an inspection, as the cracks exist subsurface. These pre-existing cracks will propagate and converge resulting in material removal, generally within a coating that has a moderate thickness [65]–[67]. However, in thin and thick coatings Hertzian cracks are the predominant failure mode [68]. Weak interlayers in multilayered structures will promote cracking in the coatings and cause delamination [69].

#### *2.3.2.1 Delamination*

Delamination of the multilayered coating may occur when the coating exhibits weak bonding at the interfaces [63], [68]. The stress field generated by a growing crack tip, if adequate, can lead to the delamination or fracture as it encounters a second-phase, significantly decreasing the load-carrying capacity [70], [71]. Thus, decreasing the

overall strength and toughness of the coating. The theory of delamination wear is described by Suh *et al.* [72], as illustrated in Figure 2.20.

- The sliding indenter causes plastic deformation, which generates dislocations;
- The dislocations will begin to gather and create voids in the material;
- These voids will coalesce due to the growth and shearing of the material, which results in the initiation of cracks that will grow parallel to the surface;
- These cracks then propagate and intersect, at which the surface will shear, resulting in the delamination of the material.

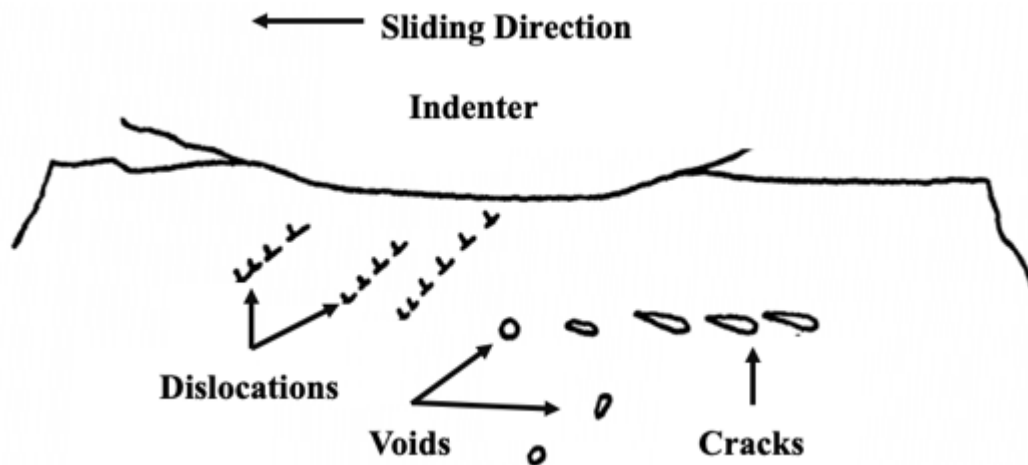


*Figure 2.20 – Theory of delamination wear [72]*

## 2.4 Wear Behavior

Wear is defined as the damage done onto the surface of a material by a sliding, rolling, or impacting motion that results in material removal or displacement [73]–[76]. A method to suppress these damages is to apply a wear-resistant coating that will provide protection to working components such as steels. The main types of wear include adhesion, abrasion, impact, and erosion. The wear behavior in monolithic materials has been studied, however, in multilayered materials, it becomes more difficult to analyze.

## 2.4.1 Monolithic Materials

### 2.4.1.1 Adhesive Wear

Adhesive wear is defined by Budinski as the “... loss of material from or damage to a solid surface in rubbing contact caused by solid-state bonding [adhesion] between the rubbing surfaces.” [74]. Several factors influence adhesion wear; this includes size and distribution of the contact area, the duration of the contact, and the shape of the asperities [77]. Figure 2.21 shows that as the two materials come into contact, the softer material adheres to the harder material, thus, resulting in material transfer.

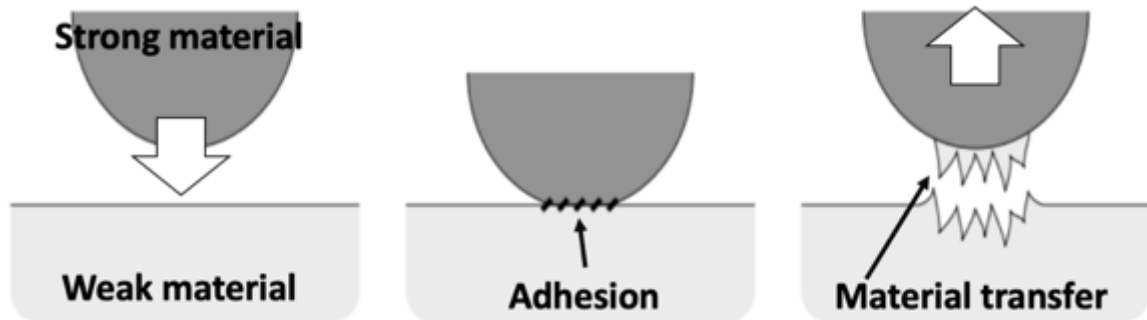


*Figure 2.21 – Adhesive wear [75]*

Consequences of adhesive wear results in mechanisms such as seizure and galling. Galling is the microscopic adhesion that occurs under transverse sliding conditions [74]. Seizure occurs when the friction force needed to shear the weaker material is not sufficient, resulting in the two bodies adhering, prohibiting them from moving [74].

Adhesive wear can be described through Archard’s law in Equation (8) [75]. Assuming that the depth of removal remains constant and proportional to the radius of the asperities and the two asperities are of the same size.

$$W = \frac{KP}{H} \quad (8)$$

Where  $W$  is the wear rate,  $K$  is a wear coefficient,  $P$  is the applied load, and  $H$  is the hardness of the softer material. According to Archard's law, as the applied load increases so does the adhesion wear rate.

#### 2.4.1.2 Abrasive Wear

Abrasive wear occurs when a softer materials interface is plastically deformed by asperities or particles of a harder material [73]. Although similar to adhesion wear, it does not include a material transfer. There are four basic forms in which abrasive wear can occur: cutting, fracture, fatigue by repeated ploughing, and grain pull-out.

The most severe form of wear for ductile materials is cutting [76]. Cutting, illustrated in Figure 2.22(a), is the removal of a weaker material by a shearing force exerted by a stronger material. If the material is not removed or sheared but is displaced around the contact area, ploughing occurs. Ploughing is a less efficient material removal method compared to cutting [75].

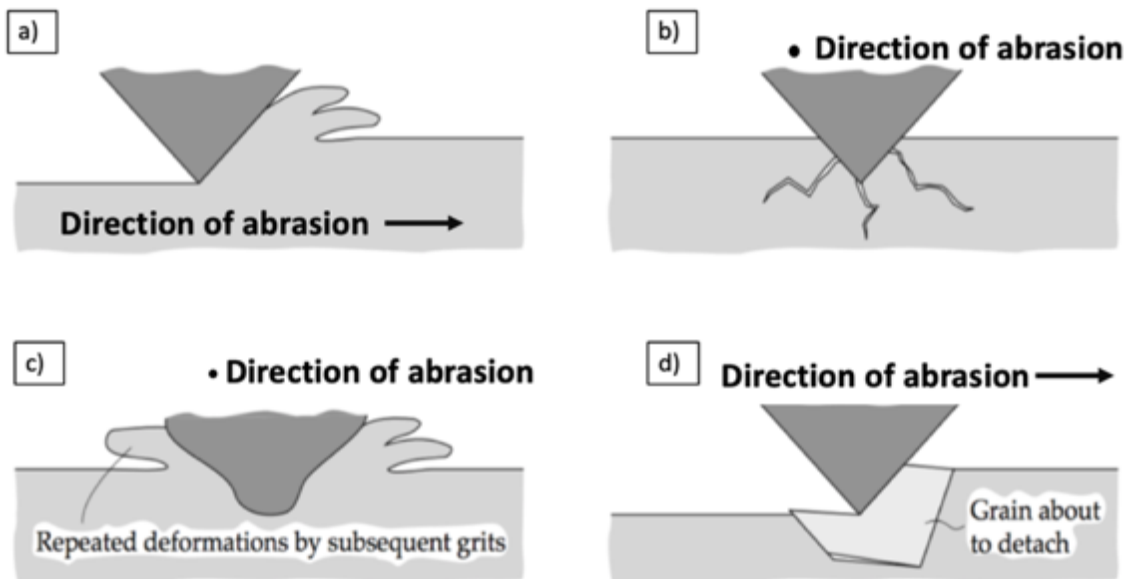


***Figure 2.22 – Abrasion wear a) cutting b) fracture c) fatigue d) grain pull-out [78]***

Fracture occurs in the case of contact with brittle materials, as illustrated in Figure 2.22(b). As the sharp indenter slides over the material, pre-existing lateral cracks propagate upwards towards the free surface. As a result, the cracks can intersect and converge causing the material to be removed [78].

Fatigue by repeated ploughing occurs when a ductile material undergoes repeated strains (i.e. loading and unloading cycles) that may induce subsurface or surface cracks resulting in plastic deformation [78], which is depicted in Figure 2.22(c). The material displacement around the body is subjected to repeated strains, as the indenter slides back and forth.

Grain pull-out mainly occurs in ceramics, shown in Figure 2.22(d), the sliding indenter will detach a grain from the matrix. Ideal conditions for this type of wear to occur is weak bonding between large grains [78], however, this mechanism is rarely seen.

#### *2.4.1.3 Erosion and Impact Wear*

There is a significant interest in using impact testing for studying erosion. Erosion encompasses a combination of many mechanical wear mechanisms. Initially, a particle impacts a solid surface and the kinetic energy from the particle is transferred into the material resulting in internal stresses [73], [79]. The kinetic energy can be totally or partially dissipated through ductility, phase transformations, and heat [79]. All of which depend on operational properties and the impacting particle, such as particle speed, velocity, hardness, size, and shape. The most common modes of erosion can be seen in Figure 2.23, which can occur upon impingement under different conditions. These modes are abrasion, fatigue, and plastic deformation.

Impacting particles could cause cutting (abrasion), Figure 2.23(a). Cutting is common in ductile materials and occurs at low impact angles over a range of different velocities and it includes material displacement of the surface or material removal.

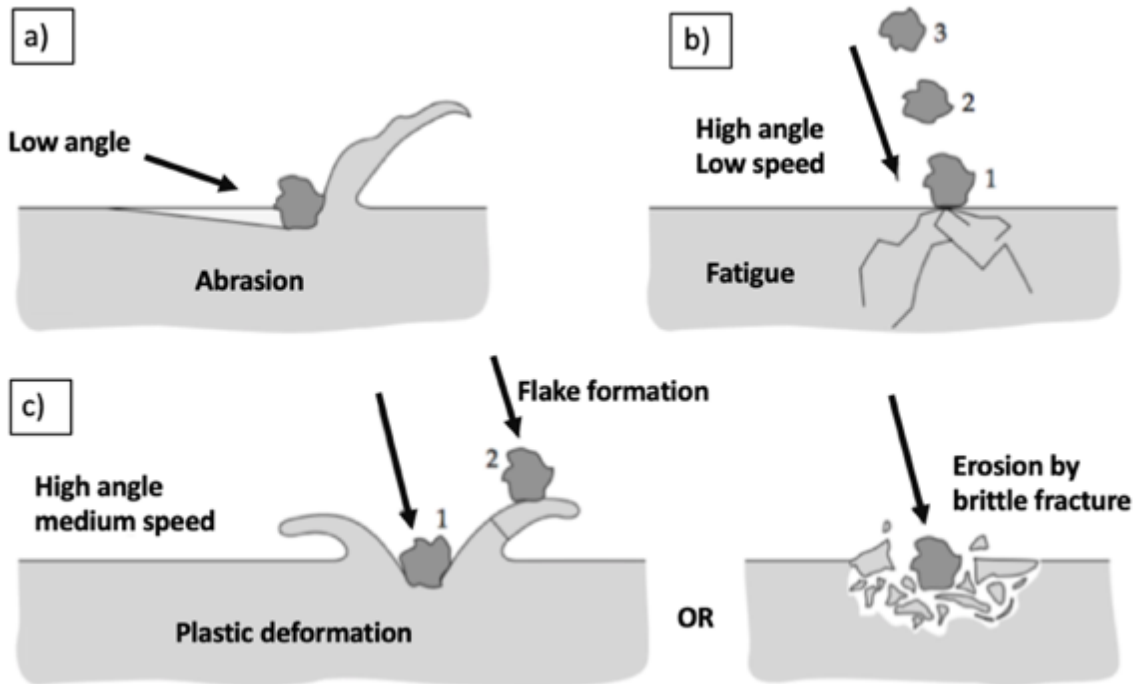


*Figure 2.23 – Erosion mechanisms by a) abrasion b) fatigue and c) plastic deformation [78]*

Fatigue erosion, Figure 2.23(b), occurs when the same location is impacted multiple times at low speeds and high angles. The repeated strain (i.e. loading and unloading cycles) may induce subsurface or surface cracks, which eventually will result in the formation of wear debris [73]. Each time the solid surface is impacted it results in internal cracks, and further impaction leads to the propagation of these cracks.

The materials response to impact or erosion testing can be classified as either ductile or brittle, as seen in Figure 2.23(c). Ductile materials will undergo material displacement, the material that is displaced will be work-hardened. On the other hand, brittle materials will result in the intersection of cracks, which will result in wear particles.

Both the impacting angle and speed play a major role in determining the wear rate of both ductile and brittle materials. Ductile materials will plastically deform until the material is removed by abrasive wear, whereas, brittle materials will have internal cracks that will propagate and intersect [73]. Figure 2.24 shows a relation between both brittle and ductile wear behavior. Ductile materials will increasingly erode until the maximum angle of approximately  $30^\circ$ , then the wear rate decreases. However, in brittle materials the wear rate increases as the impingement angle increases.

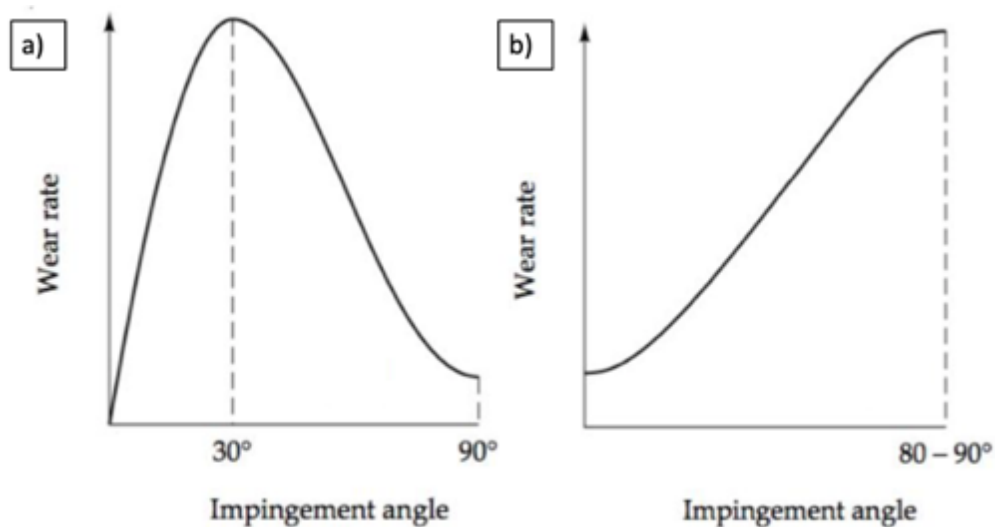


*Figure 2.24 – Wear rates behavior for a) ductile and b) brittle materials [78]*

#### **2.4.2 Multilayered Materials**

Multilayered materials are proven to have increased mechanical properties compared to monolithic materials [80], [81], which makes them advantageous for wear-resistant applications. The improved wear resistance is attributed to the interfaces of the layered structure that decelerate the propagation of cracks [82]. In multilayered materials, the more ductile layers have the capability to absorb excessive plastic deformation and harder layers provide the resistance to wear [83]. A study performed by Skordaris *et al.* [82] suggested that a TiAlN multilayered coating can more effectively withstand loads due to the property gradient of the layers compared to monolithic materials.

Although the wear mechanisms of multilayered coatings have not been explicitly studied, most literature on multilayered structures are based on the expansion of the findings from second-phase and fiber or particle reinforced metal matrix composites [83]–[85]. Multilayered materials can provide toughness through different mechanisms, such as bridging, deflection, and stress-induced phase transformation as depicted in Figure 2.25.

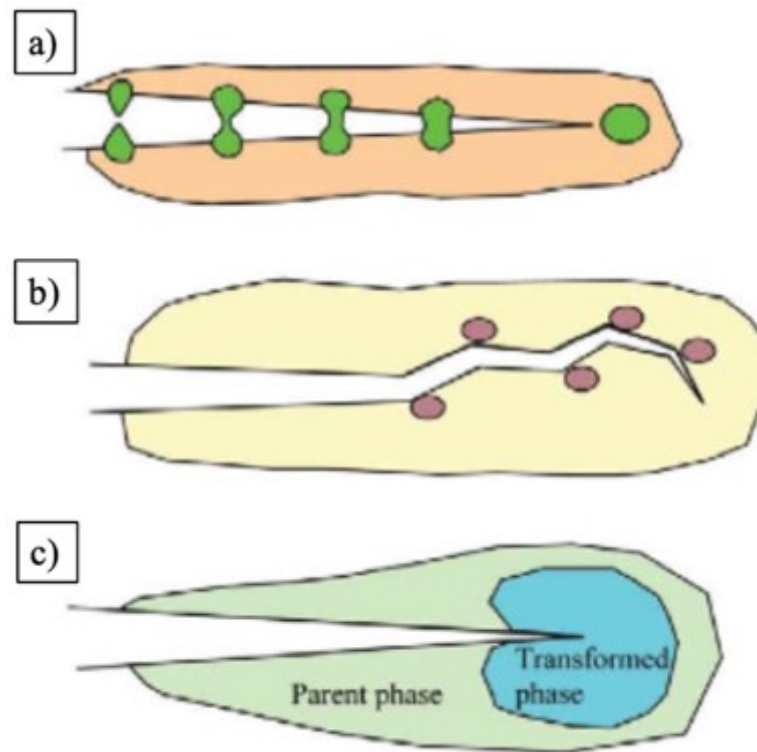


*Figure 2.25 – Composite wear behavior a) bridging, b) deflection and c) transformation toughening mechanisms [70]*

Bridging occurs when a propagating crack encounters a ductile material within the matrix, shown in Figure 2.25(a). As the crack encounters the ductile phase, the cracking energy is partially absorbed [84], [85], this impedes the cracks ability to grow as it needs more energy to pass through the other phase. Furthermore, if the cracking energy is totally consumed by the second-phase this will prohibit the crack from growing; hence another toughening mechanism termed crack arrest.

The mechanical properties of the materials influence the toughening mechanism. Crack deflection, Figure 2.25(b), is a result of a propagating crack confronting a harder material within the matrix. The interaction between the crack and the second material results in the crack path changing the direction of growth [84], [86]. Thus, the change in direction requires the cracking to dissipate more energy [87], [88].

Lastly, transformation toughening occurs when a growing crack encounters a second - phase that can undergo a stress-induced phase transformation. The stress-induced martensitic phase transformation is prompted by the stress that occurs around a crack tip [89]–[91]. The cracking energy associated with the crack is then consumed by the transformation, thus requiring a greater applied stress to allow for crack growth. The phase transformation is accompanied by a volume change [89]. When undergoing the phase transformation, a compressive or tensile strain field is generated around the phase. A compressive strain field around the transformed material can prohibit the crack from further growth.

Another toughening mechanism that should be mentioned is micro-cracking. If the cracking energy is dissipated through larger cracks, these cracks will likely be long and extend through the coating, leaving the substrate exposed, and causing severe damage to the coating. On the other hand, the same amount of cracking energy could be dissipated through a network of fine cracks or micro-cracks. Micro-cracks are generated from sites of high surface tensile stresses [92], [93], which results in cracks that are fine and shallow, minimizing the surface damage of the coating. Micro-cracking can lead to an increase in fracture toughness and a lower elastic modulus [94].

### **2.4.3 *Wear Behavior of NiTi Alloys***

NiTi alloys exhibit superior wear resistance compared to other metallic materials [95]. In metallic materials, the wear resistance depends on the mechanical properties such as hardness, toughness, strength, and ductility. However, the NiTi alloy is able to achieve

greater wear resistance due to the superelasticity effect that it possesses [2], [4], [93], [95]–[99]. Liang *et al.* [96], concluded that a superelastic NiTi alloy behaved elastically causing little material loss and it was also suggested that the wear resistance is dependent on the amount of recoverable strain within the alloy.

This agrees with the studies performed by Zhang *et al.* [2] and Farhat *et al.* [97]. Zhang *et al.* [2] observed that the superelastic NiTi alloy has an elastic recovery 5 times greater compared to Ni and 2 times greater compared to Ti, resulting in better wear resistance. Farhat *et al.* [97] observed that a superelastic NiTi alloy exhibits a large elastic recovery and a low E/H ratio which suggests excellent wear resistance. Furthermore, Neupane *et al.* [93], reported seeing micro-cracks during sliding wear of a superelastic NiTi, the micro-cracks extended perpendicular to the sliding direction, which is evidence of a toughening effect.

Recently, NiTi has been deposited as a surface coating through physical vapor deposition (PVD) processes such as sputtering. Zhang *et al.* [98] verified that a superelastic NiTi interlayer between aluminum and CrN improves wear resistance by a factor of 100 and increases the critical load required for delamination. In a similar study done by Ni *et al.* [4], found that a superelastic NiTi interlayer decreases both the COF and wear loss of a composite coating. Both studies indicate that the wear behavior of a superelastic NiTi coating is similar to that of the bulk NiTi alloy.

The wear behavior of NiTi alloys has been attributed to the superelasticity effect. During the phase transformation from austenite to detwinned martensite, the energy transferred from the external stress is stored as elastic strain. This elastic strain does not influence the wearing of the material, and upon unloading the detwinned martensite reverts back to the parent austenitic phase, recovering the elastic strain. The main factors that contribute to the excellent wear resistance are the large contact area between the applied force and the material, and limiting the crack growth [100], [101]. The superelastic NiTi alloy is able to increase the contact area between the external force and the material resulting in a larger area for the stress distribution, which minimizes the surface damage. The ability of the

superelastic NiTi effect to partially absorb and dissipate cracking energy through the stress-induced martensite phase transformation, opposed to plastic deformation or crack propagation, lessens the overall damage that would occur in other metallic materials.

## 3.0 Experimental Procedure

### 3.1 Fabrication of the Coatings

Plain carbon steel (AISI 1018) samples were ground with SiC 240, 320, 420, and 600 grit paper and were polished with 9 $\mu\text{m}$ , 3 $\mu\text{m}$ , and 1 $\mu\text{m}$  diamond paste. These samples were then coated using a DC magnetron sputtering system at the nanoFAB laboratory at the University of Alberta (Alberta, Canada). The substrate is positioned at the top of the chamber while both the Ni and Ti targets are positioned on the bottom, as seen in Figure 3.1. The air within the chamber is then completely removed to allow a pure inert gas to be passed through the chamber at a base pressure of  $1.33 \times 10^{-7}$  mbar by a cryopump. The steel substrates are secured onto a 100mm silicon wafer, the wafer is then placed on a positively charged holder.

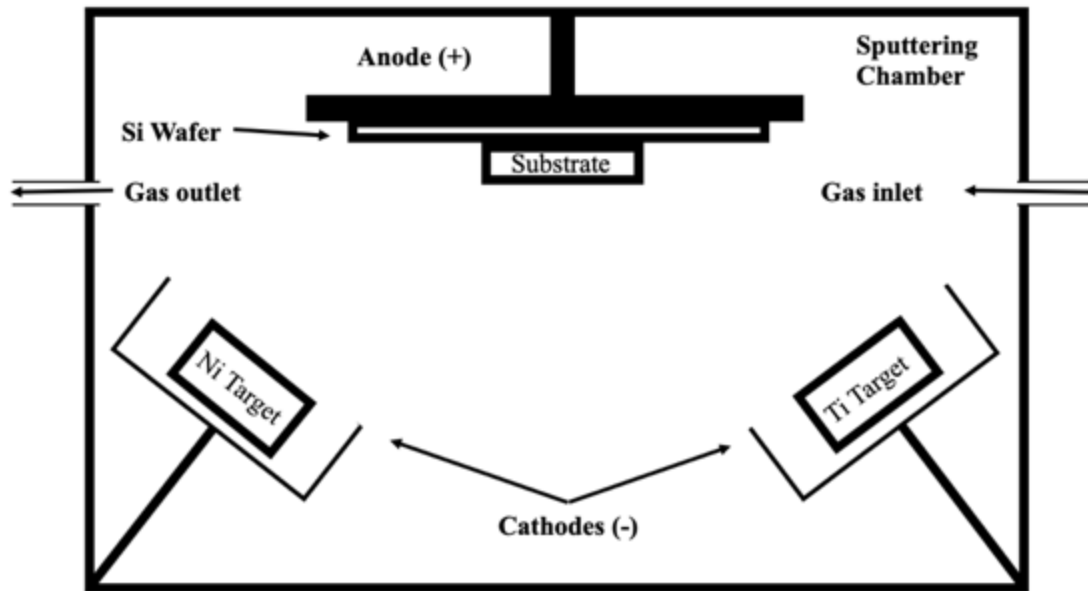


*Figure 3.1 – Schematic of the sputtering process*

Inert gas atoms then bombard the target causing the release of the ions. The target ions then travel to the anode where they are deposited onto the surface of the substrate [102]. Alternating 100nm layers of Ni or Ti is possible by placing a magnetic field around one

target at a time. The resulting laminate can be seen in Figure 3.2. Inductively Coupled Plasma Optical Emission Spectrometry (ICP-OES) was performed on the as-sputtered coating to confirm Ni and Ti were deposited in equal volumetric amounts. ICP-OES was performed using iCAP 7000 from Thermo Scientific Inc.

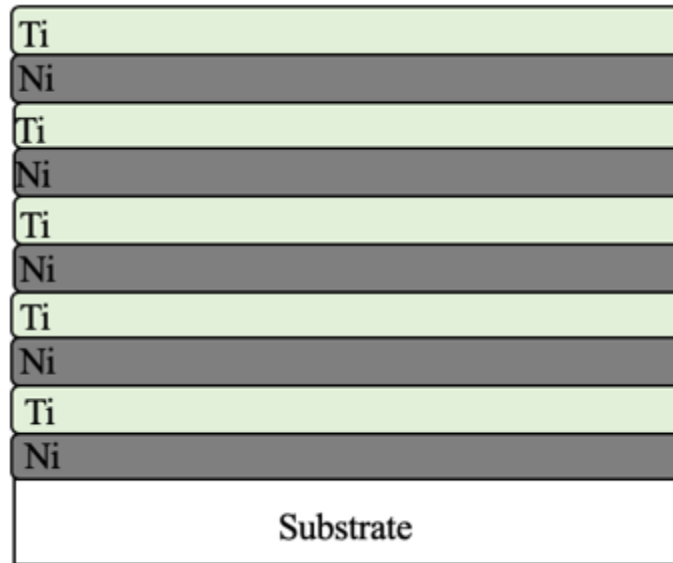


*Figure 3.2 – Schematic of Ni/Ti nanolaminate*

To form the NiTi intermetallic phase the nanolaminates were subjected to a heat treatment process. The coatings were placed in a graphite crucible, then inserted into a R.D. Webb vacuum furnace (Figure 3.3) where a vacuum of  $3 \times 10^{-5}$  mbar was established. The coatings are then heated at a rate of 20 °C per minute to 150 °C, 500 °C, 650 °C, and 800 °C where they were held for one hour. Under vacuum, the nanolaminate coatings were then moderately cooled (5 – 10 °C/min) to room temperature.

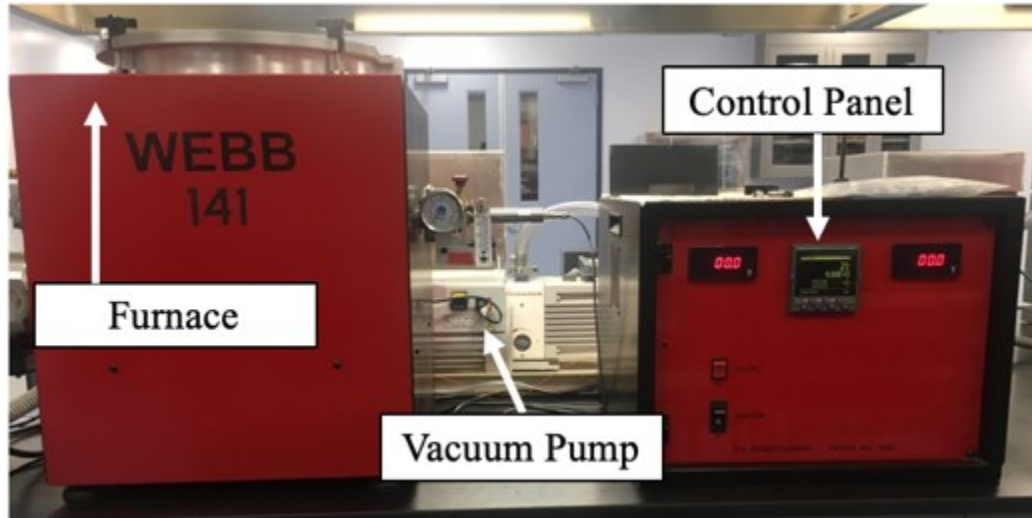


*Figure 3.3 – R.D. Webb vacuum furnace*

A DC magnetron sputtering system was also employed to produce a 50 $\mu$ m monolayer of superelastic NiTi. To ensure the coating would be superelastic at room temperature, the coating was designed for the  $A_f$  temperature to be approximately 0°C. The steel substrates were placed within the sputtering chamber and the air was then evacuated. During sputtering, the system was kept at a base pressure of  $1 \times 10^{-7}$  mbar and argon gas was pumped through the system at a rate of 20 cm<sup>3</sup> per minute [7]. This process was carried out by AQUANDAS GmbH (Kiel, Germany).

### **3.2 Microstructural Characterization of Coatings**

All coatings were sectioned using a Buehler Isomet 1000 precision saw (Figure 3.4) with a cubic boron nitride saw blade to prevent mechanical and heat damage to the coating. The cross-sections of the coatings were examined using the Hitachi S-4700 scanning electron microscope (SEM), which operated at 15kV and 15 $\mu$ A. Furthermore, energy dispersive spectrometry (EDS) to determine the elemental compositions of the coatings.

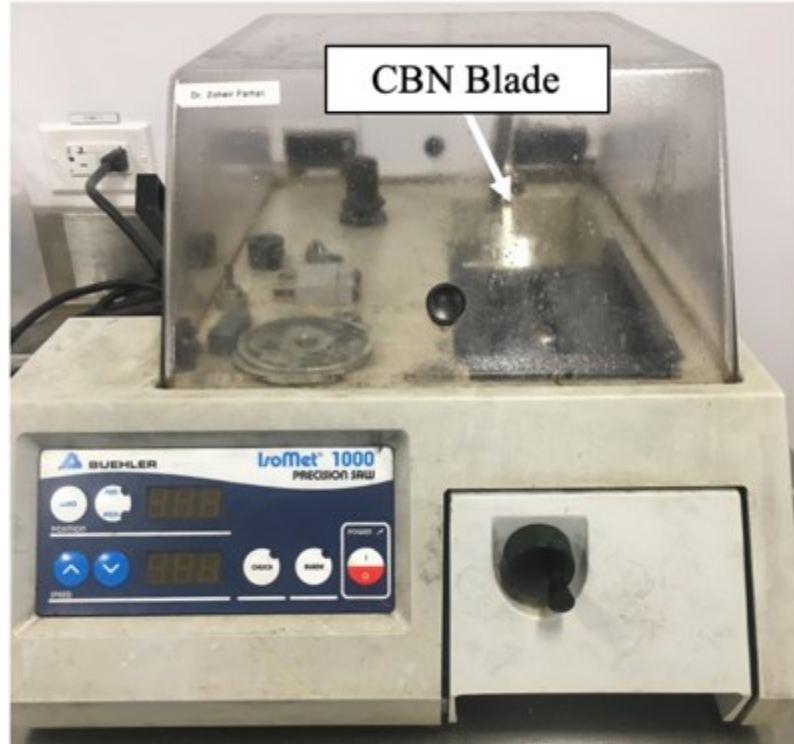


*Figure 3.4 – Buehler IsoMet 1000 precision saw*

The crystalline phases in the nanolaminates were determined through X-Ray Diffractometry (XRD) technique using a Bruker D8 advanced X-ray diffraction system with a Lynx-eye high-speed detector, shown in Figure 3.5, which operated at 40kV and 40mA. Each coating was analyzed using Cu K $\alpha$  radiation with a wavelength of 1.54 Å, from 20° to 120° (2 $\theta$ ), and generated peaks were identified using Powder Diffraction Files (PDF). The XRD tests were done using fast (5°/minute) and slow (0.5°/minute) scans. The slow scan was designed to detect low-intensity peaks.

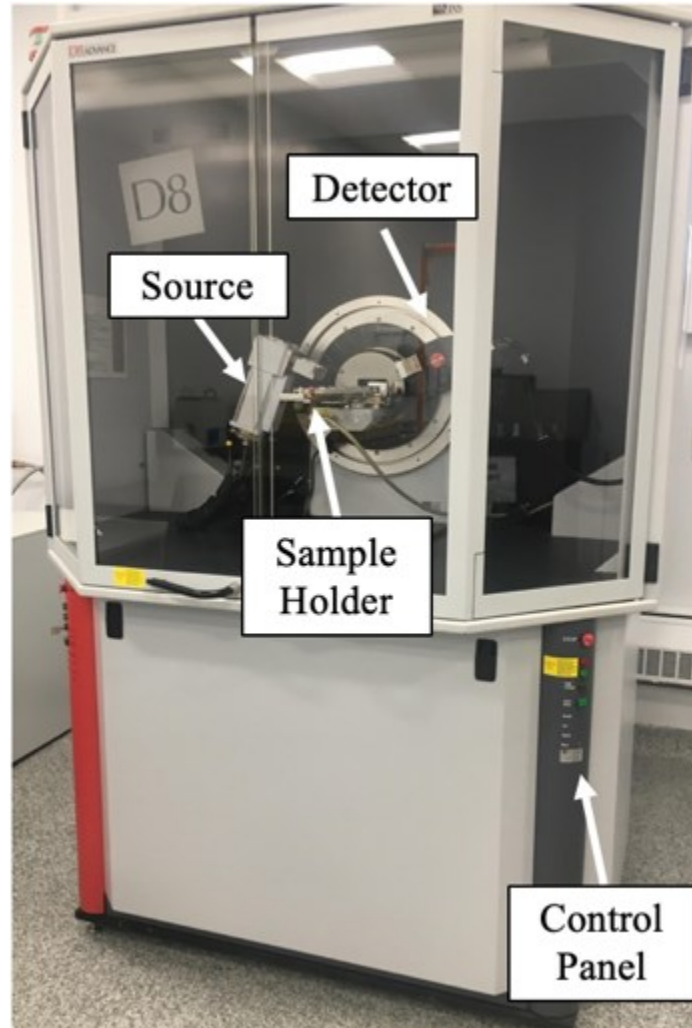


*Figure 3.5 – Bruker D8 advanced x-ray diffraction system*

Residual stresses, that may have developed during sputtering and annealing in the coating, were also analyzed through XRD technique at Proto Manufacturing Ltd. (Ontario, Canada). The equivalent and principal stress magnitude and orientation were determined by measuring the stresses at the surface in three directions ( $0^\circ$ ,  $45^\circ$ ,  $90^\circ$ ) for each annealing condition. The residual stresses were calculated according to the theory in Figure 3.6. Where  $D$  is the detector,  $S$  is the x-ray source,  $d_0$  is the unstressed lattice parameter,  $\sigma$  is the residual stress in the specimen,  $d_\psi$  is the interplanar distance at the angle  $\psi$ , and  $N$  is the direction normal to the surface.

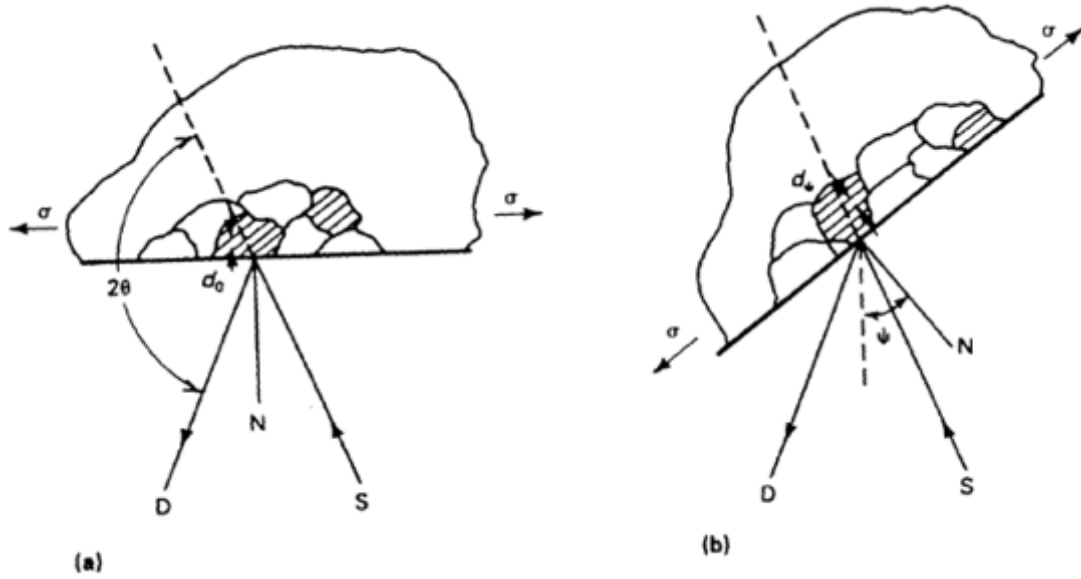


*Figure 3.6 – Principles of x-ray diffractometry stress measurement at an angle of a) 0° and b)  $\psi = \psi$  [103]*

The interplanar spacing,  $d$ , and the residual stress ( $\sigma$ ) is determined using Equation (9) and Equation (10), respectively. Where  $\lambda$  is the wavelength,  $\theta$  is the incident beam angle,  $\nu$  is the Poisson's ratio of the coating,  $E$  is the elastic modulus of the coating,  $d_\psi$  is the interplanar spacing at angle  $\psi$ , and  $\psi$  is the angle subtended by the bisector of the incident and diffracted beam. The elastic modulus and Poisson's Ratio of the coating were approximated, through the rule of mixtures, to be 192.5GPa and 0.33, respectively.

$$n\lambda = 2d \sin \theta \quad (9)$$

$$\sigma = \left[ \frac{d_\psi - d_0}{d_0} \right] \left[ \frac{E}{1 - \nu} \right] \left[ \frac{1}{\sin^2 \psi} \right] \quad (10)$$

### 3.3 Nanoindentation Testing

Load-controlled nanoindentation was performed in a progressive multicycle testing format with a Berkovich diamond indenter at the Material Properties Assessment Laboratory at McMaster University (Ontario, Canada). A single multicycle test applied loads of 5mN, 10mN, 15mN, 20mN, and 25mN to the coating; this process was repeated 10 to 15 times on different locations on the coating. During a cycle, a specific load was applied at a rate of 50 mN per minute, held for 10 seconds, subsequently unloaded at a rate of 50 mN per minute to 3 mN, and then the same location is loaded once more with the next higher load.

The elastic modulus and hardness values were determined from load-depth curves, seen in Figure 3.7, using the Oliver and Pharr method [104]. Where  $P_t$  is the applied load,  $h_t$  is the total depth of the indent, and  $dP/dh$  is the slope of the unloading curve. Hardness and elastic modulus values were recorded under each load, for a total of 5 values per test.

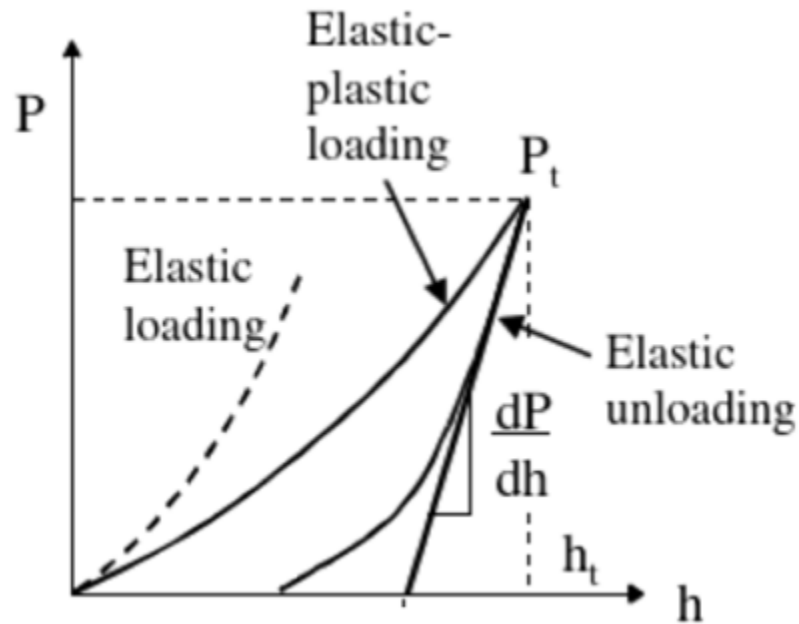


*Figure 3.7 – Typical nanoindentation load-depth curve [105]*

The hardness of the coatings was calculated using Equation (11) where  $H$  is hardness,  $h_c$  is the contact indentation depth, and  $k$  is a constant which assumes the value of 24.5 for a Berkovich indenter.

$$H = \frac{P}{kh_c^2} \quad (11)$$

The contact depth,  $h_c$ , can be calculated according to Equation (12), where  $P_t$  is the maximum load.

$$h_c = h_t - \left[ \frac{2(\pi - 2)}{\pi} \right] \left[ \frac{P_t}{dP/dh} \right] \quad (12)$$

Elastic modulus is calculated using Equation (13), where  $E^*$  is the reduced modulus,  $E$  and  $\nu$  are the elastic modulus and Poisson's ratio for the coating, respectively. Likewise,  $E_i$  and  $\nu_i$  are the elastic modulus and Poisson's ratio for the indenter.

$$\frac{1}{E^*} = \frac{(1 - \nu^2)}{E} + \frac{(1 - \nu_i^2)}{E_i} \quad (13)$$

The reduced modulus,  $E^*$ , can be found using Equation (14) where the load supporting area is denoted by  $A$ .

$$E^* = \frac{dP}{dh} \frac{1}{2} \frac{\sqrt{\pi}}{\sqrt{A}} \quad (14)$$

### 3.4 Scratch Testing

Scratch tests were performed using a Universal Micro Tribometer (UMT) at room temperature conditions, the testing set-up can be seen in Figure 3.8. The scratch test was

performed with a 0.4 mm diamond tip indenter; which has a hardness, elastic modulus, and Poisson's ratio of 41.19GPa, 1050GPa, and 0.18, respectively [106]. Constant loads of 0.5kgf, 1kgf, 2kgf, 3kgf, and 4kgf were applied for 30 seconds over a sliding distance of 5 mm. Multiple passes of a 1kgf load were applied over the same 5mm scar for a total sliding distance of 5mm, 25mm, 50mm, 100mm, and 200mm. Increasing load tests were performed by applying a force from 0.05kgf to 4.5kgf over a sliding distance of 10mm in a 60-second interval. Each test was accompanied by an acoustic emission sensor to aid in determining critical loads. The scars were further analyzed using SEM, EDS, and a Keyence confocal laser microscope.

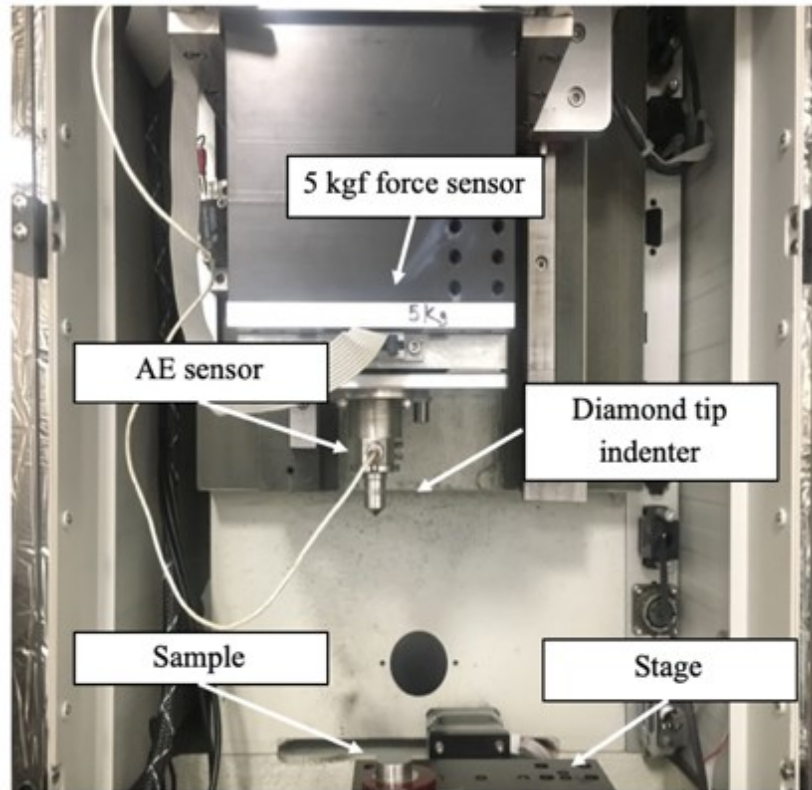


*Figure 3.8 – Scratch test apparatus*

The volume loss from scratch tests of the coatings was calculated using an area measurement equation [76]. This relation can be seen in Equation (15), where the average width of the scar,  $b$ , is measured using an Olympus Model BX-51 optical microscope.

$$V = \frac{D^2 y}{8} \left[ 2 \sin^{-1} \frac{b}{D} - \sin \left( 2 \sin^{-1} \frac{b}{D} \right) \right] \quad (15)$$

Where  $V$  is the total volume loss,  $D$  is the diameter of the diamond indenter, and  $y$  the length of the scar. The wear rates of the coatings were calculated from the slope of the volume loss versus sliding distance plots.

### **3.5 Hertzian-Type Testing**

The nanolaminate coatings were subjected to Hertzian-type indentation testing at room temperature. This was performed using PASCO ME-8236 testing apparatus. A 1.59 mm tungsten carbide (WC – 6 wt.% Co) spherical ball indenter was used to apply loads between 600 N and 2500 N at a speed of 2 mm per minute. The WC indenter has a hardness, elastic modulus, and Poisson's ratio of 14.02GPa, 600GPa, and 0.21 respectively [106]. The test set-up can be seen in Figure 3.9. Displacement, time, and force were recorded and used to produce load-displacement curves, using PASCO Capstone V1.4.1 software. Each test was accompanied by an acoustic emission sensor to determine if any cracking occurred during testing. The indentations were analyzed using SEM, EDS, and a Keyence confocal laser microscope.

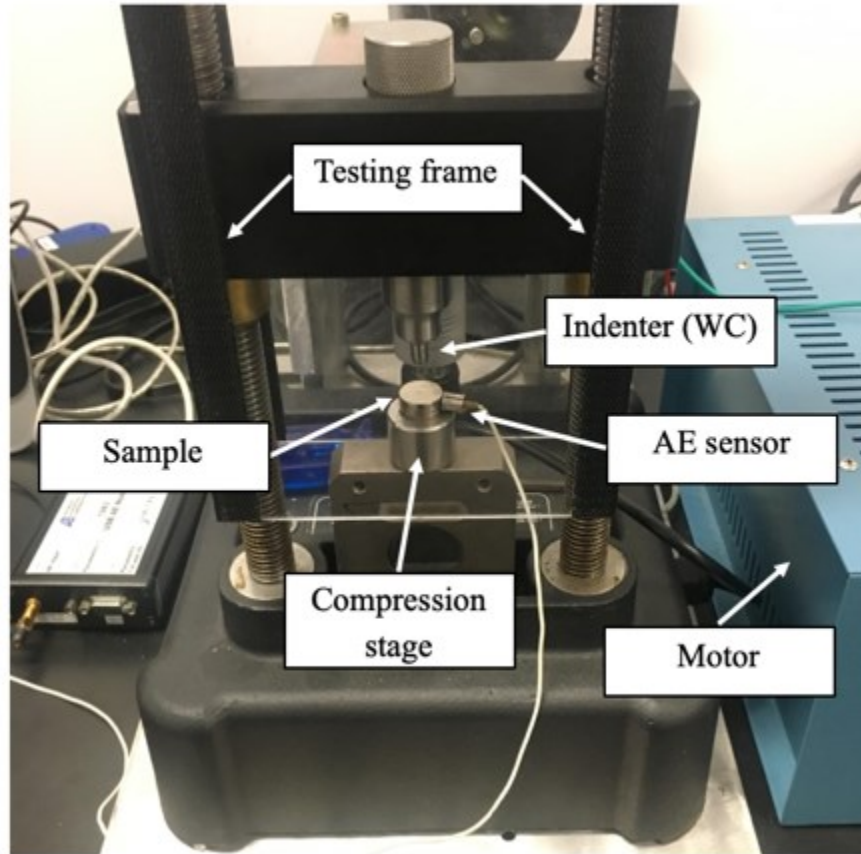


*Figure 3.9 – Hertzian- type indentation apparatus*

### **3.6 Single Particle Erosion Testing**

Single particle erosion was performed at room temperature using an in-house built apparatus, seen in Figure 3.10. A hard tungsten carbide (WC – 6 wt.% Co) spherical ball with a diameter of 1mm was placed into the receiver, then the bolt was connected to allow compressed air to fire it at the sample. The sample was loaded into the holder, placed in the vise, and then the impact angle of 90°, 60°, 45°, or 30° was chosen. The vise was then placed approximately 1cm away from the end of the barrel. After the safety enclosure was placed over the end of the barrel and vise, the pressure gage was set to a specific pressure and the solenoid valve was opened; allowing the compressed air to push the particle towards the target.

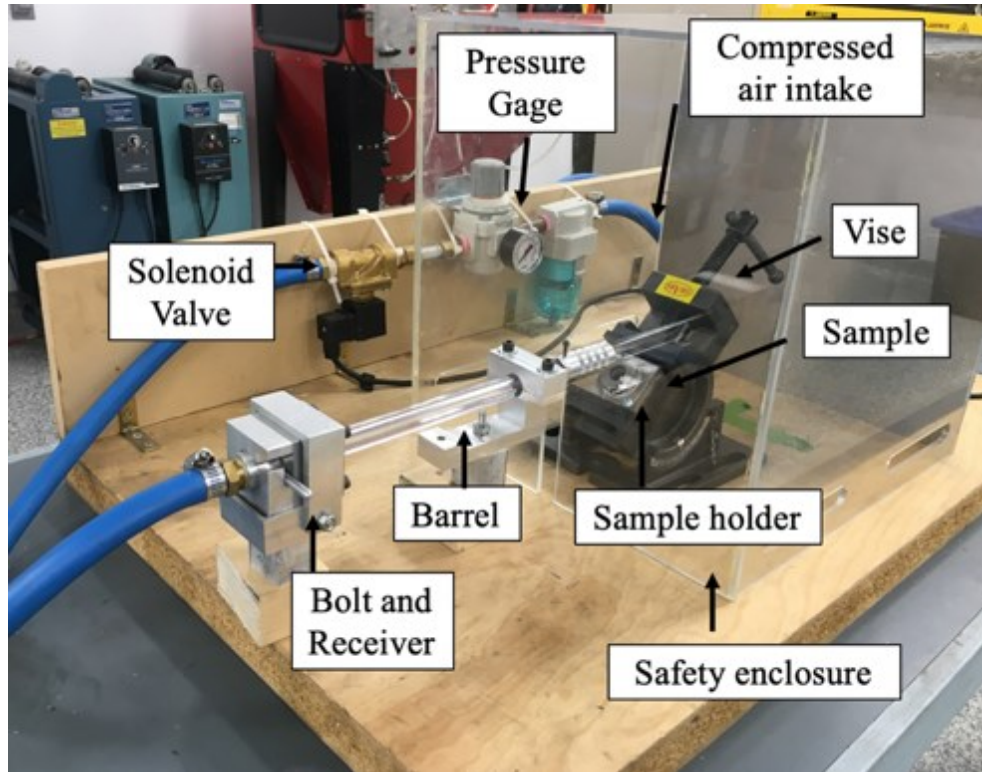


*Figure 3.10 – Single particle erosion apparatus*

The pressure gage could be adjusted to determine the velocity of the impacting particle. The velocity was measured by an Arduino that calculated the time needed for the particle to pass through two photo-interrupters that were placed 0.003m apart, the time was then inputted into Equation (16) to determine the velocity.

$$u_p(m/s) = \frac{\text{Distance between the photo interruptors (m)}}{\text{Time for particle to pass both the photo interruptors(s)}} \quad (16)$$

In this study, a pressure of 60psi was selected, to ensure that the mean contact force is above that needed to initiate the NiTi transformation; which was determined to be 0.410GPa [2]. Using the calibration curve, Figure 3.11, a pressure of 60psi results in a velocity of approximately 53m/s. The impact sites were analyzed using SEM, EDS, Keyence laser confocal microscope, and an Olympus Model BX-51optical microscope.

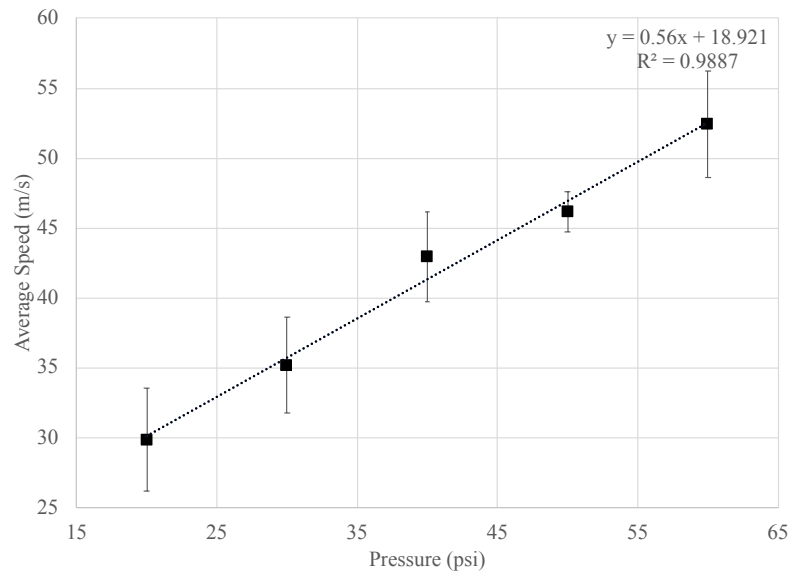


**Figure 3.11 – Calibration curve of single particle erosion tester**

## 4.0 Results and Discussion

### 4.1 Fabrication and Characterization of Coatings

#### 4.1.1 *Design and Fabrication of the NiTi Nanolaminate Coatings*

The nanolaminate coatings were designed to obtain the NiTi intermetallic phase through the solid-state diffusion of the Ni and Ti layers. The lack of studies on the formation and growth of the NiTi phase proves to be problematic when designing the coating; therefore, the coating is design based on diffusion couple literature [30]–[33]. In semi-infinite diffusion couple studies, there are infinite amounts of both Ni and Ti atoms, which ensures the reaction will not be hindered by the depletion of Ni or Ti. The semi-infinite condition eliminates some of the complexities in interpreting the results.

Therefore, within the nanolaminate structure, it is vital that the thicknesses of the layers behave in a similar manner to that of a semi-infinite diffusion couple. The thickness of the layers in the coating must exceed the expected reaction zone thickness, noting diffusion will occur on both sides of the Ni and Ti layers. The reaction zone in Ni and Ti nanolaminate coatings, under similar annealing conditions used in this study, was observed to be 10nm to 30nm by Cho *et al.* [107]. Thus, Ni and Ti were deposited in alternating 100nm thick layers to ensure that the semi-infinite diffusion couple condition is achieved.

The thickness of the Ni and Ti layers can be seen in the cross-section of the as-sputtered nanolaminate, which was examined under a Helium Ion Microscope (HiM), as seen in Figure 4.1. The image shows approximately 100nm thick layers of both Ni and Ti and intimate contact between each layer which is required for uniform diffusion during annealing. The black lines indicate the approximate locations of the Ni-Ti interfaces where the intermetallic phases should form.

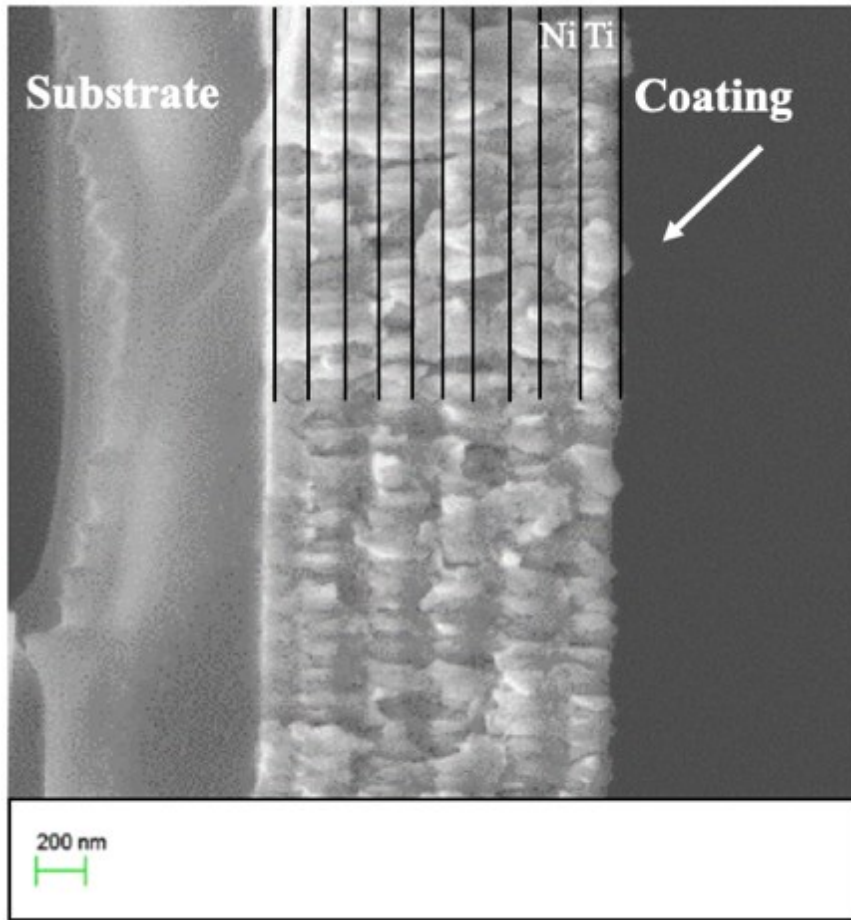


**Figure 4.1 – HiM image of the as-sputtered coating**

To further confirm that Ni and Ti were deposited in equal volumetric amounts, ICP-OES was performed on the as-sputtered coating, the results of which are listed in Table 4.1. The main elements found in the coating were Ni, Ti, and Fe. There are also trace amounts (<0.5 wt.%) of tungsten, zinc, and aluminum from the substrate. Although the overall coating Ni to Ti atomic ratio is 1.64, in the vicinity of the Ni-Ti interface, where the reaction takes place, the ratio is 1 as a consequence of the semi-infinite diffusion couple condition.

**Table 4.1 – ICP composition of as-sputtered laminate coatings**

Percentage	Elements					
	Ni	Ti	Fe	W	Zn	Al

Weight	62.44 %	30.88 %	2.75 %	<1 %	<1 %	<1 %
Atomic	59.01 %	35.78 %	2.74 %	<1 %	<1 %	<1 %
Volume	47.82 %	46.75 %	2.39 %	<1 %	<1 %	<1 %

After annealing, the reaction zones could not be clearly identified using SEM. However, the SEM image in Figure 4.2 clearly shows the nickel-rich (dark) and titanium-rich (light) layers. EDS mapping of the nanolaminate shows that the Ni and Ti layers were evenly distributed within the coating. Noting that there are no traces of Fe, which means there was no effect of the substrate during the annealing process.

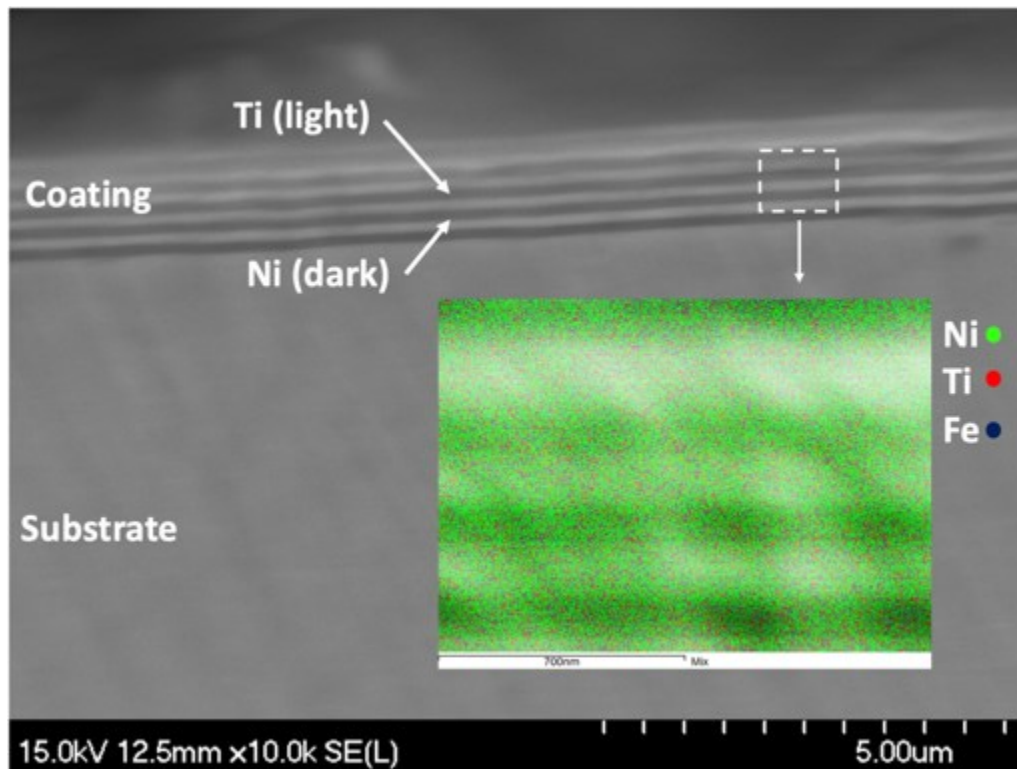


*Figure 4.2 – Mixed EDS map of nanolaminate coating annealed at 650 °C*

#### **4.1.2 XRD of Nanolaminate Coatings**

XRD patterns, seen in Figure 4.3, were gathered from each annealed coating to determine if any intermetallic phases were formed during annealing, specifically austenitic NiTi. As-sputtered and 150 °C data both show a peak at 38° (2θ) which was identified as the Ti

(002) peak. This peak does not appear in samples annealed above the 150 °C, indicating a reaction between Ti and Ni to create intermetallic phases. That is, the amount of Ti is reduced to a level where it is difficult to observe its corresponding peaks. The coatings annealed at 650°C and 800°C show the NiTi (110) intermetallic peak at 44° (2θ), demonstrating that superelastic austenitic NiTi is formed at these temperatures. The Fe (110), (200), and (211) peaks from the substrate are clearly seen in all nanolaminate coatings. It is difficult to see the Ni (111) peak as it overlaps with the strong Fe (110) peak, however, the Ni (200) is slightly visible.

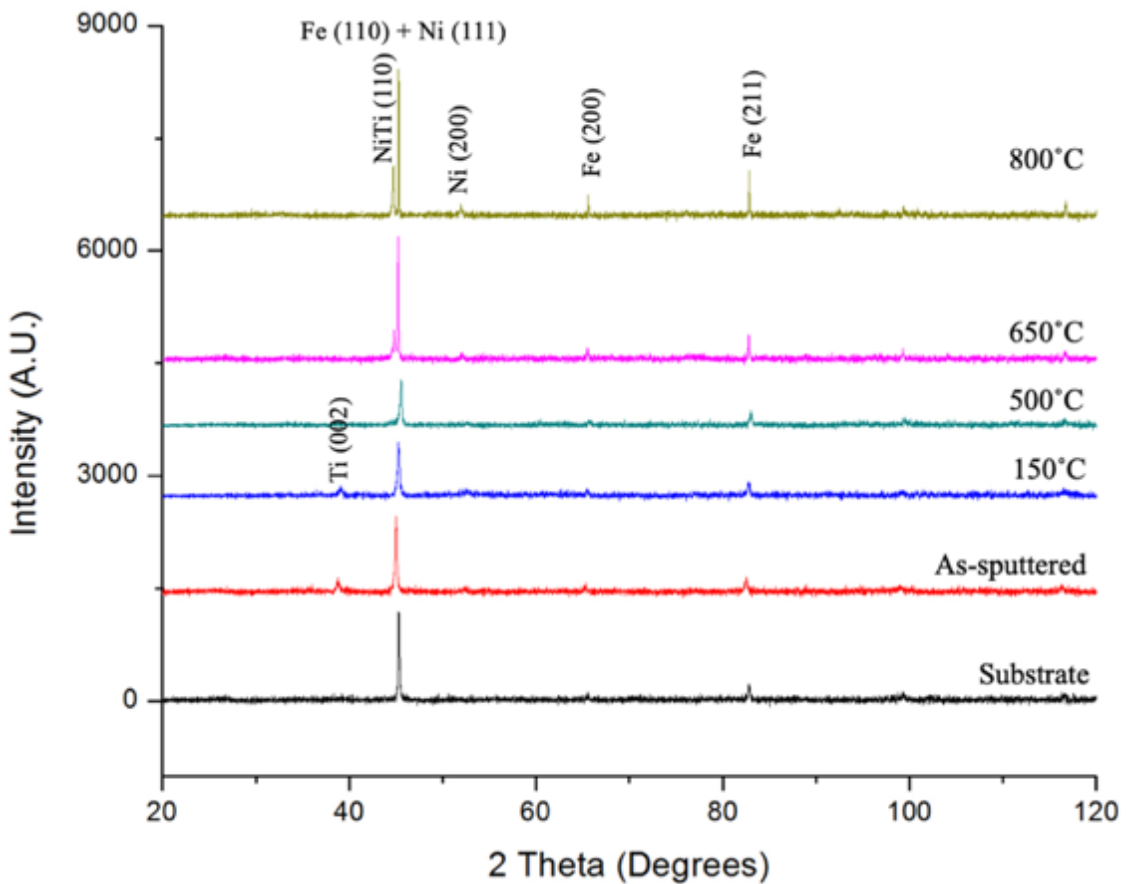


**Figure 4.3 – XRD patterns of as-sputtered and annealed nanolaminate coatings and substrate**

According to the Ni-Ti phase diagram (Figure 2.1), Ni and Ti should also form the NiTi<sub>2</sub> and Ni<sub>3</sub>Ti intermetallic phases. A close examination of the slow scan XRD diffraction patterns in the 2θ range of 44° to 45° for the 650 °C and 800 °C coatings show a

combination of the three intermetallic phases. It is clear from Figure 4.4 that the  $\text{NiTi}_2$ ,  $\text{NiTi}$ ,  $\text{Ni}_3\text{Ti}$  intermetallic phases have formed during annealing.

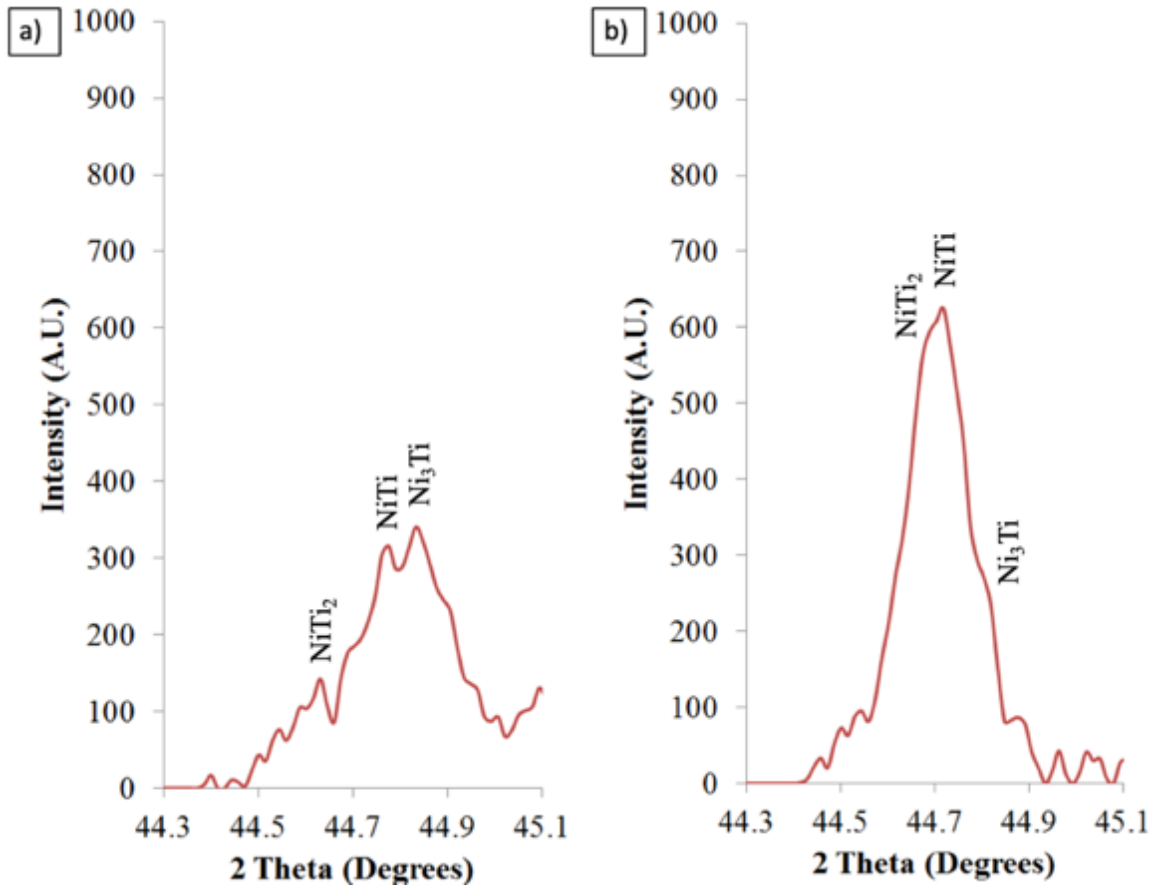


*Figure 4.4 – Slow XRD scans of a) 650°C and b) 800°C nanolaminate coatings*

The results of the residual stress analysis show the evolution of the stress during the annealing of the Ni-Ti nanolaminate composite coatings. It is clear from Figure 4.5 that the sputtering process has induced residual stresses in the coating. It is likely that these stresses have developed as a result of thermal stresses during sputtering [50]. As the coating is annealed to 150°C and slowly cooled, stresses are slightly relieved, as expected. Upon annealing to 500°C, the residual stresses increase rapidly to a value of 500MPa, which is double that of the 150°C coating. Further, annealing at 650°C and 800°C causes a rapid drop in the residual stress.

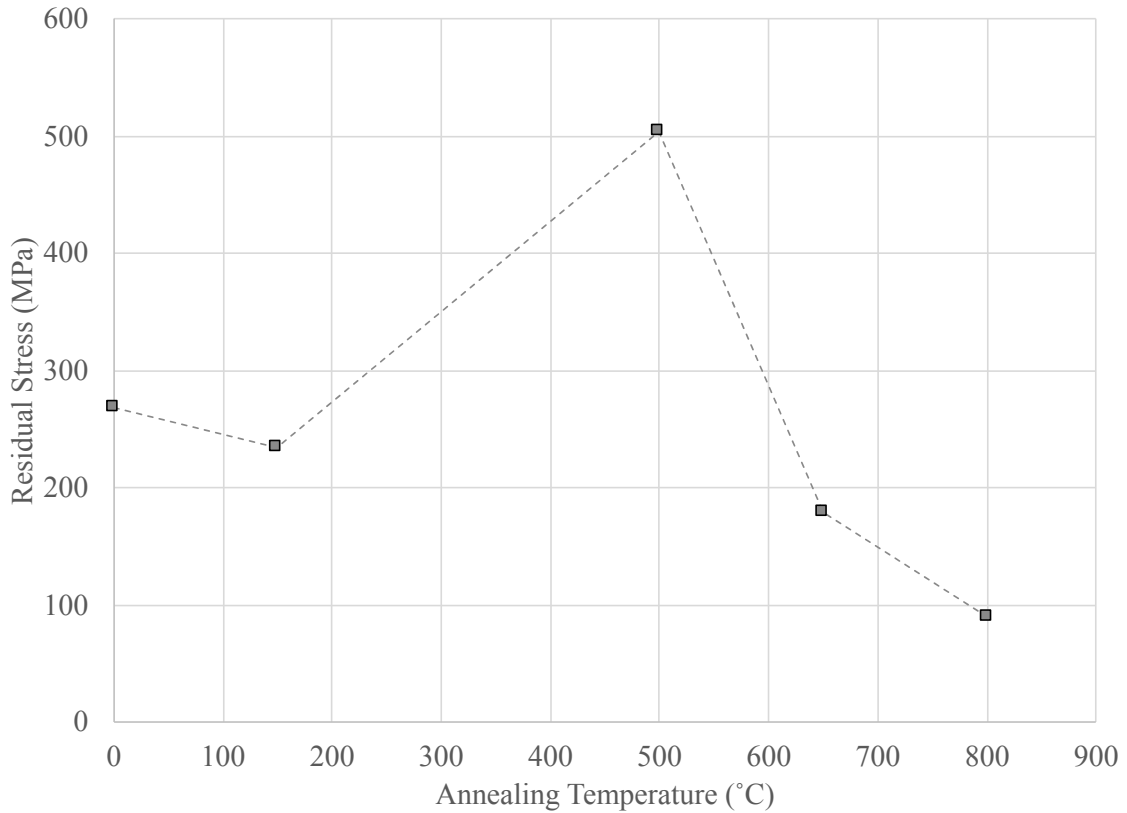


**Figure 4.5 – Equivalent stresses as a function of annealing temperature**

The macro-strain, hence residual stresses, development in the nanolaminates is believed to be a result of solid solution formation due to the diffusion and coherency state of the precipitates. As annealing temperature increases from 150°C to 500°C precipitates in the form  $Ni_xTi_y$  form and grow. These precipitates are originally coherent with the matrix [57]; which increases the energy of the coatings due to interfacial “mismatch” between the different adjacent structures, causing a strain field in the material. When annealed at a higher temperature (i.e. 650°C and 800°C), the equilibrium NiTi precipitates forms and as the size increases the NiTi precipitate loses coherency with the matrix. The NiTi precipitate would reach a critical size in which the interface stresses increase surpassing the strength of the matrix, this results in breaking the bonds to the surrounding structures [57]; as the precipitate becomes incoherent (or semi-coherent) residual stresses decrease. Based on the residual stress results (Figure 4.5) and XRD patterns (Figure 4.3) the NiTi phase is believed to have first formed as a fine, coherent, precipitate at an annealing temperature higher than 500°C and lower than 650°C.

When an intermetallic phase (i.e. NiTi) precipitates, there will be additional stresses in the matrix depending on the coherency state of the phase [55]. Material properties of the individual layers in the coating, Table 4.2, reveals that Ni is twice as dense as Ti and a similar trend can be seen in the elastic modulus. Furthermore, the coefficient of thermal expansion (CTE) values shows about a 30% difference between the Ni and Ti layers. These properties affect the coherency state of the growing precipitate; however, the main influence is the lattice parameter. Superelastic austenitic NiTi has a reported lattice parameter of 3.01 Å [108], meaning when NiTi precipitates it has some coherency with the matrix due to the - 14 % and + 2 % difference in lattice parameters between Ni and Ti, respectively. It is important to note that thermal stresses; due to the difference in CTE values between the adjacent Ni and Ti layers, may have also contributed to the rise in residual stress between 150°C and 500°C. However, it is believed that the thermal stresses contribution to the overall residual stress is small and would not account for the high rise in residual stress at 500°C, especially that the heating and cooling rates during annealing were low.

**Table 4.2 – Material properties of individual layers in the laminate and substrate**

Elements	Ni (FCC)	Ti (HCP)
Density (g cm <sup>-3</sup> )	8.90 [109]	4.51 [109]
Young's Modulus (GPa)	227.7 [2]	111.0 [2]
Lattice Parameter (Å)	3.52 [109]	a = 2.95 c = 4.68 [109]
CTE (µm m <sup>-1</sup> K <sup>-1</sup> )	13.3 [109]	8.41 [109]

Based on the XRD (Figure 4.3) and residual stress (Figure 4.5) analysis, EDS was used to identify intermetallic precipitates that have formed during annealing at 650°C. Locations within the expected reaction zone in the 650°C nanolaminate, shown in Figure 4.6, between the original Ni and Ti interface were examined. The results show that approximately equiatomic NiTi precipitates have formed within the reaction zone, which is in agreement with XRD data.

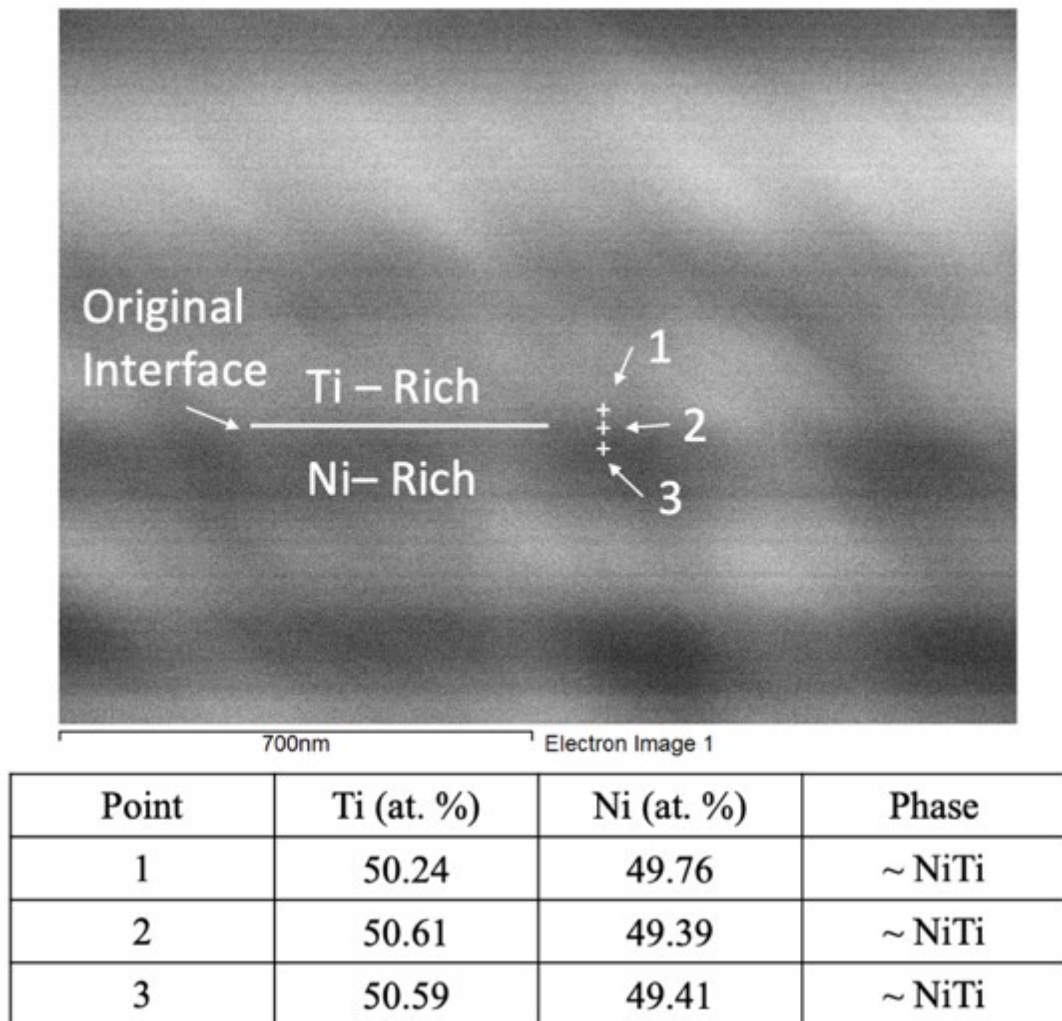


**Figure 4.6 – EDS composition of 650°C nanolaminate**

It is believed that the intermetallic phases form and grow in a very specific sequence. Hu *et. al* [30] and Garay *et. al* [35] proposed that the Ni<sub>3</sub>Ti phase forms first, followed by the NiTi<sub>2</sub> phase, and finally the NiTi phase, which is illustrated in Figure 4.7. Since Ni has the ability to diffuse faster into Ti [34], [36] compared to the reverse, the Ni<sub>3</sub>Ti will form first at the interface. Next, Ni diffuses through the new intermetallic layer to reach the Ti to form NiTi<sub>2</sub>. Hu *et al.* [30] report that the NiTi phase forms by two reactions: first is the reaction between the NiTi<sub>2</sub> and Ni<sub>3</sub>Ti interface, the other reaction is from the Ti atoms reacting with the Ni<sub>3</sub>Ti phase [30]. Resulting in the NiTi phase growing at the expense of the Ni<sub>3</sub>Ti intermetallic phase. As each of the layers form, the phase will continue to grow

and local equilibrium is established at the interfaces [35]. As the diffusion of the atoms proceeds, the Ti – Ni<sub>3</sub>Ti interface shifts towards the Ti layer, due to the imbalances of diffusivities as a result of the Kirkendall effect [47].

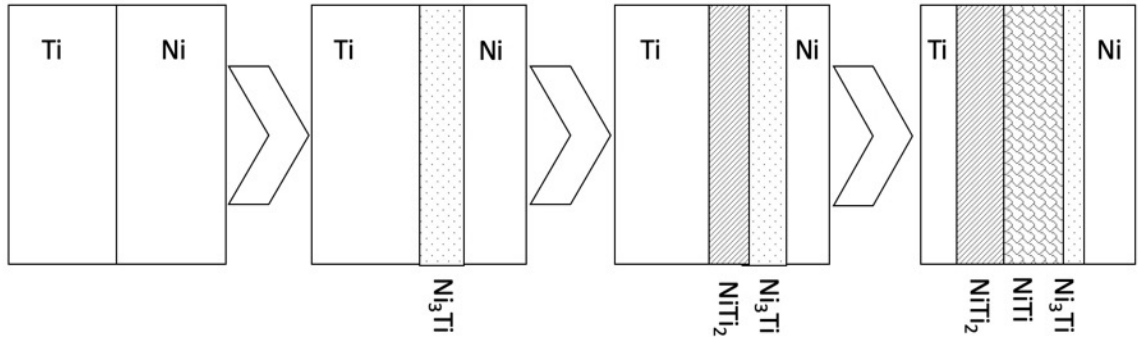


**Figure 4.7 – Schematic of the diffusion process of Ni and Ti**

The cross-section of two nanolaminates can be seen in Figure 4.8. Residual stresses may result in the delamination of the coating from the substrate [110]. After cutting the as-sputtered coating, there are locations where the coating had delaminated from the substrate. However, the coating that was annealed at 650 °C and then sectioned shows there is no delamination between the substrate and coating, signifying that annealing the coatings to form the intermetallic phases improve the overall toughness of the coating.

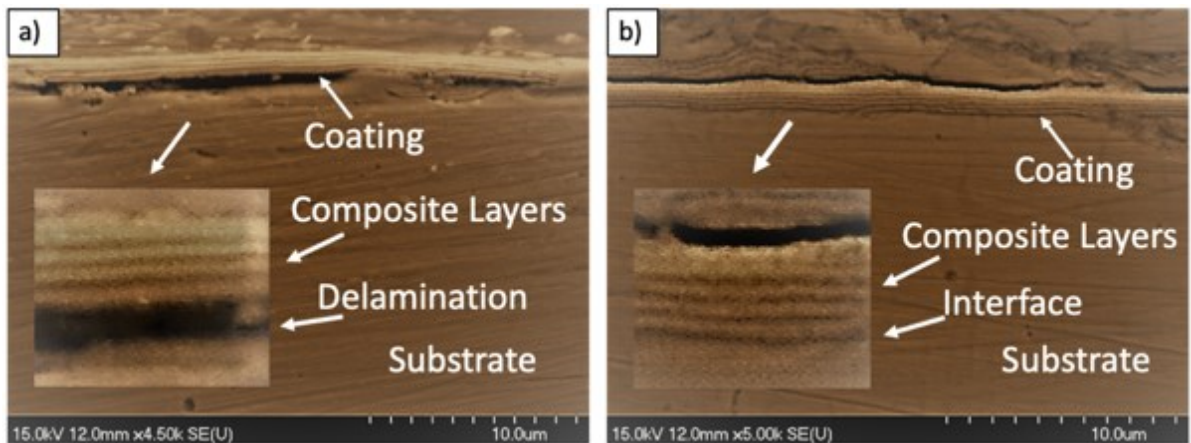


**Figure 4.8 – SEM cross-sections images of a) as-sputtered and b) 650°C**

### 4.1.3 Characterization of Monolayered NiTi Coating

A 50 $\mu\text{m}$  monolayered superelastic NiTi coating was also fabricated through DC magnetron sputtering. The cross-section of the superelastic NiTi coating, Figure 4.9, showed that NiTi was sputtered uniformly; however, the cross-section shows that the coating has a rough finish. When sectioning, the stress exerted by the saw blade was sufficient enough to initiate the NiTi phase transformation, resulting in increased wear on the blade and a rough surface finish. This further highlights the main challenge associated with machining and forming superelastic NiTi.

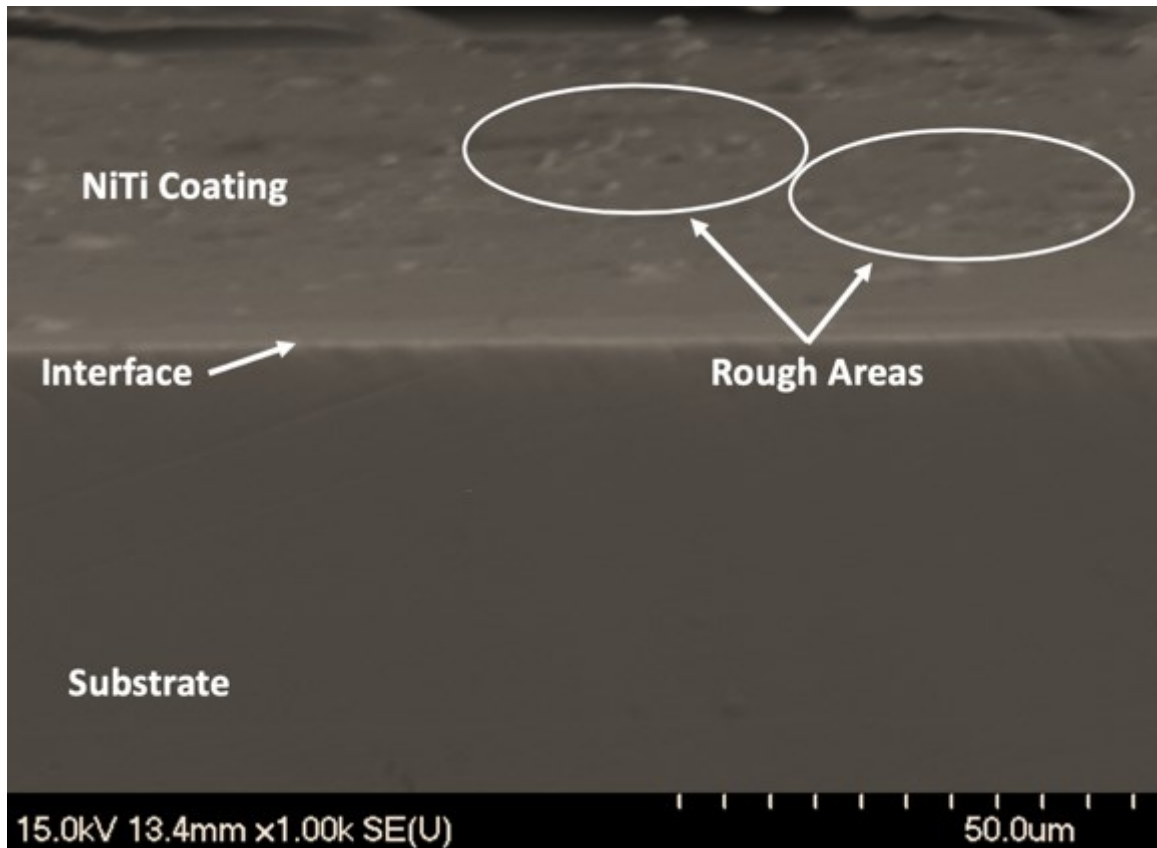


*Figure 4.9 – SEM cross-section image of superelastic NiTi monolayer coating*

The composition of the monolayer NiTi coating was determined through EDS analysis to be 50.58 at.% Ni and 47.23 at.% Ti. The superelasticity effect is sensitive to composition; however, increasing Ni concentration will decrease the transformation temperature [7].

This will suppress the austenitic start temperature to approximately 0°C, which renders the coating superelastic at room temperature, as was specified prior to sputtering.

The crystalline phases of the NiTi monolayer can be seen in Figure 4.10. The austenitic NiTi (110) peak, in the monolayered coating, was found to be shifted slightly to the left due to residual stresses within the coating. Typically, stresses arise during sputtering from the high kinetic energy of the ions bombarding the target as a result of sputtering conditions (i.e. gas pressure and plasma power) [111]. The superelastic NiTi coating pattern also shows another peak that was identified to be the R-Phase (110) peak [10], [112].

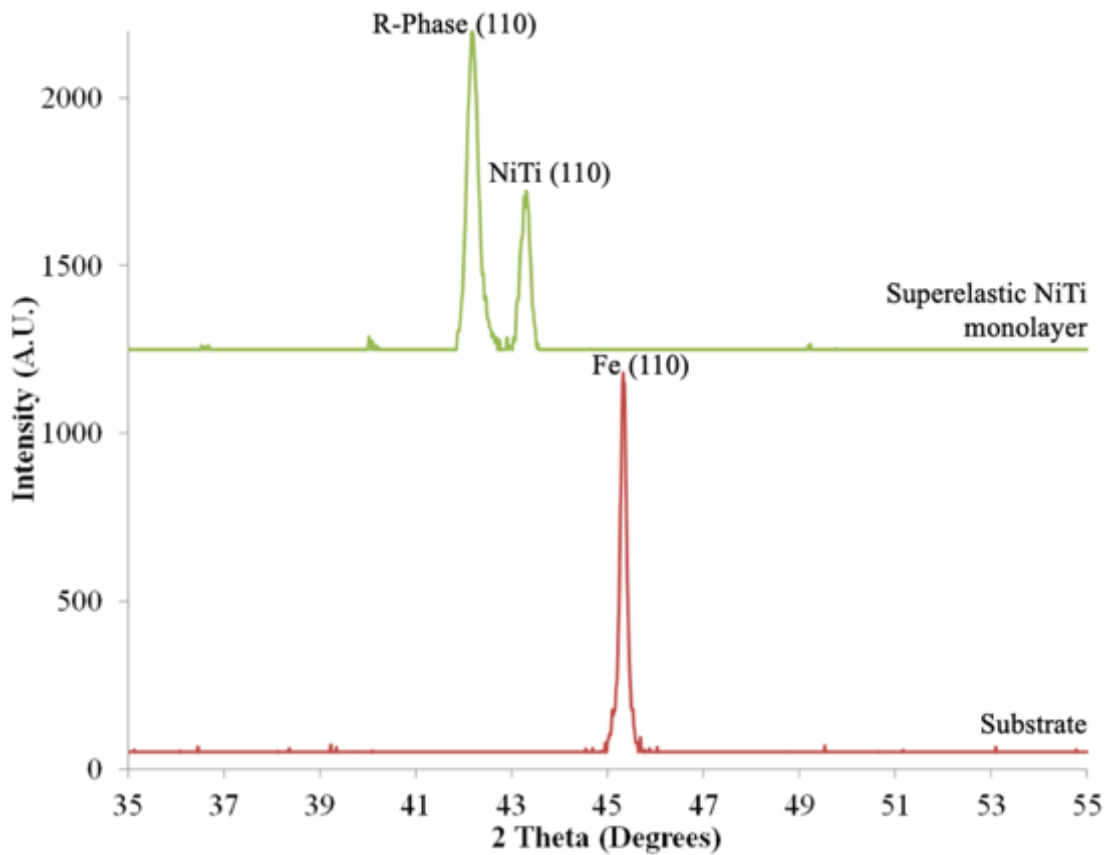


*Figure 4.10 – XRD patterns of monolayered superelastic NiTi and steel substrate*

#### 4.1.4 Nanoindentation Hardness and Elastic Modulus of the Coatings

Prior to nanoindentation testing, it was necessary to determine the surface roughness values for the coatings, the results of which are shown in Figure 4.11. Increasing surface roughness increases the scatter in nanoindentation data [113]. The roughness values between the 650°C nanolaminate and monolayer of NiTi are comparable while the other nanolaminates showed larger values. All roughness values are within acceptable limits for nanoindentation tests.

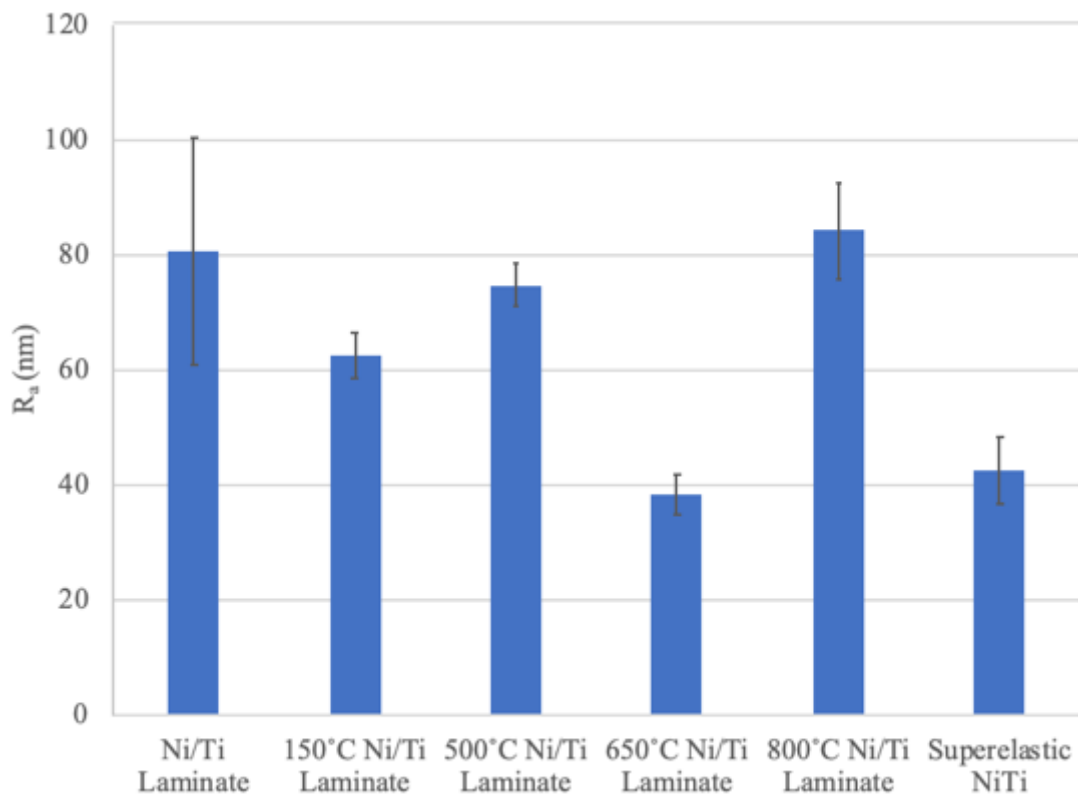


**Figure 4.11 – Surface roughness of the nanolaminate and monolayer of NiTi coatings**

Nanoindentation was performed to further characterize the as-sputtered, 650 °C, and 800 °C nanolaminates and the monolayered superelastic NiTi coating, the load-depth curves can be seen in Figure 4.12(a), (b), (c), and (d), respectively. The nanolaminates annealed at 150°C and 500°C were excluded due to the lack of NiTi precipitates. The plots in Figure 4.12 show typical load-depth curves. These are representative curves obtained

from single locations on each of the coatings. The tests were repeated on 10 to 15 locations on each coating to ensure accuracy. More curves can be found in the Appendix. The 650°C and 800°C nanolaminates, and monolayer NiTi show significant elastic recovery when unloading between cycles. The increase in elastic recovery is likely due to the superelastic NiTi phase that is present in the coatings. On the other hand, the as-sputtered coating in Figure 4.12(a), which has no superelastic NiTi phase exhibits lower elastic recovery.

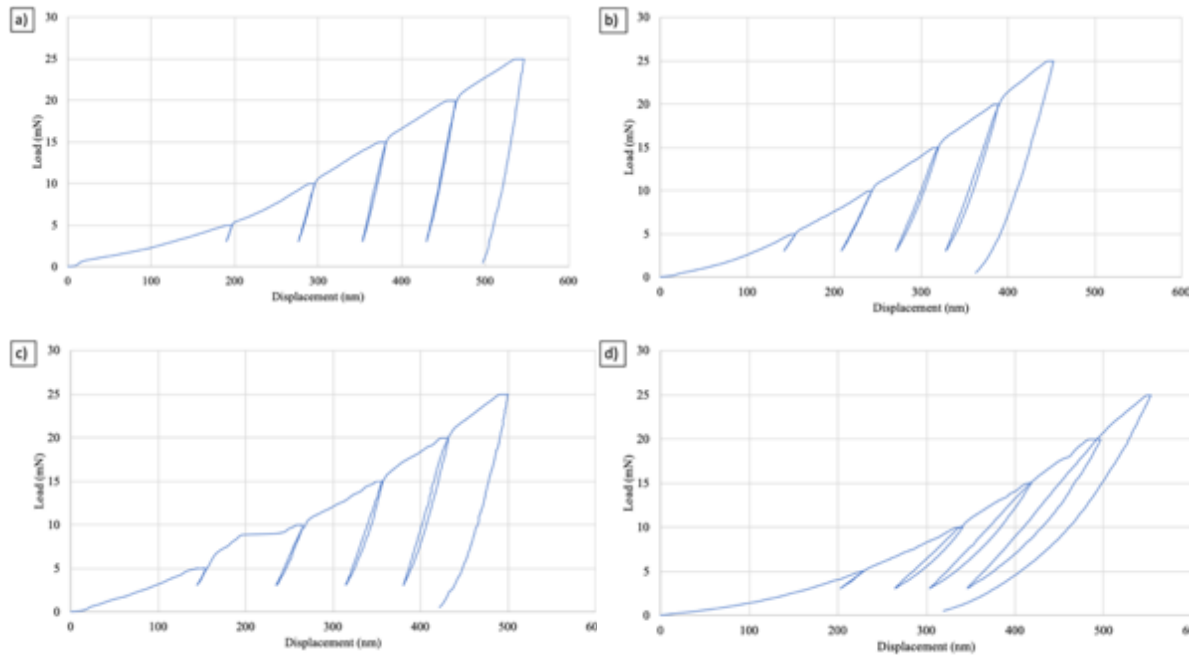


**Figure 4.12 – Nanoindentation curves for a) as-sputtered b) 650°C c) 800°C d) superelastic NiTi coatings**

From the nanoindentation plots in Figure 4.12 (and those in the Appendix) the hardness and elastic modulus values were calculated and curves were generated by plotting all values reported from nanoindentation under all loads, given in Figure 4.13 and Figure 4.14. These curves show that at low depths the hardness and elastic modulus values are significantly greater for all coatings, which is typical in nanoindentation data [58]. To determine the hardness and elastic moduli of the coatings, the data was fit to a power-law equation of the form  $y = Ax^n$ , where A and n are best-fit coefficients. The 650 °C and 800 °C nanolaminate coatings and superelastic NiTi coating follow the power-law

relationship closely, whereas the as-sputtered nanolaminate shows more scatter in the data.

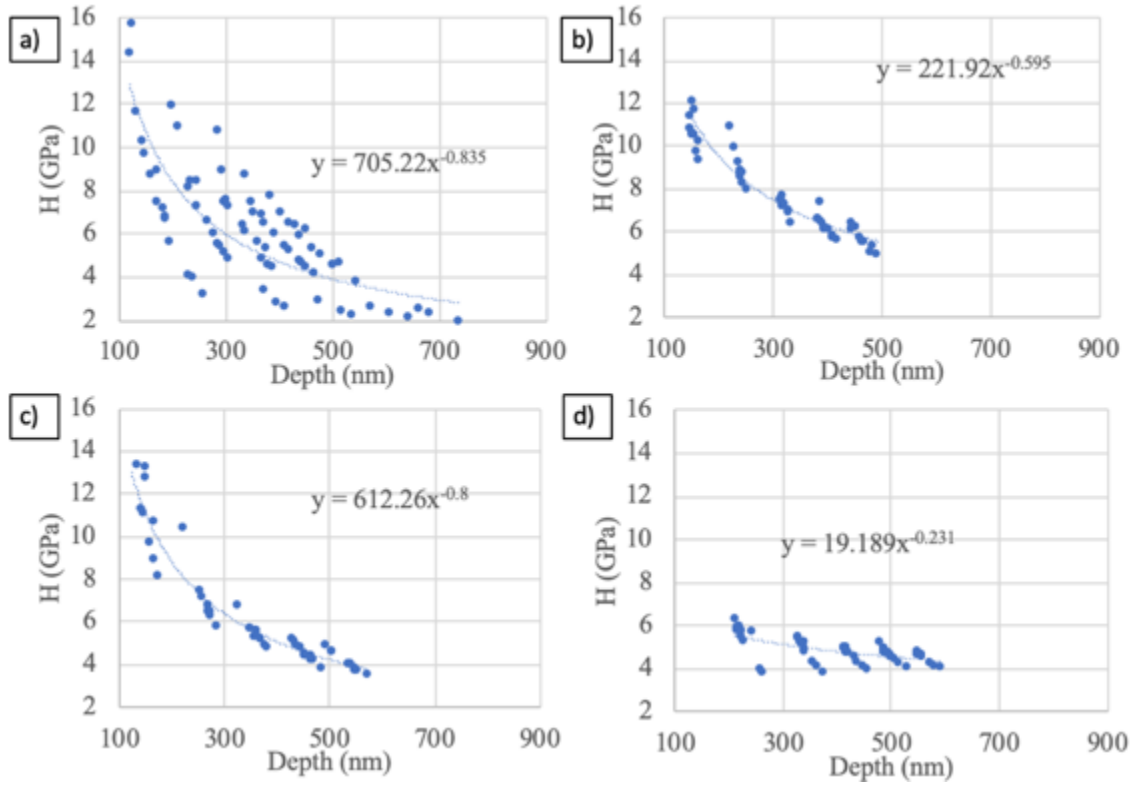


**Figure 4.13 – Hardness data for a) as-sputtered b) 650°C c) 800°C and d) superelastic NiTi coatings**

The elastic modulus values for each coating can be seen in Figure 4.14. Similar to the hardness data, the as-sputtered nanolaminate data widely scatters from the power-law trend compared to all the other coatings.

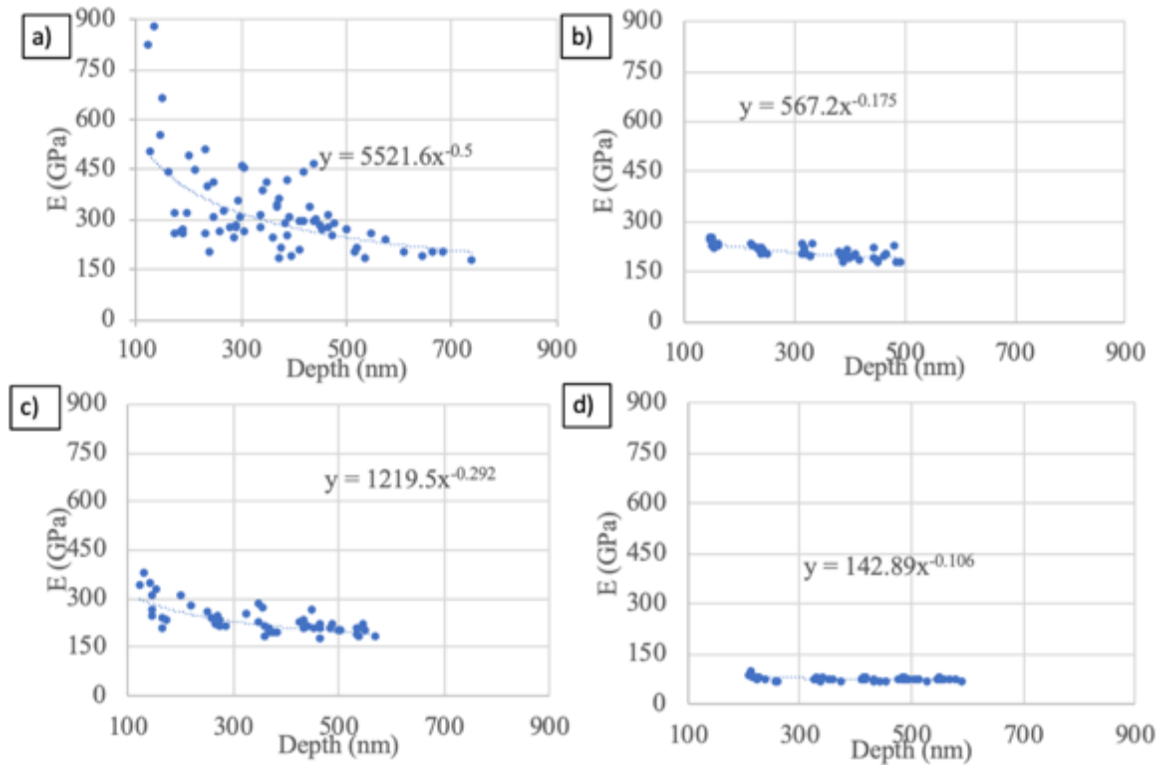


**Figure 4.14 – Elastic moduli data for a) as-sputtered b) 650°C c) 800°C and d) superelastic NiTi coatings**

To minimize the substrate effect when determining the hardness and elastic moduli of the coatings, the maximum indentation depth should not exceed 10 % to 20 % of the coatings total thickness; this is difficult in multilayered thin films. Therefore, the values of  $H$  and  $E$  are determined from best-fit equations at a depth of 200 nm, which is shown in Figure 4.15. It should be noted that the  $H$  and  $E$  values of the NiTi monolayer coating is in agreement with the published data [2], [97], [106]. The nanolaminates possess higher elastic modulus values than the monolayer of NiTi. The nanolaminate coating annealed at 650°C has comparable values to that of the superelastic monolayer NiTi coating, the same cannot be said about the other nanolaminates. Furthermore, all the nanolaminates exhibit higher hardness values than the monolayer of superelastic NiTi. Specifically, the 650 °C nanolaminate coating is 1.5 times harder compared to the superelastic NiTi coating; while, the other nanolaminates have hardness values less than the 650 °C nanolaminate.

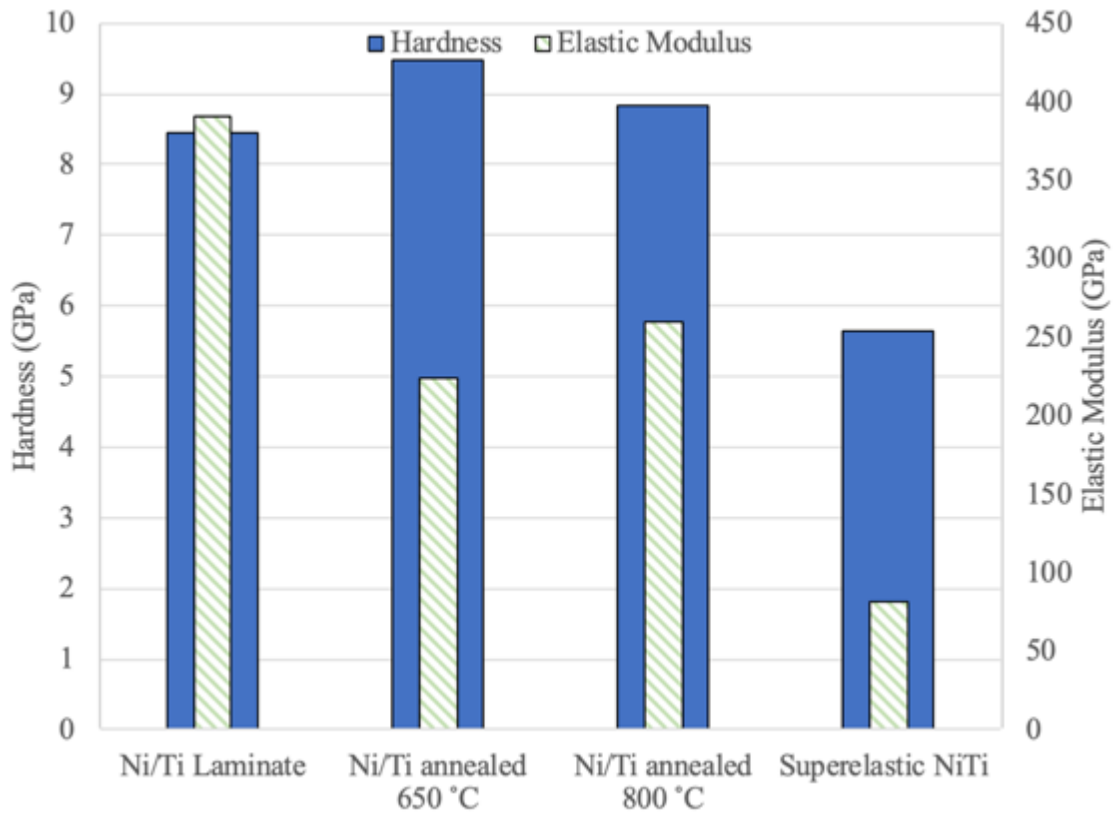


*Figure 4.15 – Hardness and elastic modulus values at a depth of 200nm*

The higher hardness in the nanolaminates can be attributed to the laminate structure of the coating. Laminates made with different materials will resist plastic deformation and brittle fracture [114]–[116]. According to Koehler [116], laminate structures are expected to have higher hardness due to the differences in elastic moduli between the layers. Koehler theory predicts that as dislocations in a low elastic modulus layer attempt to move into a layer of a higher elastic modulus it encounters resistance. Hence, hardness becomes proportional to the difference in the elastic moduli of the layers.

It is believed that the reason for the high hardness exhibited by nanolaminate annealed at 650°C is due to the large difference in elastic moduli between the NiTi layer and the adjacent Ti and Ni layers. Since the elastic modulus of the superelastic NiTi is much lower than the elastic modulus of Ti and Ni, Koehler strengthening mechanism will have a higher effect than in the as-sputtered Ni-Ti nanolaminate.

The elastic recovery ratios and E/H ratios for the as-sputtered, 650°C, and 800°C nanolaminates, and the monolayer of superelastic NiTi are displayed in Figure 4.16. The elastic recovery ratio for each coating is calculated through nanoindentation curves, by dividing the area beneath the unloading curve to the total area under the loading curve. The as-sputtered nanolaminate shows little recovery and a high E/H ratio, indicating poor wear resistance. The nanolaminate annealed at 650 °C shows comparable elastic recovery and E/H ratios to those of the superelastic NiTi monolayer coating.

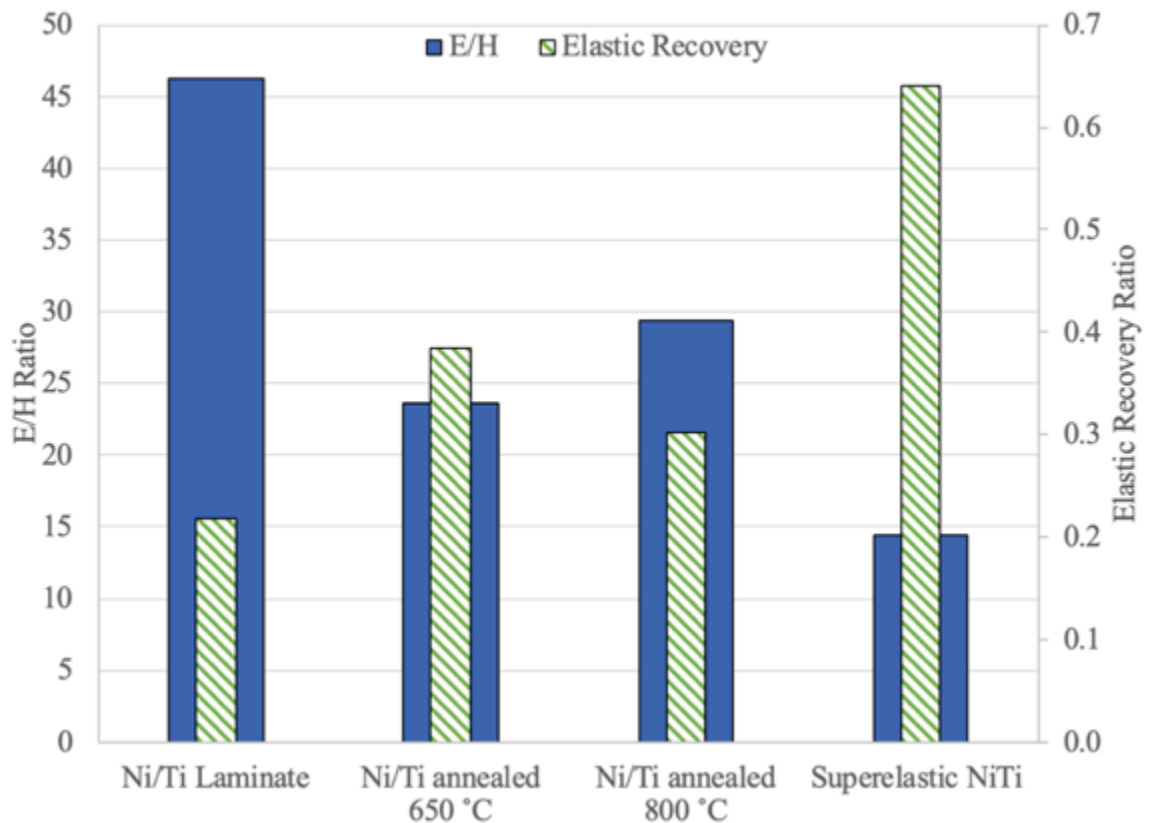


**Figure 4.16 – Elastic recovery and E/H ratios**

The  $H^3/E^2$  ratio was determined through the nanoindentation data, as seen in Figure 4.17. This ratio represents the resistance of the onset of plastic deformation in the coating [79]. Again, the superelastic NiTi and 650°C nanolaminate show comparable values to the superelastic NiTi monolayer, whereas the as-sputtered is much lower. This indicates that not only should the 650°C nanolaminate be resilient, but it should also resist plastic deformation as well.

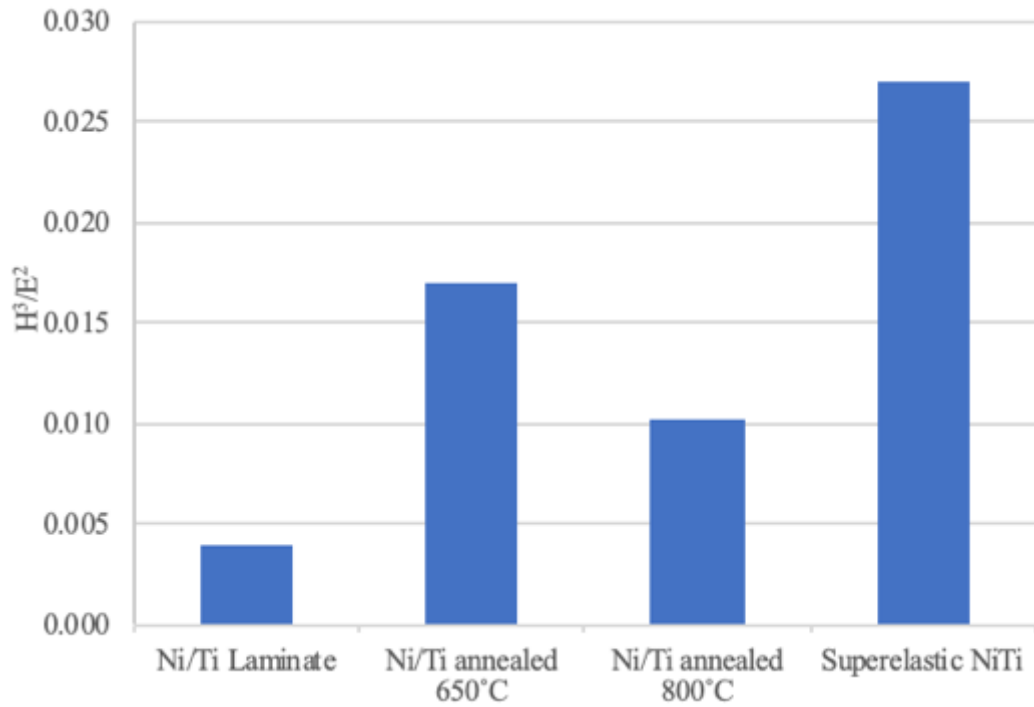


*Figure 4.17 –  $H^3/E^2$  ratio of the coatings*

## 4.2 Scratch Behavior of the Coatings

Scratch testing was performed to assess the wear damage of both the monolayer of superelastic NiTi and the Ni/Ti nanolaminate coatings. To assess if the NiTi phase could undergo transformation toughening, the contact area and the mean contact pressure were determined through Equation (2) and Equation (4), the results can be seen in Table 4.3. The initiation stress for the transformation was reported to be 0.410GPa [2]; therefore, transformation toughening can occur under all loads.

*Table 4.3 – Mean contact pressure during scratch testing*

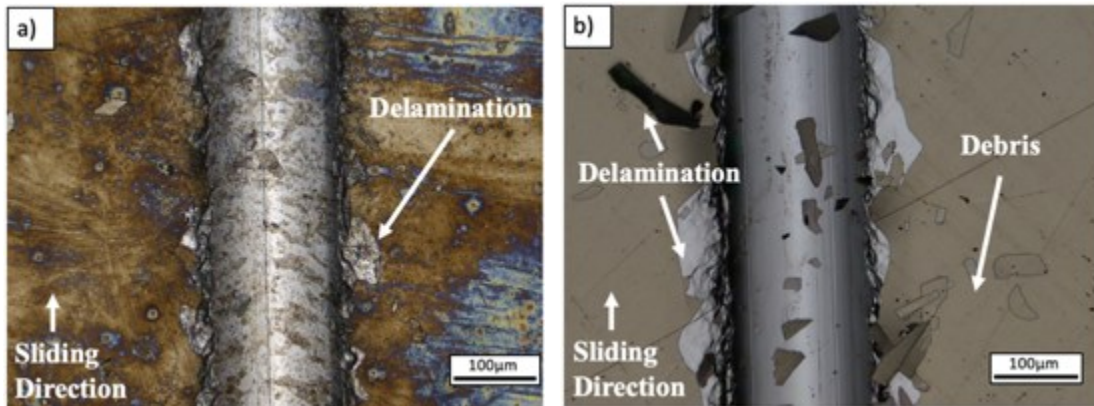
Applied Load (kgf)	0.5	1	2	3	4
Contact radius, a (mm)	0.016	0.020	0.025	0.028	0.031
Mean Contact Pressure, $p_m$	6.42	8.09	10.19	11.67	12.84

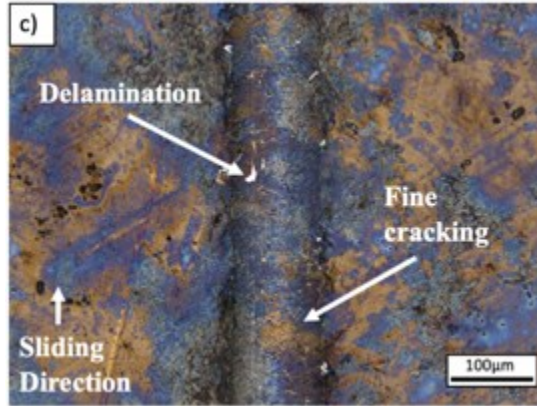
(GPa)					
-------	--	--	--	--	--

It is understood that the depths of deformation during the wear rate test are larger than the 1  $\mu\text{m}$  thickness of the nanolaminate coatings. It should be emphasized here that the failure criteria used in these coatings is their ability to resist fracture and delamination. Although the wear rates calculated from the wear depths include the contribution from the steel substrate, it gives an understanding of the coating and substrate system behavior. Furthermore, cracking of the coatings although is considered failure, if it occurs, it may not contribute to volume loss during wear; therefore, the wear data should be used with this understanding. The purpose here is to simulate the real scratch event.

#### 4.2.1 *Single Pass Fracture Mechanisms*

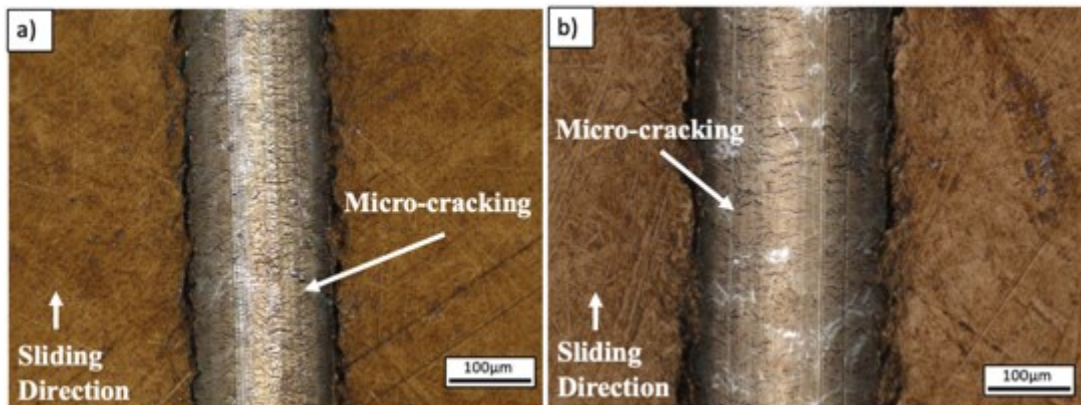
Upon analysis of the scars after a 2kgf load, it is clear that the as-sputtered and 150°C coatings experienced significant delamination inside and along the edges of the scar, seen in Figure 4.18(a) and (b), respectively. Indicating that the scratch energy initiates cracks which cause delamination within these coatings and exposes the substrate. Minor delamination also occurred within the scar of the nanolaminate annealed at 500°C seen in Figure 4.18(c), however, the substrate is not exposed as it was in the as-sputtered and 150°C nanolaminate coatings.

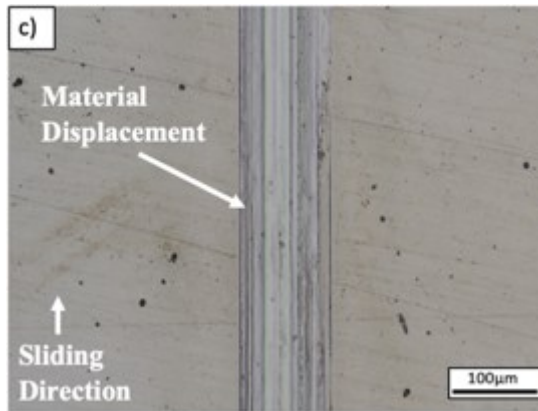




*Figure 4.18 – 2kgf a) as-sputtered b) 150°C and c) 500°C scars*

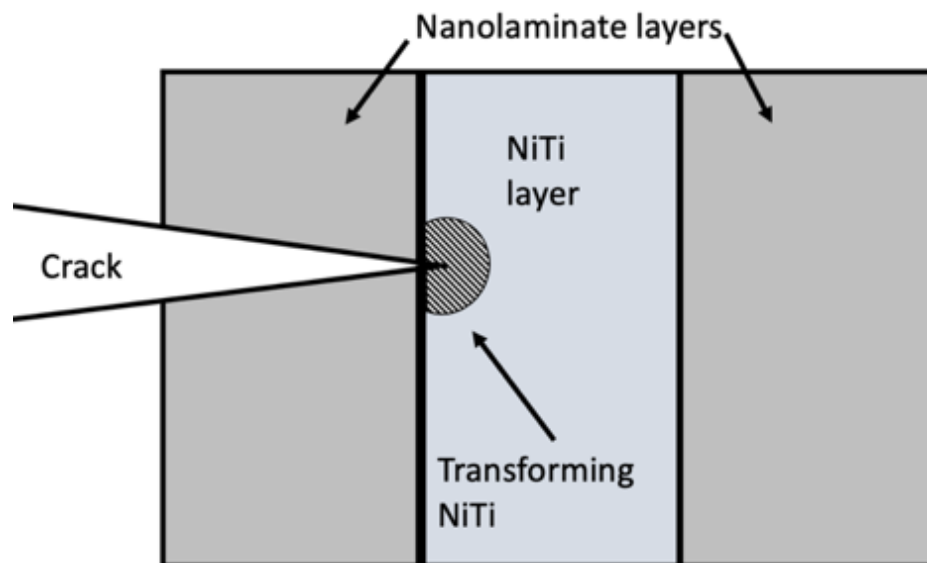
Cracks can also be seen in the scars of the 650°C and 800°C given in Figure 4.19(a) and (b), respectively. The 650°C and 800°C coatings have a network of fine cracks and no delamination. It is believed that energy required for crack initiation and propagation was consumed by the NiTi phase transformation from austenite to detwinned martensite. This transformation also generates compressive strains that prohibit any further propagation of the cracks when they encounter a precipitate, resulting in a network of fine cracks, or micro-cracks, as seen in Figure 4.19(a) and (b). Thus, nanolaminates with NiTi precipitates show evidence of both transformation and micro-crack toughening. On the other hand, the superelastic NiTi coating, Figure 4.19(c), had no micro-cracks and underwent material displacement, indicating a more ductile behavior compared to the nanolaminates.





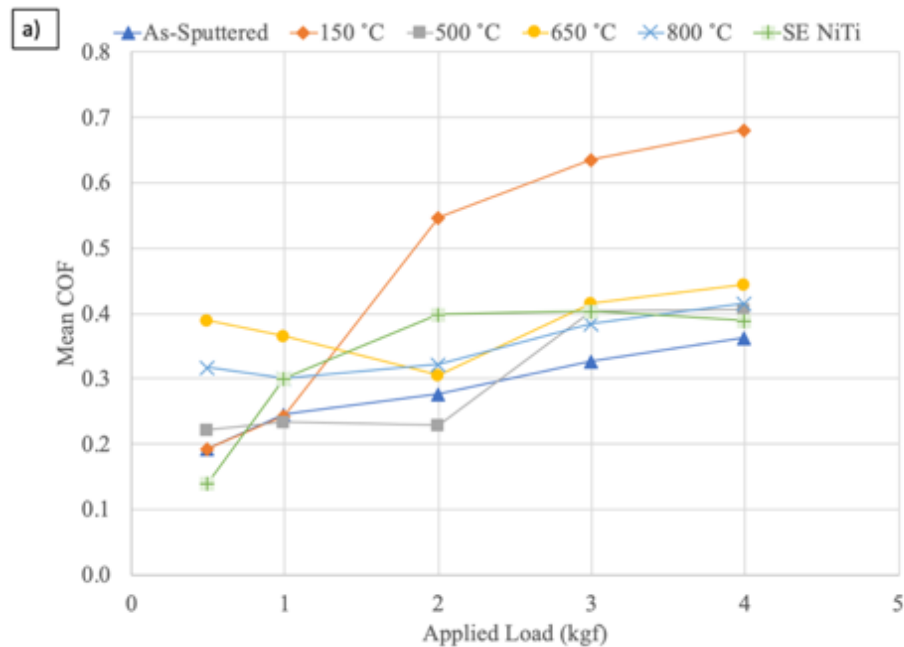
**Figure 4.19 – 2kgf scars of a) 650 °C b) 800 °C and c) superelastic NiTi coating**

A schematic of the NiTi phase transformation within the nanolaminates is illustrated in Figure 4.20. When a crack is growing, it will pass through the nanolaminate structure until it encounters the austenitic NiTi phase. The presence of stress fields around the tip of the crack will be large enough to induce the phase transformation. The crack energy is absorbed by the superelastic NiTi phase as it undergoes a reversible martensitic transformation [90], [91], [117]. During the transformation from austenite to detwinned martensite, there is an increase in volume due to the change in the crystal structure, generating a compressive strain field around the crack tip, which opposes further crack propagation [90]. This results in the dissipation of energy through micro-cracking and the phase transformation, as was seen in the 650°C and 800°C nanolaminate scars.



**Figure 4.20 – Transformation toughening in laminate structures**

The mean COF values, Figure 4.21(a), shows that, in general, increasing the applied load increases the COF. The COF of the coating annealed at 150 °C increases significantly with the applied load. This increase is likely due to the friction between the indenter and substrate as a consequence of significant delamination of the coating. The other coatings narrowly range from about 0.2 to 0.4; showing little difference in COF between nanolaminates. Figure 4.21(b) shows that all coatings, with the exception of the superelastic NiTi coating, had similar volume loss values. It should be noted that single pass COF and wear data only represents the initial stage of the wear process. Therefore, a multiple pass test was conducted to generate data averaged over a larger span of sliding distances and gives a better assessment of coating behavior.



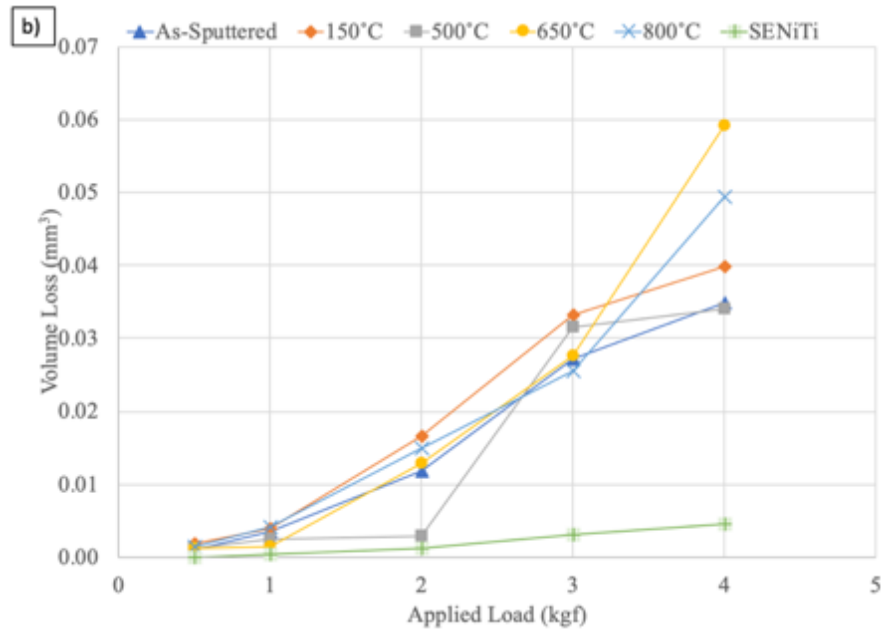


**Figure 4.21 – Constant load a) mean COF values and b) volume loss for nanolaminate coatings and superelastic NiTi monolayer**

#### **4.2.2 Multiple Passes Fracture Mechanisms**

Multiple passes of a 1kgf load were performed to analyze the repeated wear of the coating. After 5 passes of a 1kgf load (totaling a sliding distance of 25 mm), the as-sputtered and 150°C nanolaminates can be seen in Figure 4.22(a) and (b), respectively. These coatings experienced delamination along the edges of the scar, ultimately resulting in the spalling of the coating, leaving the substrate exposed. However, after annealing the coating at 500°C, delamination occurs inside the scar as seen in Figure 4.22(c). The 500°C coating resulted in large and severe cracks within the scar, that extended to the substrate. The significant cracking in the coating annealed at 500°C can be attributed to the high residual stress in the coating as determined by the residual stress analysis (Figure 4.5).

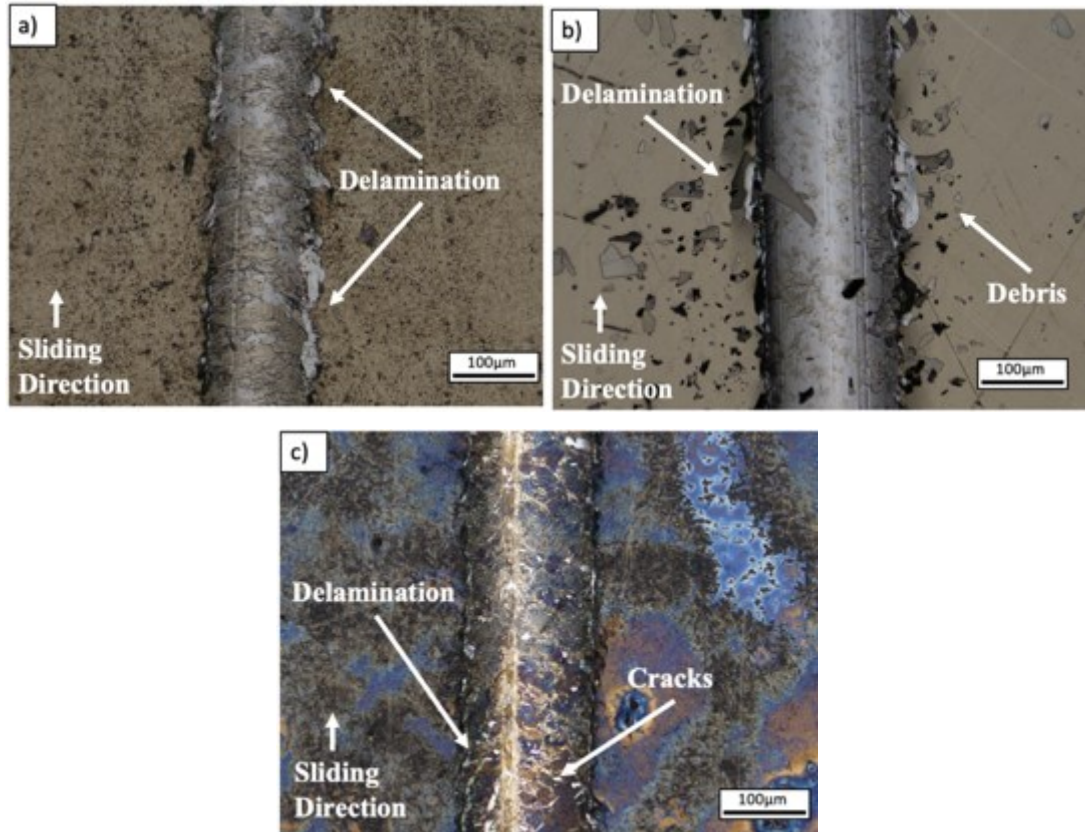


**Figure 4.22 – Sliding distance 25mm a) as-sputtered b) 150°C c) 500°C scars**

The lack of delamination and severe cracking in the 650°C and 800°C nanolaminates, seen in Figure 4.23(a) and (b), may be attributed to the formation of the superelastic NiTi precipitates. The increase in NiTi precipitates volume gives rise to compressive stresses in the vicinity, leading to the closing of propagating fine cracks (micro-cracks). Similar to the single pass test, the energy needed for the initiation and propagation of cracks is consumed by the transformation from austenite to detwinned martensite (transformation toughening). This also occurs in the superelastic NiTi coating, Figure 4.23(c), where there was material displacement and no cracking. Thus, the nanolaminates shows only a network of fine cracks (micro-crack toughening) which was prohibited from further propagation due to the superelastic NiTi monolithic layer.

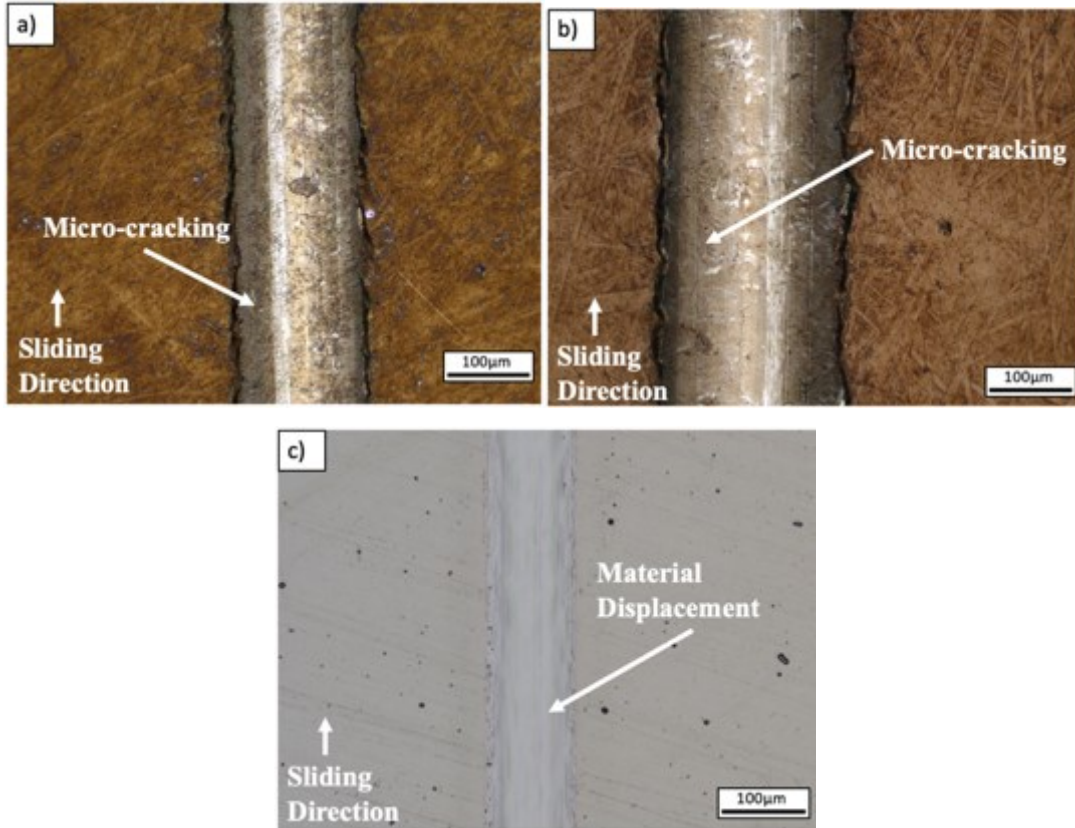


**Figure 4.23 – Sliding distance of 25mm of a) 650 °C b) 800 °C and c) superelastic NiTi coating**

The coatings mean COF values from multiple passes can be seen in Figure 4.24. The mean COF values for the nanolaminates range from 0.1 to 0.3 across all sliding distances. However, the superelastic NiTi had a mean COF value increased from 0.3 to 0.65 after a sliding distance of 25mm. During testing of the NiTi coating, it is believed that there was a transfer layer of superelastic NiTi transferred onto the diamond indenter, which results in an increase in the COF. This phenomenon was studied by Lee *et al.* [118] who found that the rubbing of two materials with the same strength and hardness amplifies the COF values.

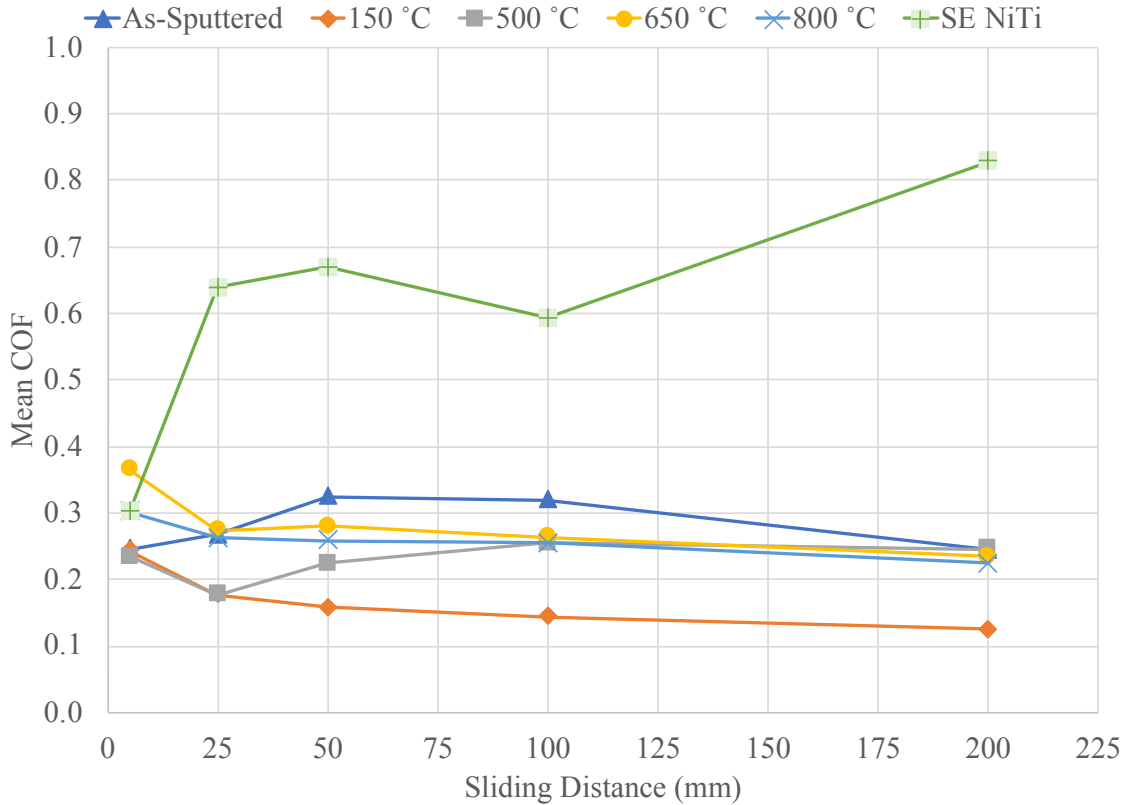


**Figure 4.24 – Multiple passes of a 1kgf load mean COF values for nanolaminate and monolayer superelastic NiTi coatings**

The wear rates of the coatings, determined by the slope of the volume loss against sliding distance, are shown in Figure 4.25. The as-sputtered coating has the largest wear rate. The wear rate of coatings annealed above 500°C exhibit lower wear rates compared to the other nanolaminates. Wear resistance of coatings annealed at 650°C is approximately 7 times higher compared to the as-sputtered coating. The improvement in scratch resistance may be attributed to the formation of superelastic NiTi precipitates during annealing and their toughening effects. This is further validated by the superelastic NiTi coating’s wear rate that is slightly less than the annealed nanolaminates. Indicating that the presence of the superelastic NiTi phase reduces the rate of material removal.

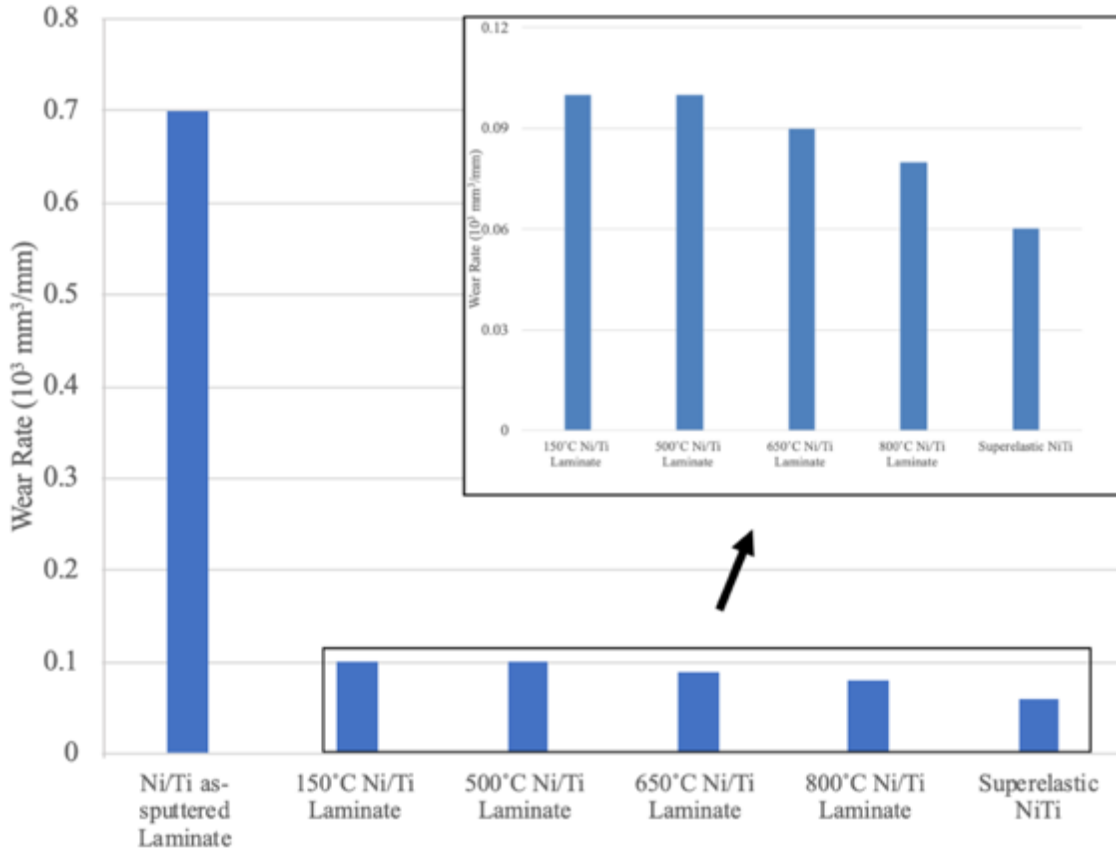


**Figure 4.25 – Wear rates of nanolaminates and superelastic NiTi coating**

Furthermore, the relationship between the wear rate of a material is influenced by both the elastic recovery and the E/H ratios, seen in Figure 4.26. The wear rate drops as the E/H ratio decreases and the elastic recovery ratio increases. The coatings in this study that contain the NiTi phase exhibit a low E/H ratio and a high elastic recovery ratio; validating that the superior wear resistance can be attributed to the presence of the superelastic NiTi phase.

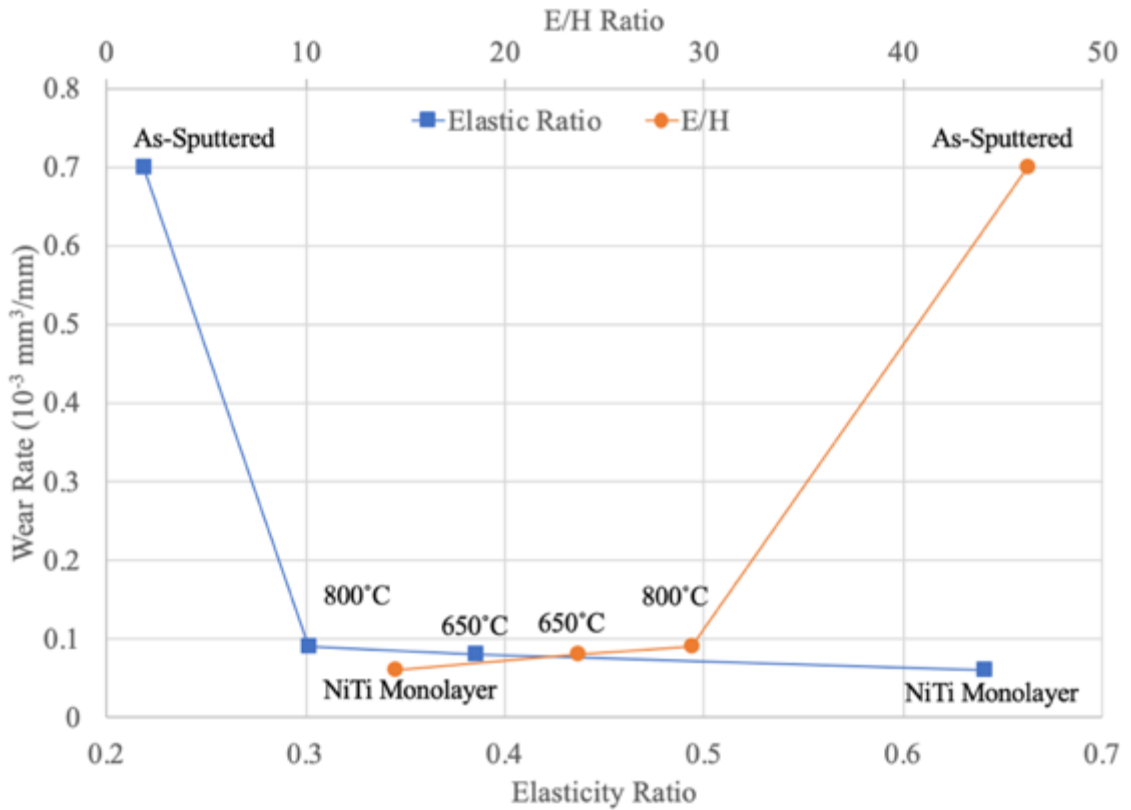


*Figure 4.26 – E/H and elastic recovery ratios influence on wear rates*

### **4.2.3 Increasing Load Scratch Test**

The sliding distance where cracks first began to form was determined from the increasing load scars and is shown in Figure 4.27, noting that the superelastic NiTi coating did not experience cracking. Nanolaminates with the NiTi intermetallic phase (i.e. annealed above 500 °C) required higher loads to initiate cracking compared to the as-sputtered coating. The coatings with NiTi precipitates undergo transformation toughening which hinders cracking requiring a higher load to initiate and propagate cracks.

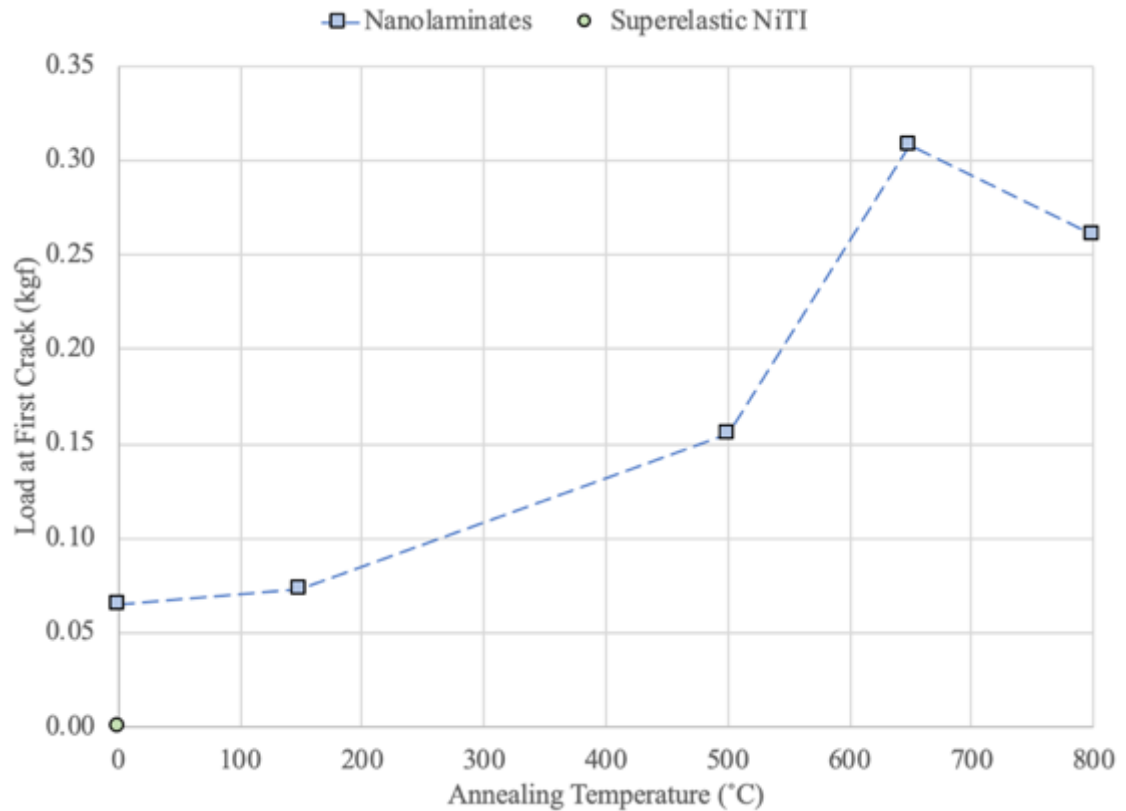


**Figure 4.27 – Load at first crack**

The acoustic emission signal recorded during the increasing load test further confirms that the coating annealed at 650°C exhibits no significant cracking compared to the as-sputtered coating. It is clear from Figure 4.28 that the acoustic emission signal for coatings annealed at 500 °C and 650 °C show low background noise while the as-sputtered coating shows a high peak at an approximate load of 2.5kgf, which is an indication of major crack formation. The AE signal of the superelastic NiTi monolayer shows no spikes, which indicates that severe cracking did not occur.

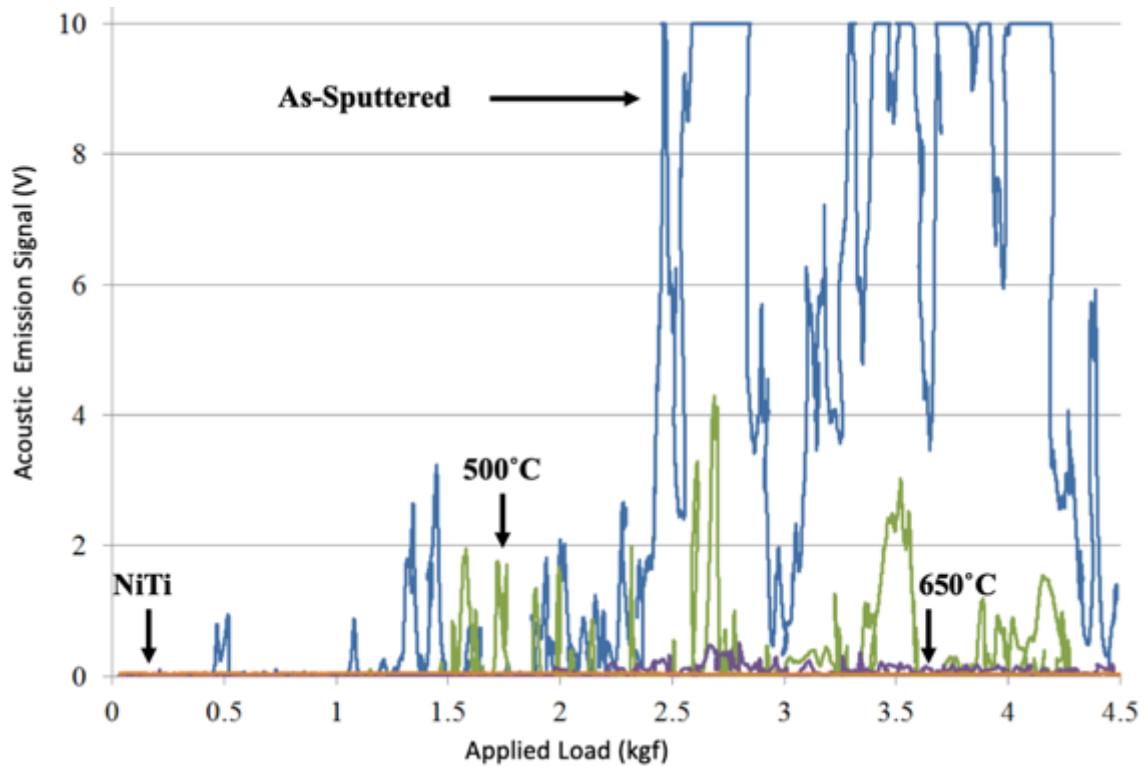


*Figure 4.28 – Acoustic emission signal from the coatings*

An XRD scan was performed after scratch testing to determine if martensitic NiTi peaks were present as evidence of transformation toughening. Figure 4.29 shows the presence of martensitic NiTi peaks in the 650 °C and 800 °C nanolaminates; confirming that the nanolaminates containing NiTi underwent transformation toughening. The martensitic peaks validate that the superior wear resistance of the nanolaminates is due to the formation of superelastic NiTi precipitates.

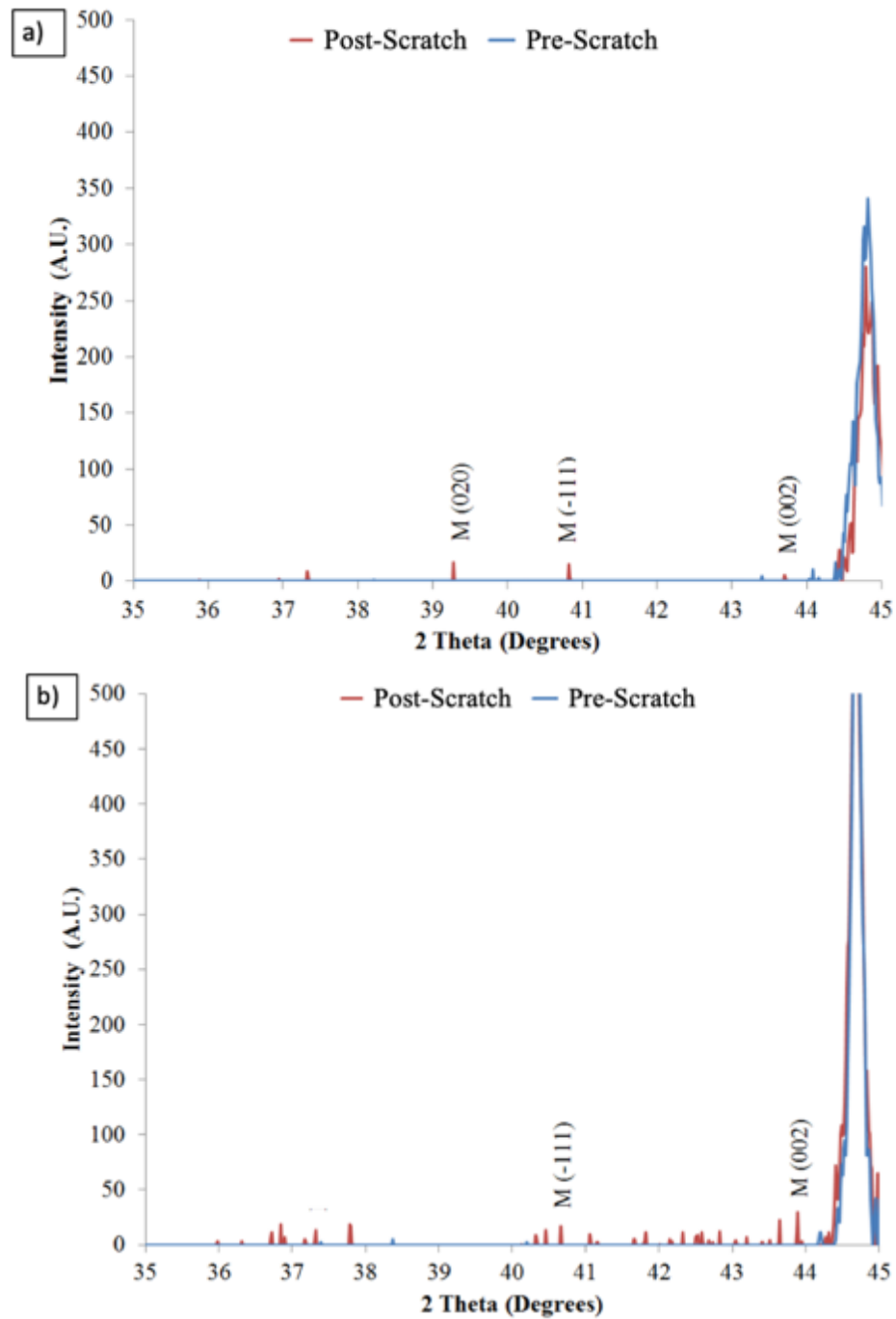
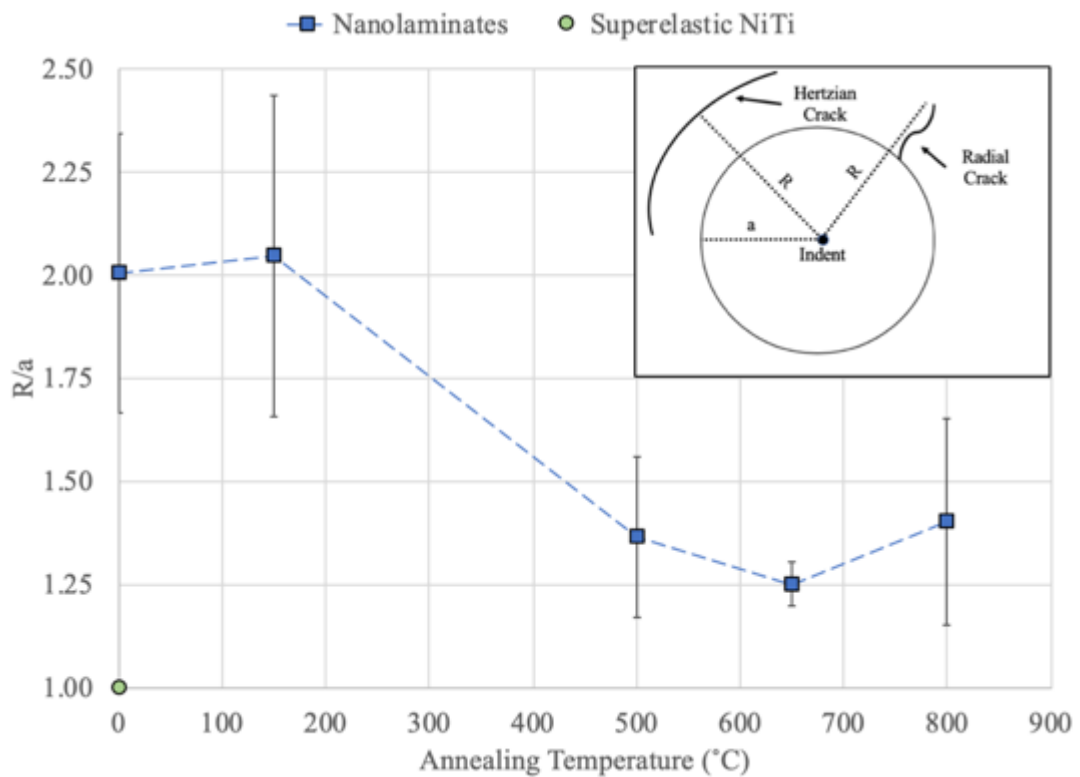


Figure 4.29 – XRD of a) 650 °C and b) 800 °C nanolaminates before and after scratch testing

### 4.3 Hertzian-Type Indentation

To assess the dent resistance of as-sputtered nanolaminate, annealed Ni and Ti nanolaminates, and the monolayer of superelastic NiTi, a series of Hertzian-type

indentation tests were conducted. In order to analyze the extent of cracking during Hertzian indentation, the ratio of the mean crack length ( $R$ ) to indent radius ( $a$ ) is plotted against annealing temperature in Figure 4.30, which also shows how ( $R$ ) and ( $a$ ) are measured. A larger  $R/a$  ratio indicates the propagation of severe cracks. The monolayer of superelastic NiTi had no cracking and the 650°C nanolaminate had the lowest ratio and varied the least of all nanolaminate coatings. The small variation indicates a better dent resistance to all loads applied between 600N and 2500N. This is likely due to the transformation toughening associated with the superelastic NiTi phase.



**Figure 4.30 –  $R/a$  ratios for nanolaminate and monolayered coatings**

Similar to scratch testing, the contact area and mean contact pressure, Equation (2) and Equation (4), were calculated to determine if the load applied was sufficient enough to initiate the reversible martensitic phase transformation of NiTi. Table 4.4 shows that the mean contact pressure is greater than the reported transformation (0.410GPa [2]); therefore, the decrease in crack severity of the 650°C and 800°C nanolaminates may be

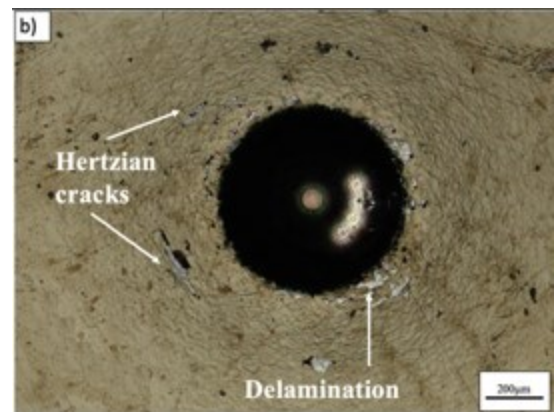
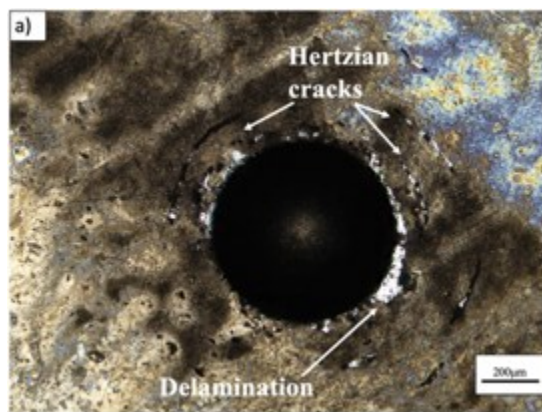
contributed to the superelastic NiTi precipitates undergoing the transformation toughening effect.

**Table 4.4 – Hertzian indentation mean pressure**

Applied Load (N)	600	1000	1500	2000	2500
Contact radius, a (mm)	0.127	0.151	0.173	0.190	0.205
Mean Contact Pressure, $p_m$ (GPa)	11.81	14.00	16.03	17.64	19.00

#### 4.3.1 Fracture Mechanisms Under Hertzian-Type Indentation

It is evident that the as-sputtered and 150 °C nanolaminate coatings exhibit delamination around the indent. It seems that Hertzian ring cracking develops around the indent as a result of the surface tensile stresses, the propagation of ring cracks leads to major delamination occurring in the coatings. Figure 4.31(a) and (b) show ring cracks connecting in a complex network, ultimately causing spalling of the coating. The 500°C coating had a less amount of delamination compared to the as-sputtered and 150°C nanolaminates, Figure 4.31(c), likely due to fine, coherent NiTi precipitates.



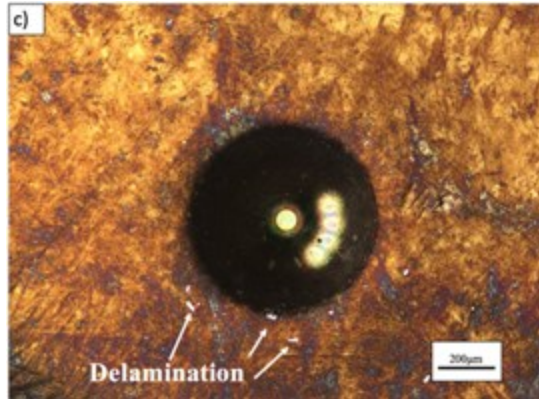


*Figure 4.31 – 1000N indent of a) as-sputtered b) 150°C and c) 500°C annealed nanolaminate coatings*

Delamination is the debonding of adjacent layers in a structure [119]. Pre-existing subsurface cracks form at high residual stress locations and, under applied stresses, will begin to grow. The residual stresses present in a coating will influence the crack growth rates [110], [120]. As these cracks continue to grow, they may intersect and converge, leading to the spalling of the coating. Delamination occurring in a coating can be seen in Figure 4.32.

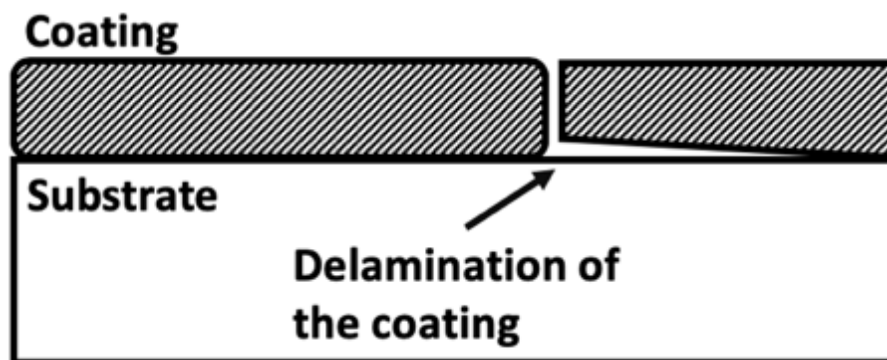


*Figure 4.32 – Schematic of delamination occurring in the coating*

Further evidence of the enhanced toughening of NiTi precipitates is given in Figure 4.33(a) and (b); as the nanolaminates annealed at 650°C and 800°C show a major enhancement in toughening and dent fracture resistance. The formation of the superelastic NiTi clearly improves the toughness of the coatings as a result of the transformation toughening mechanisms and superelastic effects. The lack of spalling of

the nanolaminate coatings annealed above 500°C allows them to be compared to the monolayer of superelastic NiTi (Figure 4.33(c)).

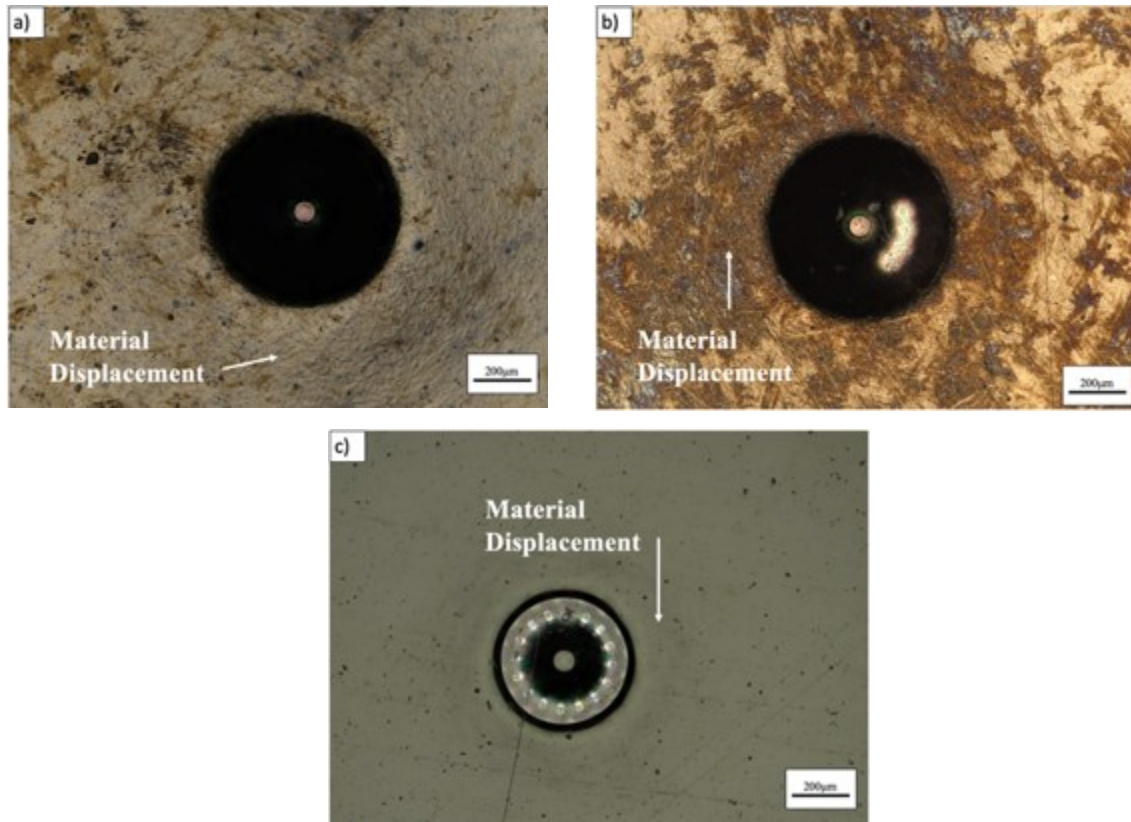


*Figure 4.33 – 1000N indent of a) 650 °C b) 800°C annealed nanolaminate coatings and c) superelastic monolayer of superelastic NiTi coating*

### **4.3.2 Cracking Events**

The AE sensor was used to identify if cracking events occurred during loading. The load-displacement curves, Figure 4.34, show that severe cracking occurred in coatings annealed at lower temperatures. The as-sputtered coating, seen in Figure 4.34(a), had a large spike at an approximate load of 300N indicating the initiation and propagation of severe cracks. While the 650°C and 800°C nanolaminates, and the superelastic NiTi monolayer had no spikes in the AE signal during testing. It should be noted that the depth at which cracking signals are detected is larger than the coating thickness. Since the low

carbon steel substrate is much softer than the coatings it deforms before cracking occurs in the coating.

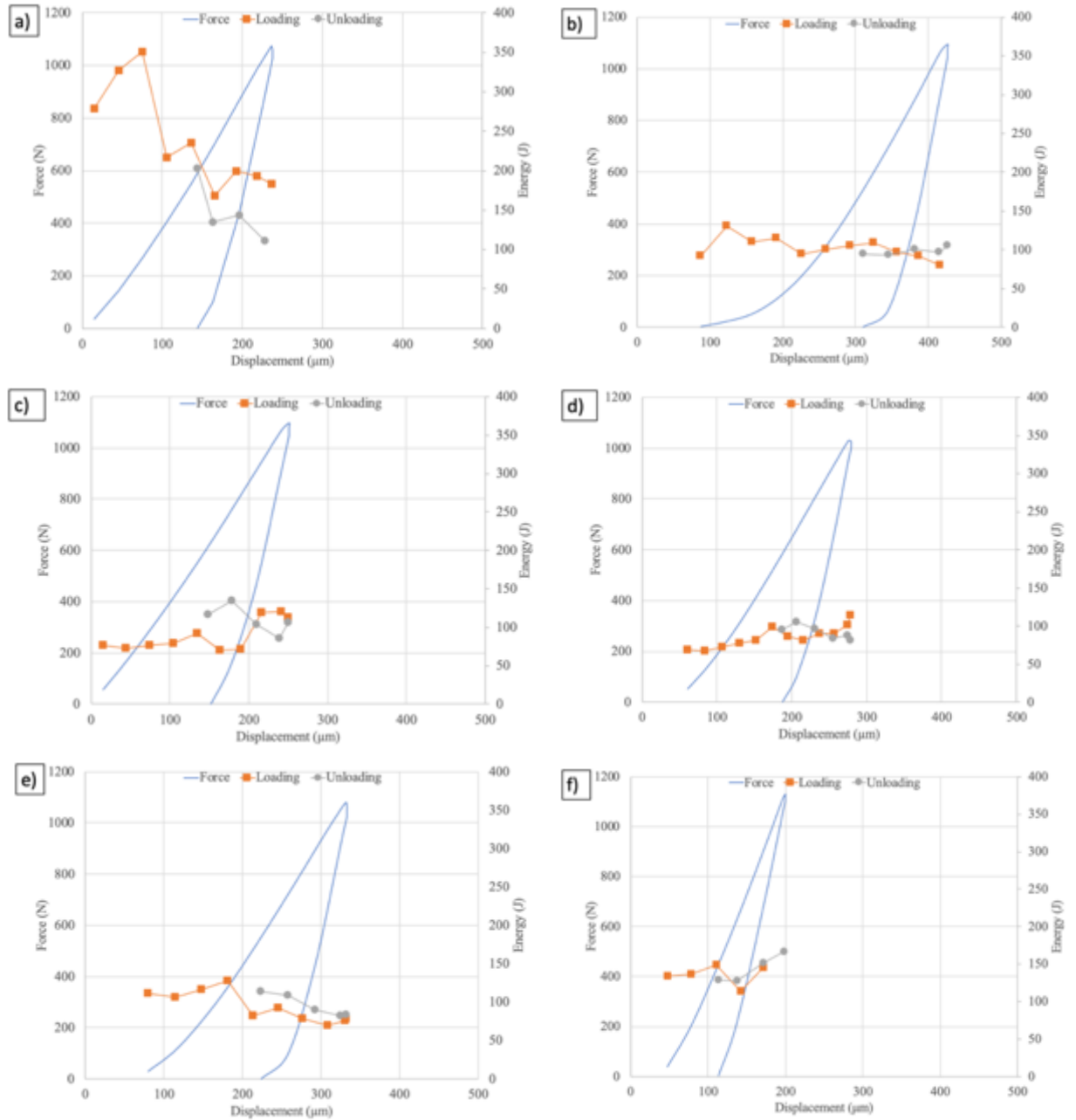


**Figure 4.34 – 1000N load-displacement curves for a) as-sputtered b) 150°C c) 500°C d) 650°C e) 800°C nanolaminate coating and f) monolayered superelastic NiTi coating**

#### 4.4 Single Particle Impact Erosion

The mean contact pressure exerted by the impacting particles was calculated to ensure the force was large enough to initiate the NiTi phase transformation. To calculate the applied force of the impacting particle, the kinetic energy can be equated to the work done by the particle, as seen in Equation (17). This equation works under the assumption that the friction and drag effects of the impacting particle are negligible.

$$Pl = \frac{1}{2} m_p v_p^2 \sin \phi \quad (17)$$

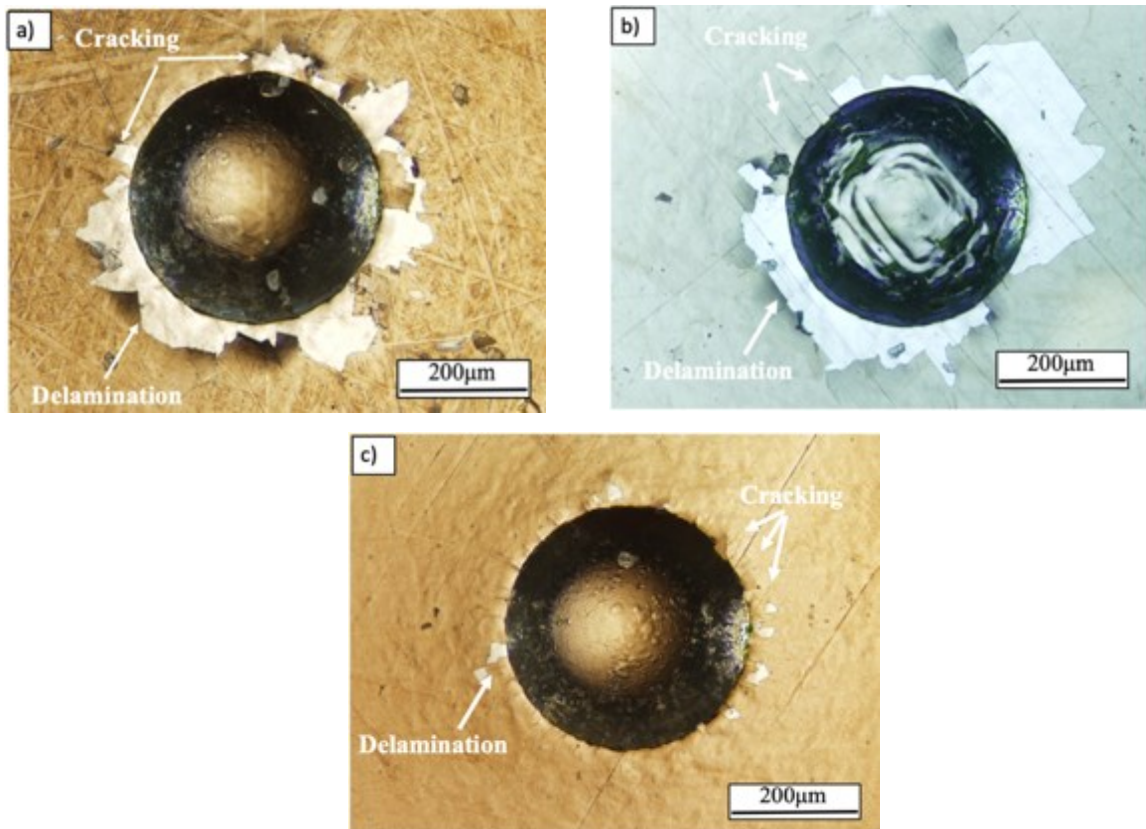
Where P is the applied load, l is the distance the particle travels,  $m_p$  is the mass of the particle,  $v_p$  is the velocity of the impacting particle, and  $\phi$  is the incident angle. From this, the mean contact pressure can be calculated, Equation (2) and Equation (4), to determine the mean contact pressure exerted at each angle, as seen in Table 4.5. At a 30° angle, the mean contact pressure is below that of the NiTi transformation initiation stress of 0.410GPa [2]. However, given the uncertainty in the exact composition of the NiTi precipitates, hence, uncertainty in the exact transition stress, as well as, uncertainty in the exact incident angle, it is reasonable to assume that even at low impact angle some martensitic transformation can take place, given the small difference between the contact pressure and the reported transformation stress.

*Table 4.5 – Single particle impact mean contact pressure*

Impact angle (°)	30	45	60	90
Applied Load (N)	0.020	0.029	0.035	0.040
Contact radius, a (mm)	0.004	0.005	0.005	0.005
Mean Contact Pressure, $p_m$ (GPa)	0.381	0.428	0.458	0.480

#### 4.4.1 High-Angle Fracture Mechanisms

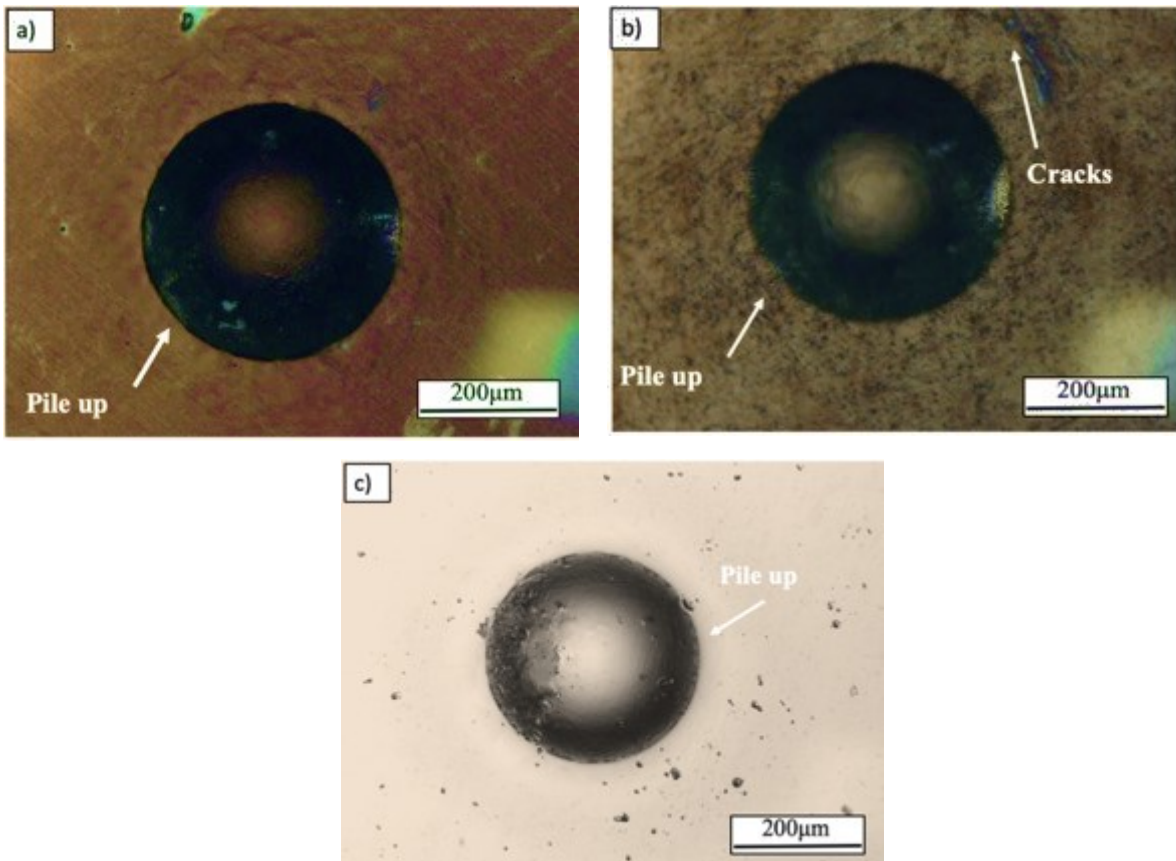
High-angle impact of the as-sputtered, 150°C, and 500°C nanolaminate coatings can be seen in Figure 4.35(a), (b), and (c), respectively. Upon impact, cracks were initiated and then propagated downwards into the coating towards the substrate, resulting in the delamination and spalling of the coating. The 500°C nanolaminate coating shows that radial cracking occurred as well as significantly less delamination, comparatively. This is likely due to the presence of small superelastic NiTi precipitates.



**Figure 4.35 – Single particle 90-degree impact a) as-sputtered b) 150°C and c) 500°C nanolaminate coating**

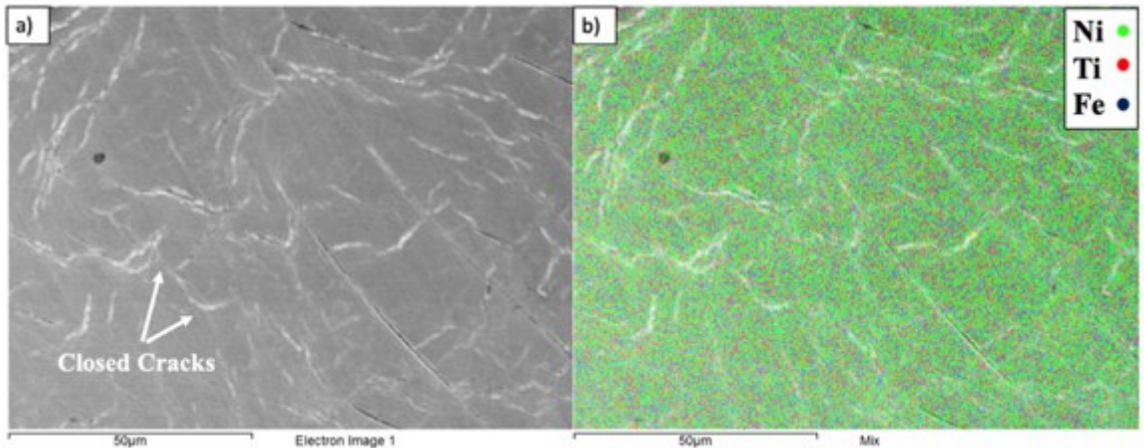
The nanolaminates that contain NiTi and the monolayer of superelastic NiTi results in minimum surface damage. The 650°C and 800°C nanolaminates, Figure 4.36(a) and (b), show less delamination and only a few fine cracks, due to the superelasticity effect of NiTi precipitates. Upon impact, the energy is absorbed by the coating, which initiates the

phase transformation from austenite to detwinned martensite. Once the applied load of the impacting particle is removed, the reverse phase transformation occurs and some of the elastic strains are recovered. Comparing the nanolaminates to the monolayer of superelastic NiTi, Figure 4.36(c), reveals that it is likely the nanolaminates experienced transformation toughening.



**Figure 4.36 – Single particle 90-degree impact a) 650°C b) 800°C and c) monolayer of NiTi coating**

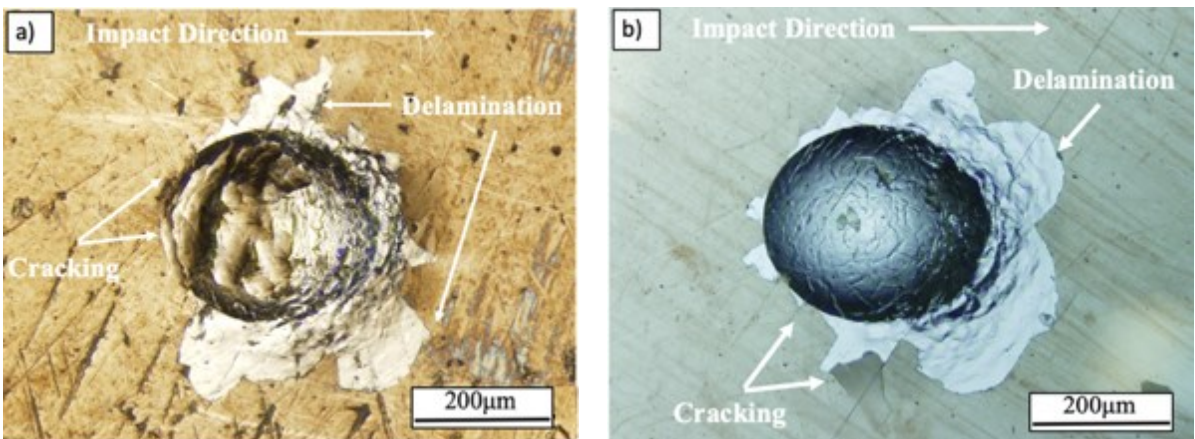
Although the 650°C nanolaminate impact experienced cracking within the impact site, as seen in Figure 4.37(a), the phase transformation generates compressive strains that prohibit any further propagation of the cracks. This minimizes the extent of surface damage done within the coating. This is evidence that the phase transformation occurred in the coating upon impact. Figure 4.37(b) is an EDS map that shows that the closed cracks do not expose the substrate.

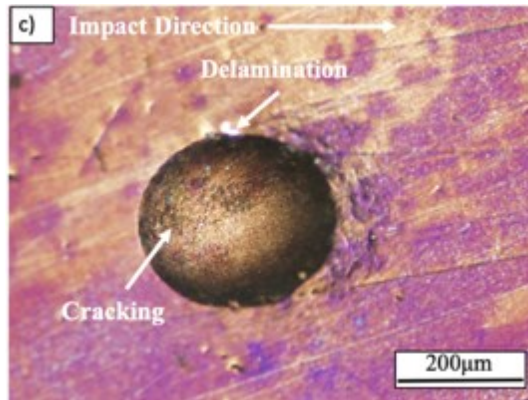


**Figure 4.37 – Impact site of 650 °C nanolaminate a) SEM and b) EDS map of 90° impact**

#### 4.4.2 Low-Angle Fracture Mechanisms

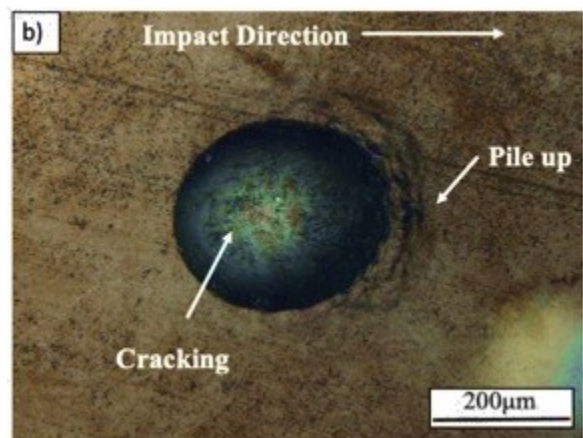
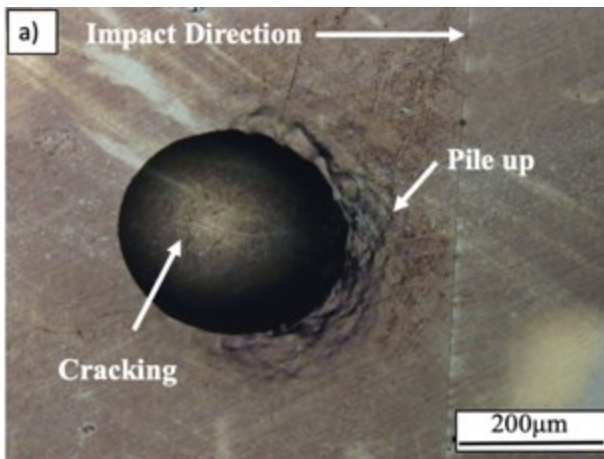
Low-angle erosion testing resulted in elliptical impact sites, as seen in both Figure 4.38 and Figure 4.39. The as-sputtered, 150°C, and 500°C nanolaminate coatings undergo spalling and delamination upon impact, as seen in Figure 4.38(a), (b), and (c), respectively. Similar to the high-angle impacts, cracks were initiated on the surface of the coating and then propagated downwards to result in the spalling of the coating from beneath and around the impact area.





**Figure 4.38 – Single particle 30-degree impact a) as-sputtered b) 150°C and c) 500°C nanolaminate coating**

The coatings that contain NiTi show few fine cracks as seen in Figure 4.39. At the lower angles, the impacts of the 650°C and 800°C nanolaminates show few cracks within the indent and no delamination. As impact occurs, the kinetic energy is transferred to the coating and dissipated through both the initiation and propagation of fine cracks (micro-cracks). When the cracks encounter the NiTi phase, the cracking energy is consumed by the phase transformation and further cracking is prohibited due to the compressive strain fields caused by the formation of the martensitic NiTi phase. The erosion resistance of these monolithic coatings is enhanced due to the NiTi precipitates ability to dissipate cracking energy through the phase transformation effect.



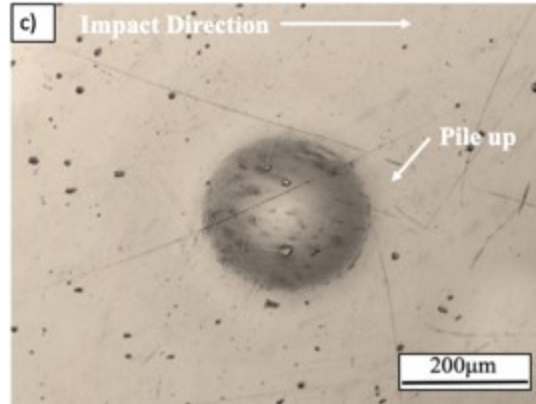


*Figure 4.39 – Single particle 30-degree impact a) 650°C b) 800°C and c) monolayer of NiTi coating*

#### **4.4.3 Erosion Mechanisms**

Upon impact of the particle on the 150°C annealed coating, cracks are initiated and propagated resulting in delamination, as seen in Figure 4.40. Upon impact, the residual stresses within the coating accelerated the propagation of cracks causing the removal of the coating around the impact site. The confocal and depth profiles show delamination of the coating from the substrate, indicating poor erosion resistance. The confocal images and profiles for both low and high angles show pile-up on the edges of the indent. It is likely that the steel substrate is squeezed to the edges of the indent causing the pile-up and lifting of the coating. It is evident that the low angle impact causes pile-up on the side opposite to the location of initial impact. As a consequence of the pile-up, lifting and delamination of the coating has occurred only on the side opposite to the initial impact. However, the normal impact shows pile-up and delamination of the coating all around the indent.

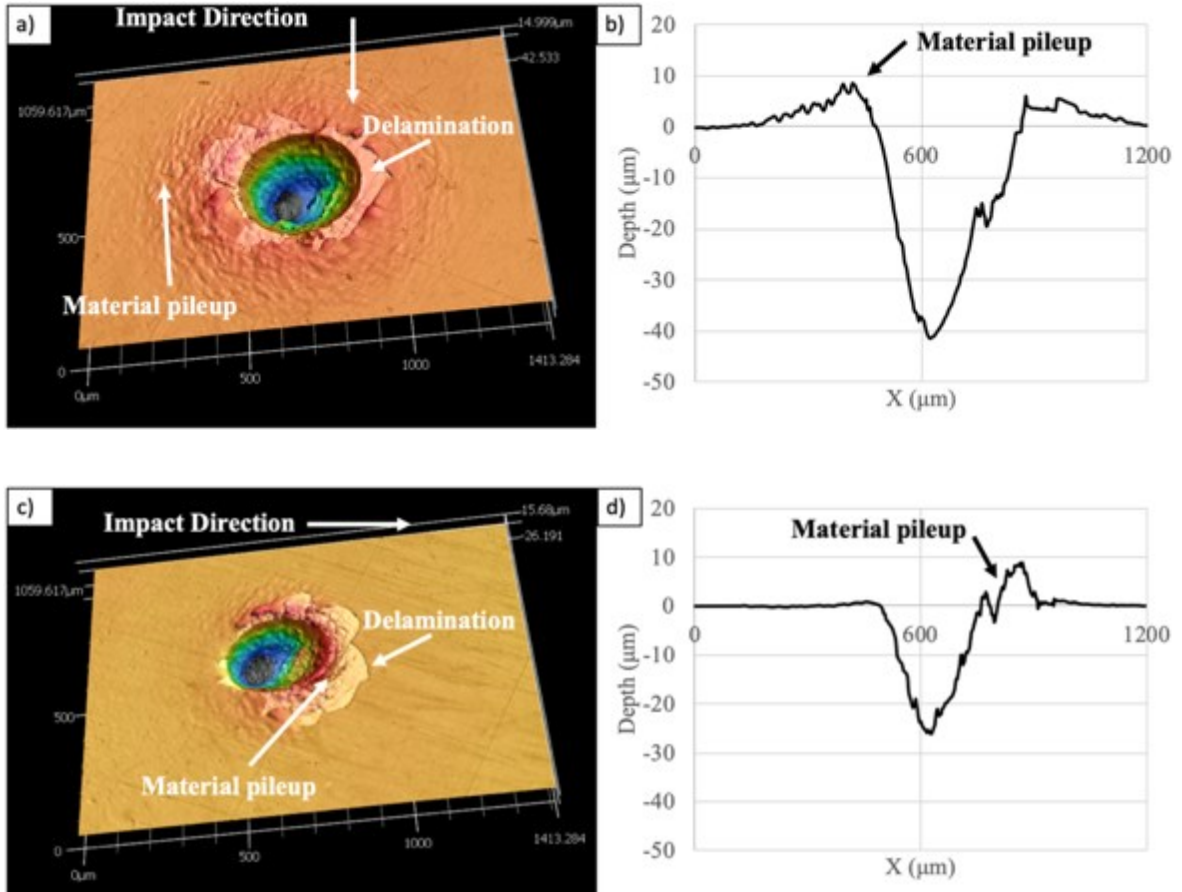


**Figure 4.40 – Nanolaminate annealed at 150°C impact profiles at 90° a) confocal image b) depth profile and 30° impacts c) confocal image and d) depth profile**

The impacting particle was examined for evidence of adhesive wear after testing of the as-sputtered nanolaminate. The WC ball used for impacting, Figure 4.41, shows evidence of adhesive wear. As the hardness of the WC ball is much larger than that of the as-sputtered coating, it is believed that upon impact of the particles, the as-sputtered nanolaminate coating adhered to the surface of the particle.

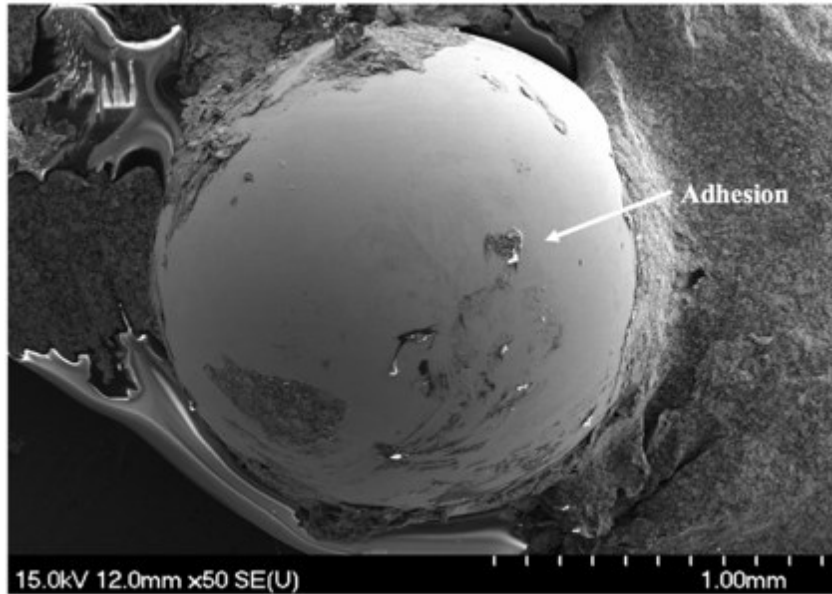


*Figure 4.41 – WC ball used to impact as-sputtered coating*

The transformation toughening ability of the monolayer of superelastic NiTi resulted in no material removal, at both high and low impact angles, as seen in Figure 4.42. Superelastic NiTi has the ability to impede erosive wear due to its superelastic effect [121]; resulting in the kinetic energy being totally dissipated through the reversible phase transformation. The impact sites show that the material was displaced in the direction of impact, whereas the 90° evenly displaces the material around the indent. Upon impact, the particle pushes the material in one direction, forming a work-hardened lip [122]; as seen in the depth profile of the 30° impact.

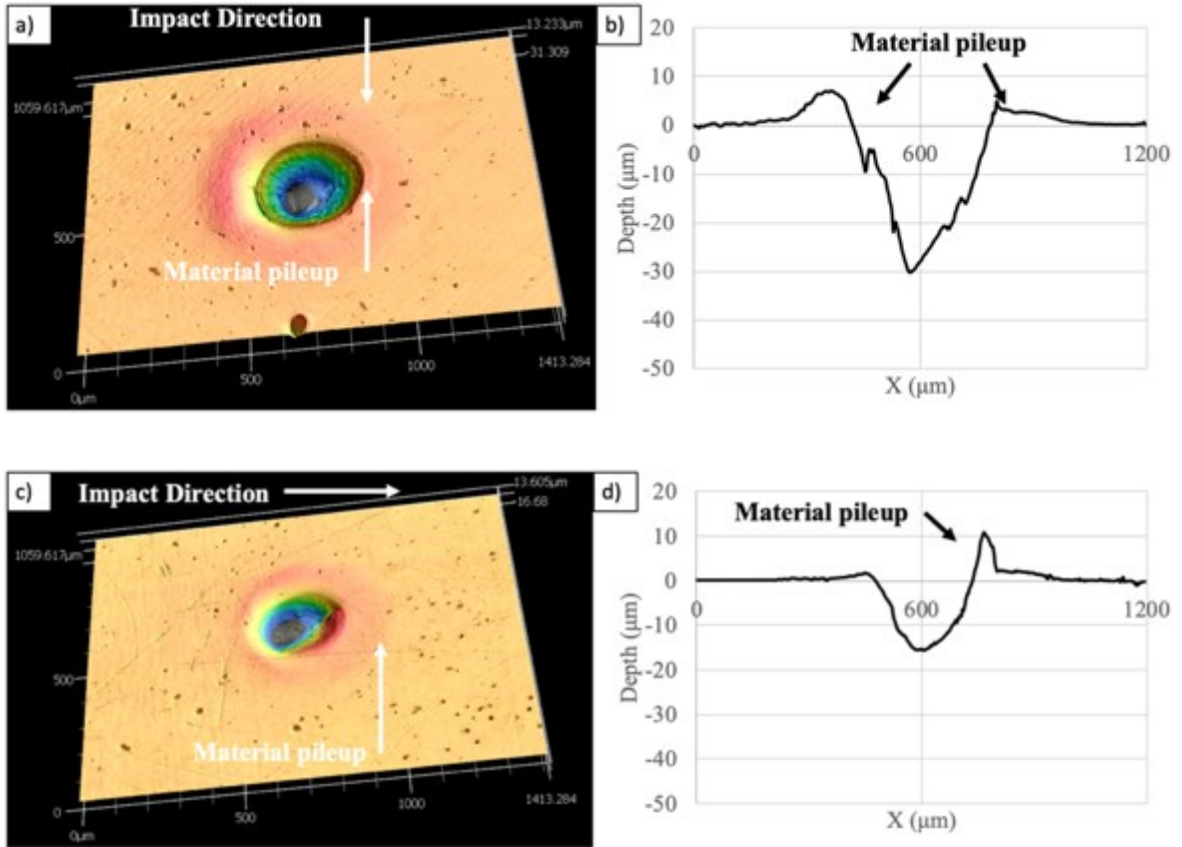


**Figure 4.42 – Superelastic NiTi monolayer coating impact profiles at 90° a) confocal image b) depth profile and 30° impacts c) confocal image and d) depth profile**

The 650 °C nanolaminate experienced transformation toughening at high and low impact angles, as seen in Figure 4.43. No visible cracks were detected in the confocal image. The transfer of kinetic energy of the particle is dissipated mainly through the martensitic transformation. Any fine cracks that may form are prevented from any significant propagation by the NiTi precipitate. Here, the crack energy is absorbed by the NiTi precipitates as they transform from austenite to martensite, during transformation, the NiTi precipitates expand and create a compressive stress field in their vicinity which assists in closing cracks. The material pile-up is comparable to the superelastic NiTi coating.

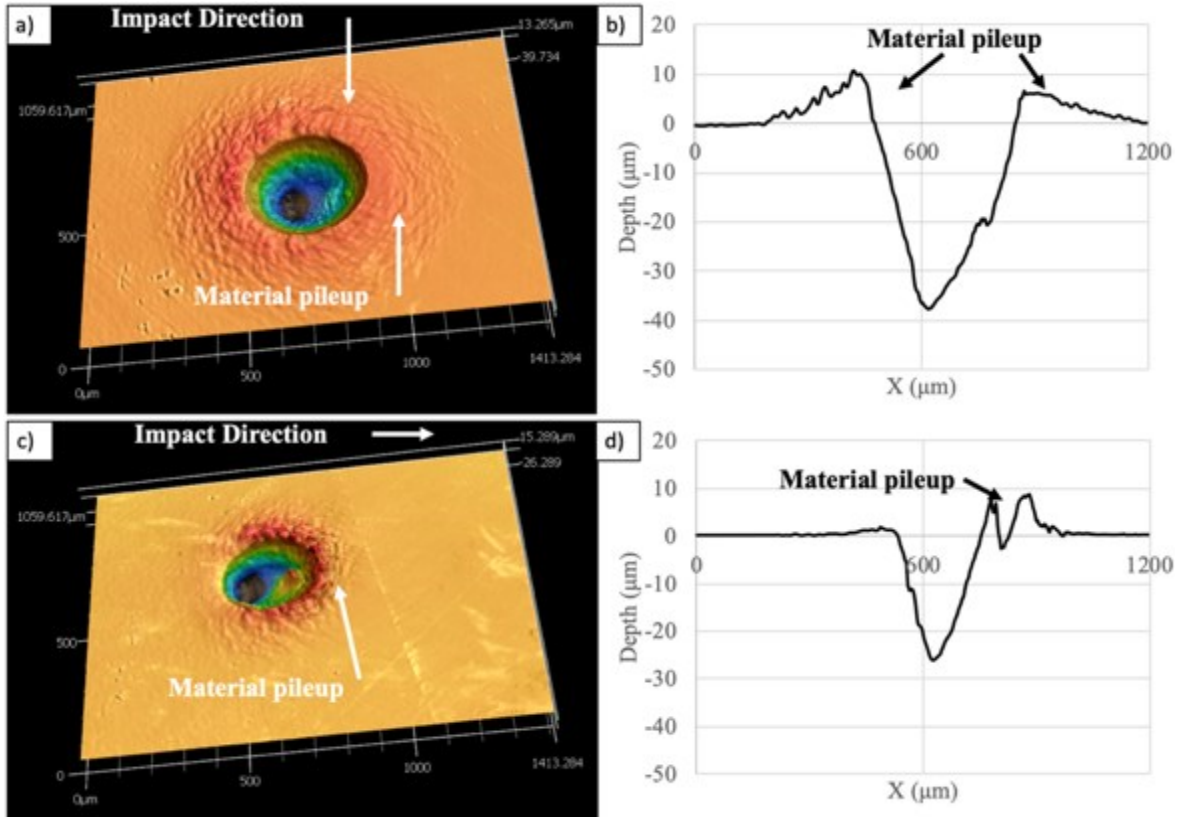


**Figure 4.43 – Nanolaminate annealed at 650°C impact profiles at 90° a) confocal image b) depth profile and 30° impacts c) confocal image and d) depth profile**

Overall, the volume loss during single particle erosion increases with impact angle as seen in Figure 4.44. The nanolaminates all reported similar volume losses, whereas, the NiTi coating reported less volume loss at each angle. Despite this, all coatings tested had the highest volume loss at 90°, which is expected as the impact energy increases with impact angles. For ductile materials, erosion is typically highest at low angles as a result of the cutting mechanism. However, the cutting mechanism is induced as a result of sharp impact particles, which is not the case in this study. Therefore, the increasing erosion with impact angle trend, as seen in Figure 4.44, is expected when spherical particles are used.

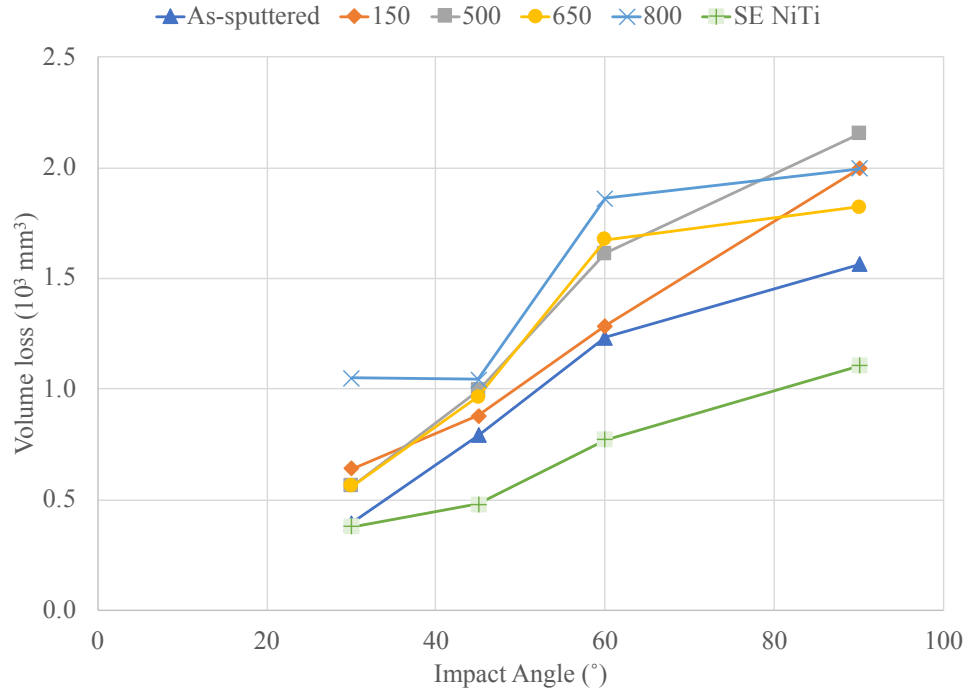


**Figure 4.44 – Volume loss at different impact angles for all coatings**

#### 4.5 Dent Resistance Comparative Analysis

The 650°C nanolaminate demonstrated superior wear resistance under sliding, denting, and eroding conditions in this study. Compared to the superelastic NiTi monolayer, the 650°C nanolaminate exhibited higher hardness values, yet, similar elastic recovery and E/H ratios. To further explore the possibility that the 650°C nanolaminate could be a suitable replacement to other wear resistant coatings, a comparative analysis of dent resistance was conducted comparing this nanolaminate to a 40µm thick hard chromium coating and 62µm thick electroless Ni-P coating.

The hard chromium coating was fabricated through an electroplating coating process, these coatings are primarily used in aerospace and automotive industries. The appeal of these coatings in wear-resistant applications is their low COF, high melting point, high hardness, and resistance to corrosion and wear [123]. Ni-P coatings exhibit resistance to corrosion and wear and the electroless coating process provides superb adhesion and is

able to coat a variety of shape and sizes [124]. Ni-P coatings are predominantly found in oil and gas pipelines, food industries, and aerospace.

A 1500N load indentation site on a Ni-P, hard chromium, and 650°C annealed nanolaminate can be seen in Figure 4.45(a), (b), and (c), respectively. The hard chromium and Ni-P coatings have several radial cracks extending from the edge of the indent. Upon contact of the spherical indenter, cracks were initiated at the edges of the contact area and then continued to grow outwards, which indicates brittle behavior. The cracks may extend into the coating towards the substrate, which will expose the substrate.

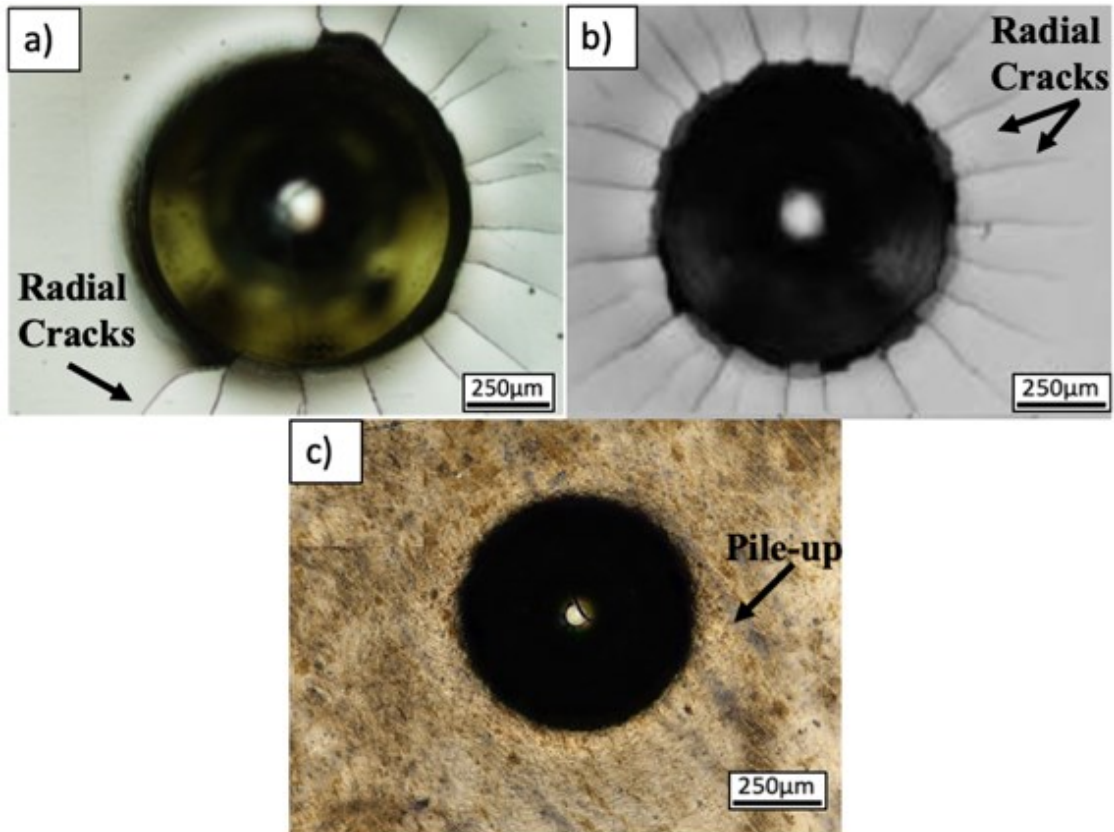


*Figure 4.45 – 1500N indents of a) Ni-P [124] b) hard chromium [123] and c) 650°C annealed nanolaminate coatings*

In contrast, the nanolaminate coating annealed at 650°C had no visible cracks and material pile-up around the indent. Upon contact, the energy is absorbed and dissipated through the transformation toughening effects of the superelastic NiTi phase. The

material pile-up around the edges indicates ductile behavior, which is not seen in the chromium or nickel coatings. Concluding that the Ni-Ti nanolaminate annealed at 650°C has better dent resistance compared to the Ni-P and chromium coatings. Thus, proving that the 650°C nanolaminate could be a potential replacement for these coatings in industrial applications.

## 5.0 Conclusion

### 5.1 Summary

In summary, NiTi was successfully produced within the coating through the annealing of sputter deposited Ni and Ti layers. Characterization shows that the hardness and elastic moduli of the nanolaminate coatings were greater than those of the monolayered superelastic NiTi coating. The higher hardness values can be attributed through the laminate structure of the coating. Furthermore, the presence of superelastic NiTi phase induces transformation toughening, which enhances crack resistance significantly. The superelastic NiTi monolayer and 650°C nanolaminate exhibited comparable E/H and elastic recovery ratios compared to the other nanolaminates, yet, the 650°C nanolaminate had a higher hardness value. Concluding that out of all the coatings tested, the 650°C nanolaminate produced optimal results, which are highlighted below.

- Successfully formed the austenitic NiTi intermetallic phase and exhibited low residual stress values;
- Comparable E/H and elastic recovery ratios to the monolayer of superelastic NiTi but exhibits a higher hardness due to its nanolaminate structure;
- Exhibited highest wear resistance compared to all other nanolaminate coatings;
- Showed greater dent resistance when compared to chromium and Ni-P coatings under a 1500N load.

This study suggests that subjecting a Ni-Ti nanolaminate coating to a heat treatment process is a potential fabrication method of a wear-resistant NiTi surface coating. This alternative manufacturing method of producing superelastic NiTi requires the minimum amount of machining post-coating. These coatings have the potential to be incorporated into industrial applications in numerous sectors.

## 5.2 List of Publications From This Work

- **Fabrication, characterization, and evaluation of wear behavior of monolithic NiTi coatings** – accepted at Tribology Transactions (July 2019).
- **Investigation into the wear behavior of NiTi nanolaminates and monolayer of superelastic NiTi coating** – under review at Journal of Materials Engineering and Performance.
- **Single particle erosion behavior of NiTi nanolaminates and monolayer of superelastic NiTi coatings** – Undergoing editing process.

## 5.3 Future Research

The results of this study prove that superelastic NiTi can be developed within a surface coating; validating that its presence increases the wear resistance of the coating. To further this research, a systematic study is needed to understand and control the formation and growth of the NiTi intermetallic layer, to optimize the thickness for greater wear resistance. Once optimal NiTi formation is achieved, further research is needed on the topics outlined below.

- The temperature range ( $A_s$ ,  $A_f$ ,  $M_s$ ,  $M_f$ ) at which the coating can be used should be exploited. If NiTi is not in its austenitic phase then the superelasticity effect is non-existent.
- An in-depth and comprehensive study of the corrosion resistance of the NiTi monolayer and nanolaminates coatings is needed to explore if this fabrication method could be suitable for components in corrosive environments.
- Further research may be needed into alternative coating methods. Sputtering is the most common for thin films, however, it is a low production and timely process. Other coating methods, such as electroless plating of Ni-P onto Ti, should be exploited.

## 6.0 References

- [1] J. R. Davis, Ed., “Introduction to surface engineering for corrosion and wear resistance,” in *Surface Engineering for Corrosion and Wear Resistance*, Materials Park, OH: ASM International, 2001, pp. 1–10.
- [2] C. Zhang and Z. N. Farhat, “Sliding wear of superelastic TiNi alloy,” *Wear*, vol. 267, no. 1–4, pp. 394–400, Jun. 2009.
- [3] S. Momeni and W. Tillmann, “Investigation of the self-healing sliding wear characteristics of NiTi-based PVD coatings on tool steel,” *Wear*, vol. 368–369, pp. 53–59, Dec. 2016.
- [4] W. Ni, Y.-T. Cheng, M. Lukitsch, A. M. Weiner, L. C. Lev, and D. S. Grummon, “Novel layered tribological coatings using a superelastic NiTi interlayer,” *Wear*, vol. 259, no. 7–12, pp. 842–848, Jul. 2005.
- [5] A. Cavaleiro and J. T. M. De Hosson, Eds., *Nanostructured Coatings*. New York, NY: Springer New York, 2006.
- [6] E. W. Brooman, “Corrosion performance off environmentally acceptable alternatives to cadmium and chromium coatings: Chromium—Part I,” *Met. Finish.*, vol. 98, no. 7, pp. 38–43, Jul. 2000.
- [7] P. K. Kumar and D. C. Lagoudas, “Introduction to Shape Memory Alloys,” in *Shape Memory Alloys*, Boston, MA: Springer US, 2013, pp. 1–51.
- [8] D. Y. Li, “Development of novel tribo composites with TiNi shape memory alloy matrix,” *Wear*, vol. 255, no. 1–6, pp. 617–628, Aug. 2003.
- [9] K. Mehrabi, H. Bahmanpour, A. Shokuhfar, and A. Kneissl, “Influence of chemical composition and manufacturing conditions on properties of NiTi shape memory alloys,” *Mater. Sci. Eng. A*, vol. 481–482, pp. 693–696, May 2008.
- [10] S. Miyazaki, Y. Q. Fu, and W. Huang, “Overview of sputter-deposited TiNi based thin films,” in *Thin Film Shape Memory Alloys: Fundamentals and Device Applications*, New York: Cambridge University Press, 2009, pp. 1–72.
- [11] P. J. Blau and J. R. Davis, *ASM Handbook Nonferrous Alloys and Special-Purpose Materials*. Materials Park, OH: ASM International, 2000.
- [12] H. Okamoto, “Supplemental Literature Review of Binary Phase Diagrams: Au-Ce,

- B-Pr, Bi-Gd, Bi-Ho, Cd-Sr, Ga-Ti, Gd-Pb, Gd-Ti, Mg-Mn, Mn-Nd, Nd-Ni, and Ni-Ti,” *J. Phase Equilibria Diffus.*, vol. 36, no. 4, pp. 390–401, Aug. 2015.
- [13] A. Taylor and R. W. Floyd, “Precision measurements of lattice parameters of non-cubic crystals,” *Acta Crystallogr.*, vol. 3, no. 4, pp. 285–289, Jul. 1950.
- [14] K. Otsuka and X. Ren, “Physical metallurgy of Ti–Ni-based shape memory alloys,” *Prog. Mater. Sci.*, vol. 50, no. 5, pp. 511–678, Jul. 2005.
- [15] J. P. Oliveira, R. M. Miranda, and F. M. Braz Fernandes, “Welding and Joining of NiTi Shape Memory Alloys: A Review,” *Prog. Mater. Sci.*, vol. 88, pp. 412–466, Jul. 2017.
- [16] G. . Sandrock and R. . Hehemann, “The observation of surface relief during the martensitic transformation in TiNi,” *Metallography*, vol. 4, no. 5, pp. 451–456, Oct. 1971.
- [17] X. Wang, S. Kustov, B. Verlinden, and J. Van Humbeeck, “Fundamental Development on Utilizing the R-phase Transformation in NiTi Shape Memory Alloys,” *Shape Mem. Superelasticity*, vol. 1, no. 2, pp. 231–239, Jun. 2015.
- [18] A. P. Jardine, K. H. G. Ashbee, and M. J. Bassett, “Effects of cooling rate on the shape memory effect thermodynamics of NiTi,” *J. Mater. Sci.*, vol. 23, no. 12, pp. 4273–4281, Dec. 1988.
- [19] C. Zamponi, R. L. De Miranda, and E. Quandt, “Superelastic thin films and applications for medical devices,” in *Thin Film Shape Memory Alloys: Fundamentals and Device Applications*, New York, NY: Cambridge University Press, 2009, pp. 370–384.
- [20] A. Czechowicz and S. Langbein, “Introduction to Shape Memory Alloy Technology,” in *Shape Memory Alloy Valves*, Cham: Springer International Publishing, 2015, pp. 23–40.
- [21] N. B. Morgan and C. M. Friend, “Shape Memory Alloys,” in *Smart Technologies*, River Edge, NJ: World Scientific, 2003, pp. 109–139.
- [22] R. Lima de Miranda, C. Zamponi, and E. Quandt, “Micropatterned Freestanding Superelastic TiNi Films,” *Adv. Eng. Mater.*, vol. 15, no. 1–2, pp. 66–69, Feb. 2013.
- [23] X.-B. Yuan, B. Chen, F.-S. Liu, Q. Xu, and W. Ma, “Transformation behaviors

- and superelasticity of Ti<sub>50</sub>Ni<sub>48</sub>Fe<sub>2</sub> shape memory alloy subjected to cold-rolling and subsequent annealing,” *Rare Met.*, vol. 33, no. 6, pp. 652–656, Dec. 2014.
- [24] T. Lehnert, S. Tixier, P. Böni, and R. Gotthardt, “A new fabrication process for Ni–Ti shape memory thin films,” *Mater. Sci. Eng. A*, vol. 273–275, pp. 713–716, Dec. 1999.
- [25] T. Matsunaga, S. Kajiwara, K. Ogawa, T. Kikuchi, and S. Miyazaki, “High strength Ti–Ni-based shape memory thin films,” *Mater. Sci. Eng. A*, vol. 273–275, pp. 745–748, Dec. 1999.
- [26] X.-G. Ma and K. Komvopoulos, “Nanoscale pseudoelastic behavior of indented titanium–nickel films,” *Appl. Phys. Lett.*, vol. 83, no. 18, pp. 3773–3775, Nov. 2003.
- [27] E. O. Nasakina *et al.*, “Preparation of a nanostructured shape-memory composite material for biomedical applications,” *Inorg. Mater.*, vol. 51, no. 4, pp. 400–404, Apr. 2015.
- [28] V. N. Kulkarni, V. N. Gaitonde, V. Hadimani, and V. Aiholi, “Analysis of Wire EDM Process Parameters in Machining of NiTi Superelastic Alloy,” *Mater. Today Proc.*, vol. 5, no. 9, pp. 19303–19312, 2018.
- [29] Y. Kaynak, S. W. Robertson, H. E. Karaca, and I. S. Jawahir, “Progressive tool-wear in machining of room-temperature austenitic NiTi alloys: The influence of cooling/lubricating, melting, and heat treatment conditions,” *J. Mater. Process. Technol.*, vol. 215, pp. 95–104, Jan. 2015.
- [30] L. Hu, Y. Xue, and F. Shi, “Intermetallic formation and mechanical properties of Ni-Ti diffusion couples,” *Mater. Des.*, vol. 130, pp. 175–182, Sep. 2017.
- [31] Y. Zhou, Q. Wang, D. L. Sun, and X. L. Han, “Co-effect of heat and direct current on growth of intermetallic layers at the interface of Ti–Ni diffusion couples,” *J. Alloys Compd.*, vol. 509, no. 4, pp. 1201–1205, Jan. 2011.
- [32] Q. Meng, H. Yang, Y. Liu, and T. Nam, “Compositionally graded NiTi plate prepared by diffusion annealing,” *Scr. Mater.*, vol. 67, no. 3, pp. 305–308, Aug. 2012.
- [33] B.-Y. Li, L.-J. Rong, and Y.-Y. Li, “Anisotropy of dimensional change and its corresponding improvement by addition of TiH<sub>2</sub> during elemental powder

- sintering of porous NiTi alloy,” *Mater. Sci. Eng. A*, vol. 255, no. 1–2, pp. 70–74, Oct. 1998.
- [34] S. M. Green, D. M. Grant, and N. R. Kelly, “Powder Metallurgical Processing of Ni–Ti Shape Memory Alloy,” *Powder Metall.*, vol. 40, no. 1, pp. 43–47, Jan. 1997.
- [35] J. E. Garay, U. Anselmi-Tamburini, and Z. A. Munir, “Enhanced growth of intermetallic phases in the Ni–Ti system by current effects,” *Acta Mater.*, vol. 51, no. 15, pp. 4487–4495, Sep. 2003.
- [36] G. F. Bastin and G. D. Rieck, “Diffusion in the titanium-nickel system: I. occurrence and growth of the various intermetallic compounds,” *Metall. Trans.*, vol. 5, no. 8, pp. 1817–1826, Aug. 1974.
- [37] S. Miyazaki, H. Y. Kim, and H. Cho, “Crystallization of sputter deposited TiNi amorphous thin films,” in *Thin Film Shape Memory Alloys: Fundamentals and Device Applications*, S. Miyazaki, Y. Q. Fu, and W. M. Huang, Eds. Cambridge University Press, 2009, pp. 115–117.
- [38] H. H. Mohd Zaki and J. Abdullah, “The role of CaH<sub>2</sub> in preventing oxidation for the production of single-phase NiTi alloy in solid state,” *J. Alloys Compd.*, vol. 655, pp. 364–371, Jan. 2016.
- [39] G. Chen, K.-D. Liss, and P. Cao, “In situ observation and neutron diffraction of NiTi powder sintering,” *Acta Mater.*, vol. 67, pp. 32–44, Apr. 2014.
- [40] J. Laeng, Z. Wu, Y. Wang, Y. Liu, and H. Yang, “Phase Formation in Ti–Ni Binary System during Solid-State Synthesis,” *Shape Mem. Superelasticity*, vol. 4, no. 3, pp. 351–359, Sep. 2018.
- [41] H. Rumpf, T. Walther, C. Zamponi, and E. Quandt, “High ultimate tensile stress in nano-grained superelastic NiTi thin films,” *Mater. Sci. Eng. A*, vol. 415, no. 1–2, pp. 304–308, Jan. 2006.
- [42] W. J. Buehler, J. V. Gilfrich, and R. C. Wiley, “Effect of Low-Temperature Phase Changes on the Mechanical Properties of Alloys near Composition TiNi,” *J. Appl. Phys.*, vol. 34, no. 5, pp. 1475–1477, 1963.
- [43] A. Behera, S. Aich, A. Behera, and A. Sahu, “Processing and Characterization of Magnetron Sputtered Ni/Ti Thin Film and their Annealing Behaviour to Induce Shape Memory Effect,” *Mater. Today Proc.*, vol. 2, no. 4–5, pp. 1183–1192, 2015.

- [44] D. M. Mattox, "Physical Sputtering and Sputter Deposition (Sputtering)," in *Handbook of Physical Vapor Deposition (PVD) Processing*, Elsevier, 2010, pp. 237–286.
- [45] H. Cho, H. Y. Kim, and S. Miyazaki, "Alloying process of sputter-deposited Ti/Ni multilayer thin films," *Mater. Sci. Eng. A*, vol. 438–440, pp. 699–702, Nov. 2006.
- [46] A. Behera and S. Aich, "Characterisation and properties of magnetron sputtered nanoscale bi-layered Ni/Ti thin films and effect of annealing," *Surf. Interface Anal.*, vol. 47, no. 8, pp. 805–814, Aug. 2015.
- [47] A. Paul, T. Laurila, V. Vuorinen, and S. V. Divinski, *Thermodynamics, Diffusion and the Kirkendall Effect in Solids*. Cham: Springer International Publishing, 2014.
- [48] G. Glodán, C. Cserhádi, I. Beszeda, and D. L. Beke, "Production of hollow hemisphere shells by pure Kirkendall porosity formation in Au/Ag system," *Appl. Phys. Lett.*, vol. 97, no. 11, p. 113109, Sep. 2010.
- [49] R. Talreja and C. V. Singh, *Damage and Failure of Composite Materials*, 1st ed. Cambridge: Cambridge University Press, 2012.
- [50] G. Abadias *et al.*, "Review Article: Stress in thin films and coatings: Current status, challenges, and prospects," *J. Vac. Sci. Technol. A Vacuum, Surfaces, Film.*, vol. 36, no. 2, p. 020801, Mar. 2018.
- [51] Y. Fu and H. Du, "Effects of film composition and annealing on residual stress evolution for shape memory TiNi film," *Mater. Sci. Eng. A*, vol. 342, no. 1–2, pp. 236–244, Feb. 2003.
- [52] V. Teixeira, M. Andritschky, W. Fischer, H. P. Buchkremer, and D. Stöver, "Effects of deposition temperature and thermal cycling on residual stress state in zirconia-based thermal barrier coatings," *Surf. Coatings Technol.*, vol. 120–121, pp. 103–111, Nov. 1999.
- [53] J. W. Hutchinson, "Stresses and Failure Modes in Thin Films and Multilayers," Harvard University, 1996.
- [54] A. N. Khan, J. Lu, and H. Liao, "Heat treatment of thermal barrier coatings," *Mater. Sci. Eng. A*, vol. 359, no. 1–2, pp. 129–136, Oct. 2003.
- [55] F. Bernard, A. El-Bouri, E. Sciora, and N. Gérard, "Residual stresses induced by LiH precipitation in an Al-Li alloy," *J. Alloys Compd.*, vol. 177, no. 2, pp. 245–

249, Dec. 1991.

- [56] V. Sijacki -Zeravcic, M. Rogulic, A. Markovic, and A. Milosavljevic, "Residual Elastic Stresses Dependence on Precipitation and Cold Plastic Deformation in Al-Cu Alloy," in *Residual Stresses III: Science and Technology*, Springer, 1992, pp. 797–802.
- [57] D. A. Porter and K. E. Easterling, *Phase Transformations in Metals and Alloys*. Boston, MA: Springer US, 1992.
- [58] A. C. Fischer-Cripps, *Introduction to Contact Mechanics*, 2nd ed. Springer, 2007.
- [59] S. Y. Chen, T. N. Farris, and S. Chandrasekari, "Contact mechanics of hertzian cone cracking," *Int. J. Solids Struct.*, vol. 32, no. 3–4, 1995.
- [60] D. Louapre and K. Breder, "Hertzian Indentation Stress Field Equations," *Int. J. Appl. Ceram. Technol.*, vol. 12, no. 5, pp. 1071–1079, Sep. 2015.
- [61] A. Pajares, L. Wei, B. R. Lawn, N. P. Padture, and C. C. Berndt, "Mechanical characterization of plasma sprayed ceramic coatings on metal substrates by contact testing," *Mater. Sci. Eng. A*, vol. 208, no. 2, pp. 158–165, Apr. 1996.
- [62] A. C. Fischer-Cripps, B. R. Lawn, A. Pajares, and L. Wei, "Stress Analysis of Elastic-Plastic Contact Damage in Ceramic Coatings on Metal Substrates," *J. Am. Ceram. Soc.*, vol. 79, no. 10, pp. 2619–2625, Aug. 2005.
- [63] H. Chai, "Fracture mechanics analysis of thin coatings under spherical indentation," *Int. J. Fract.*, vol. 119, no. 3, pp. 263–285, 2003.
- [64] R. R. Balokhonov, V. A. Romanova, S. Schmauder, S. A. Martynov, and Z. G. Kovalevskaya, "A mesomechanical analysis of plastic strain and fracture localization in a material with a bilayer coating," *Compos. Part B Eng.*, vol. 66, pp. 276–286, Nov. 2014.
- [65] Y.-G. Jung, S. Wuttiphan, I. M. Peterson, and B. R. Lawn, "Damage Modes in Dental Layer Structures," *J. Dent. Res.*, vol. 78, no. 4, pp. 887–897, Apr. 1999.
- [66] Y. Deng, B. R. Lawn, and I. K. Lloyd, "Characterization of damage modes in dental ceramic bilayer structures," *J. Biomed. Mater. Res.*, vol. 63, no. 2, pp. 137–145, 2002.
- [67] K. S. Lee, S. Wuttiphan, X.-Z. Hu, S. K. Lee, and B. R. Lawn, "Contact-Induced Transverse Fractures in Brittle Layers on Soft Substrates: A Study on Silicon

- Nitride Bilayers,” *J. Am. Ceram. Soc.*, vol. 81, no. 3, pp. 571–580, Jan. 2005.
- [68] H. Chai, “Transverse fracture in thin-film coatings under spherical indentation,” *Acta Mater.*, vol. 53, no. 2, pp. 487–498, Jan. 2005.
- [69] K. S. Lee, S. K. Lee, B. R. Lawn, and D. K. Kim, “Contact Damage and Strength Degradation in Brittle/Quasi-Plastic Silicon Nitride Bilayers,” *J. Am. Ceram. Soc.*, vol. 81, no. 9, pp. 2394–2404, Jan. 2005.
- [70] S. Kumar and W. A. Curtin, “Crack interaction with microstructure,” *Mater. Today*, vol. 10, no. 9, pp. 34–44, Sep. 2007.
- [71] S. S. R. Koloor, A. Abdul-Latif, X. J. Gong, and M. N. Tamin, “Evolution Characteristics of Delamination Damage in CFRP Composites Under Transverse Loading,” 2012, pp. 45–59.
- [72] N. Suh, S. Jahanmir, and E. Abrahamson, “The Delamination Theory of Wear,” 1974.
- [73] B. Bhushan, “Wear,” in *Introduction to Tribology*, New York, NY: Wiley, 2002, pp. 331–410.
- [74] K. G. Budinski, *Friction, Wear, and Erosion Atlas*. CRC Press, 2013.
- [75] G. W. Stachowiak and A. W. Batchelor, *Engineering Tribology*, 4 ed. Oxford, UK: Butterworth-Heinemann, 2013.
- [76] ASM International Handbook Committee, *Friction, Lubrication, and Wear Technology*, Volume 18. Materials Park, OH, 1992.
- [77] J. F. Archard, “Contact and Rubbing of Flat Surfaces,” *J. Appl. Phys.*, vol. 24, no. 8, pp. 981–988, Aug. 1953.
- [78] G. W. Stachowiak and A. W. Batchelor, *Engineering Tribology*. Elsevier, 2014.
- [79] E. Bousser, L. Martinu, and J. E. Klemberg-Sapieha, “Solid particle erosion mechanisms of protective coatings for aerospace applications,” *Surf. Coatings Technol.*, vol. 257, pp. 165–181, Oct. 2014.
- [80] M. Antonov, I. Hussainova, F. Sergejev, P. Kulu, and A. Gregor, “Assessment of gradient and nanogradient PVD coatings behaviour under erosive, abrasive and impact wear conditions,” *Wear*, vol. 267, no. 5–8, pp. 898–906, Jun. 2009.
- [81] P. Wieceński, J. Smolik, H. Garbacz, and K. J. Kurzydłowski, “Failure and deformation mechanisms during indentation in nanostructured Cr/CrN multilayer

- coatings,” *Surf. Coatings Technol.*, vol. 240, pp. 23–31, Feb. 2014.
- [82] G. Skordaris, K.-D. Bouzakis, and P. Charalampous, “A dynamic FEM simulation of the nano-impact test on mono- or multi-layered PVD coatings considering their graded strength properties determined by experimental–analytical procedures,” *Surf. Coatings Technol.*, vol. 265, pp. 53–61, Mar. 2015.
- [83] M. Berger, U. Wiklund, M. Eriksson, H. Engqvist, and S. Jacobson, “The multilayer effect in abrasion — optimising the combination of hard and tough phases,” *Surf. Coatings Technol.*, vol. 116–119, pp. 1138–1144, Sep. 1999.
- [84] S. G. Warrier, B. S. Majumdar, and D. B. Miracle, “Interface effects on crack deflection and bridging during fatigue crack growth of titanium matrix composites,” *Acta Mater.*, vol. 45, no. 12, pp. 4969–4980, Dec. 1997.
- [85] R. O. Ritchie, R. H. Dauskardt, and K. T. Venkateswara Rao, “Fatigue-crack propagation behavior in monolithic and composite ceramics and intermetallics,” *Mater. Sci.*, vol. 30, no. 3, pp. 277–300, 1995.
- [86] M. Barchiesi, “Toughening by Crack Deflection in the Homogenization of Brittle Composites with Soft Inclusions,” *Arch. Ration. Mech. Anal.*, vol. 227, no. 2, pp. 749–766, Feb. 2018.
- [87] J. Hou, Q. Li, J. Lv, and H. Zuo, “Crack deflection by the transformable particles dispersed in composites,” *Acta Mech.*, vol. 227, no. 3, pp. 743–756, Mar. 2016.
- [88] J. Watts and G. Hilmas, “Crack deflection in tungsten carbide based laminates,” *Int. J. Refract. Met. Hard Mater.*, vol. 24, no. 3, pp. 222–228, May 2006.
- [89] L. Ma, “Fundamental formulation for transformation toughening,” *Int. J. Solids Struct.*, vol. 47, no. 22–23, pp. 3214–3220, Nov. 2010.
- [90] R. H. J. Hannink, P. M. Kelly, and B. C. Muddle, “Transformation Toughening in Zirconia-Containing Ceramics,” *J. Am. Ceram. Soc.*, vol. 83, no. 3, pp. 461–487, Dec. 2004.
- [91] H. Tsukamoto, “Design against fracture of functionally graded thermal barrier coatings using transformation toughening,” *Mater. Sci. Eng. A*, vol. 527, no. 13–14, pp. 3217–3226, May 2010.
- [92] K. T. Faber, T. Iwagoshi, and A. Ghosh, “Toughening by Stress-Induced Microcracking in Two-Phase Ceramics,” *J. Am. Ceram. Soc.*, vol. 71, no. 9, pp. C-

- 399-C-401, Sep. 1988.
- [93] R. Neupane and Z. Farhat, "Wear and dent resistance of superelastic TiNi alloy," *Wear*, vol. 301, no. 1-2, pp. 682-687, Apr. 2013.
- [94] J. P. Singh, D. P. H. Hasselman, W. M. Su, J. A. Rubin, and R. Palicka, "Observations on the nature of micro-cracking in brittle composites," *J. Mater. Sci.*, vol. 16, no. 1, pp. 141-150, Jan. 1981.
- [95] D. . Li, "A new type of wear-resistant material: pseudo-elastic TiNi alloy," *Wear*, vol. 221, no. 2, pp. 116-123, Oct. 1998.
- [96] Y. N. Liang, S. Z. Li, Y. B. Jin, W. Jin, and S. Li, "Wear behavior of a TiNi alloy," *Wear*, vol. 198, no. 1-2, pp. 236-241, Oct. 1996.
- [97] Z. Farhat and C. Zhang, "On the Deformation of Superelastic TiNi Alloy," *Tribol. Lett.*, vol. 37, no. 2, pp. 169-173, Feb. 2010.
- [98] Y. Zhang, Y.-T. Cheng, and D. S. Grummon, "The influence of superelastic NiTi interlayers on tribological properties of CrN hard coatings," *Mater. Sci. Eng. A*, vol. 438-440, pp. 710-713, Nov. 2006.
- [99] Y. Zhang, Y.-T. Cheng, and D. S. Grummom, "Novel tribological systems using shape memory alloys and thin films," *Surf. Coatings Technol.*, vol. 202, no. 4-7, pp. 998-1002, Dec. 2007.
- [100] H. C. Lin, J. L. He, K. C. Chen, H. M. Liao, and K. M. Lin, "Wear characteristics of TiNi shape memory alloys," *Metall. Mater. Trans. A*, vol. 28, no. 9, pp. 1871-1877, Sep. 1997.
- [101] R. Liu and D. Y. Li, "Experimental studies on tribological properties of pseudoelastic TiNi alloy with comparison to stainless steel 304," *Metall. Mater. Trans. A*, vol. 31, no. 11, pp. 2773-2783, Nov. 2000.
- [102] S. I. Shah, G. H. Jaffari, E. Yassitepe, and B. Ali, "Evaporation: Processes, Bulk Microstructures, and Mechanical Properties," in *Handbook of Deposition Technologies for Films and Coatings*, Elsevier, 2010, pp. 135-252.
- [103] P. S. Prevey, "X-Ray Diffraction Residual Stress Techniques," *Met. Handb.*, vol. 10, pp. 380-392, 1986.
- [104] W. C. Oliver and G. M. Pharr, "An improved technique for determining hardness and elastic modulus using load and displacement sensing indentation

- experiments,” *J. Mater. Res.*, vol. 7, no. 06, pp. 1564–1583, Jun. 1992.
- [105] A. C. Fischer-Cripps, *Nanoindentation*. Springer, 2002.
- [106] “CES EduPack.” Cambridge, 2017.
- [107] H. Cho and S. Miyazaki, “TiNi multilayer thin films,” in *Thin Film Shape Memory Alloys: Fundamentals and Device Applications*, S. Miyazaki, Y. Q. Fu, and W. M. Huang, Eds. New York, NY: Cambridge University Press, 2009, pp. 110–123.
- [108] N. Hatcher, O. Y. Kontsevoi, and A. J. Freeman, “Role of elastic and shear stabilities in the martensitic transformation path of NiTi,” *Phys. Rev. B*, vol. 80, no. 14, p. 144203, Oct. 2009.
- [109] ASM International Handbook Committee, *Properties and Selection: Nonferrous Alloys and Special-Purpose Materials*, 9th ed. Metals Park, Ohio: ASM International, 1990.
- [110] V. Teixeira, “Residual stress and cracking in thin PVD coatings,” *Vacuum*, vol. 64, no. 3–4, pp. 393–399, Jan. 2002.
- [111] Y. Q. Fu, W. M. Huang, M. Cai, and S. Zhang, “Stress and surface morphology evolution,” in *Thin Film Shape Memory Alloys*, S. Miyazaki, Y. Q. Fu, and W. M. Huang, Eds. Cambridge: Cambridge University Press, 2009, pp. 166–192.
- [112] F. Kahleyss *et al.*, “Processing and Damping Properties of Sputtered NiTi Thin Films for Tools in Machining Processes,” *J. Mater. Eng. Perform.*, vol. 20, no. 4–5, pp. 500–505, Jul. 2011.
- [113] C. Walter, T. Antretter, R. Daniel, and C. Mitterer, “Finite element simulation of the effect of surface roughness on nanoindentation of thin films with spherical indenters,” *Surf. Coatings Technol.*, vol. 202, no. 4–7, pp. 1103–1107, Dec. 2007.
- [114] S. L. Lehoczky, “Retardation of Dislocation Generation and Motion in Thin-Layered Metal Laminates,” *Phys. Rev. Lett.*, vol. 41, no. 26, pp. 1814–1818, Dec. 1978.
- [115] A. Kelly, F. E. Buresch, and R. H. Biddulph, “Composites for the 1990s [and Discussion],” *Philos. Trans. R. Soc. A Math. Phys. Eng. Sci.*, vol. 322, no. 1567, pp. 409–423, Jul. 1987.
- [116] J. S. Koehler, “Attempt to Design a Strong Solid,” *Phys. Rev. B*, vol. 2, no. 2, pp. 547–551, Jul. 1970.

- [117] Z. N. Farhat and C. Zhang, "The Role of Reversible Martensitic Transformation in the Wear Process of TiNi Shape Memory Alloy," *Tribol. Trans.*, vol. 53, no. 6, pp. 917–926, Oct. 2010.
- [118] G.-S. Lee, S.-H. Bae, and Y.-Z. Lee, "The influence of formation of transfer layer on the characteristics of friction and wear mechanism between several coatings and anodized aluminum alloy," *Surf. Coatings Technol.*, vol. 205, pp. S152–S157, Dec. 2010.
- [119] S. Koloor, A. Sbdul-latif, X. Gong, and M. Tamin, *Damage and Fracture of Composite Materials and Structures*, vol. 17. Berlin, Heidelberg: Springer Berlin Heidelberg, 2012.
- [120] D. Lesuer, C. Syn, O. Sherby, J. Wadsworth, and J. Lewandowski, "Mechanical Behavior of Laminated Metal Composites," *Int. Mater. Rev.*, vol. 41, no. 5, pp. 196–197, 1996.
- [121] L. M. Yang *et al.*, "Cavitation erosion resistance of NiTi thin films produced by Filtered Arc Deposition," *Wear*, vol. 267, no. 1–4, pp. 233–243, Jun. 2009.
- [122] J. Cheng, N. Zhang, L. Wei, H. Mi, and Y. Dou, "A New Phenomenological Model for Single Particle Erosion of Plastic Materials," *Materials (Basel)*, vol. 12, no. 1, p. 135, Jan. 2019.
- [123] A. Almotairi, A. Warkentin, and Z. Farhat, "Mechanical damage of hard chromium coatings on 416 stainless steel," *Eng. Fail. Anal.*, vol. 66, pp. 130–140, Aug. 2016.
- [124] C. Wang, "Indentation and Fracture Behaviour of Electroless Ni-P-based Composite Coatings," Dalhousie Univerity, 2017.

## 7.0 Appendix A – Nanoindentation Data

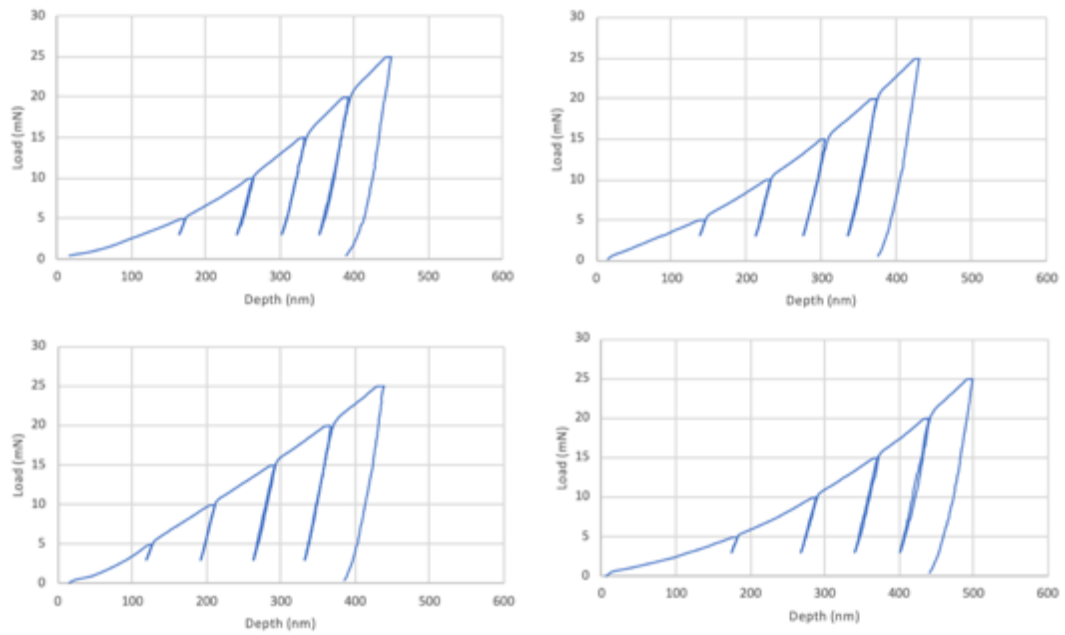


*Figure 7.1 – As-sputtered load-depth curves*

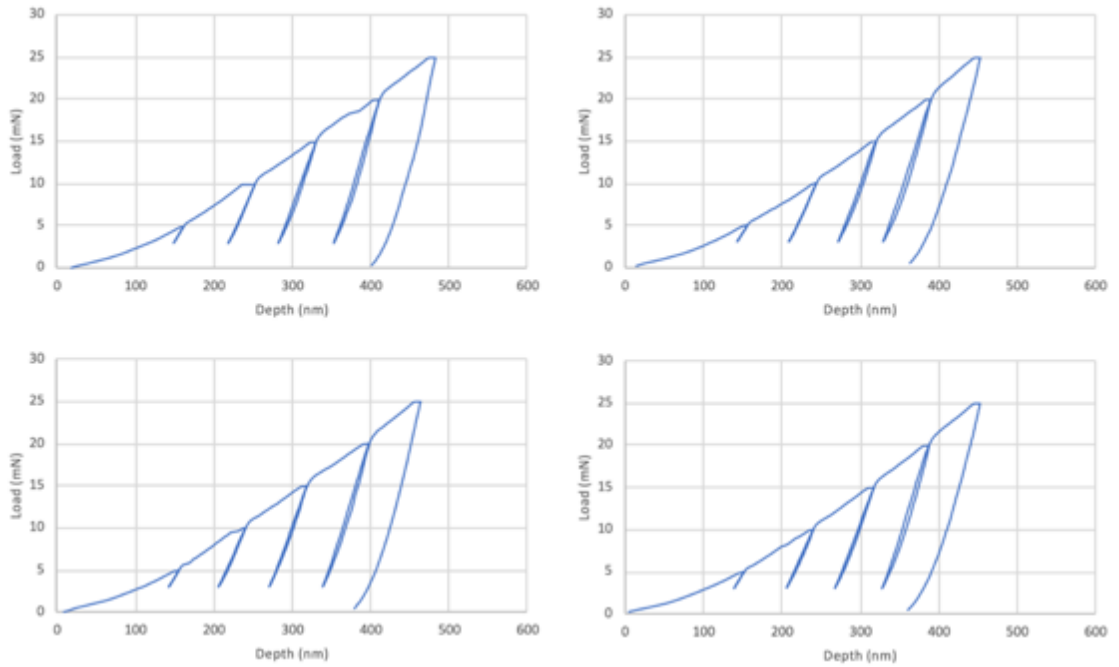


*Figure 7.2 – 650°C load-depth curves*

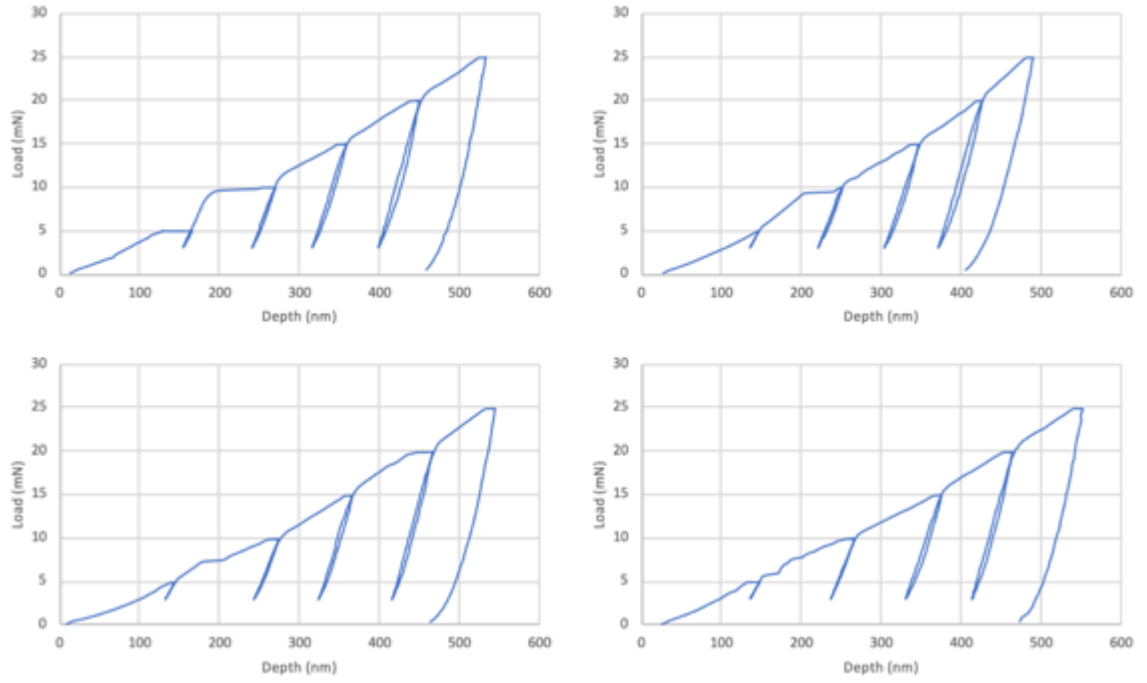


**Figure 7.3 – 800°C load-depth curves**

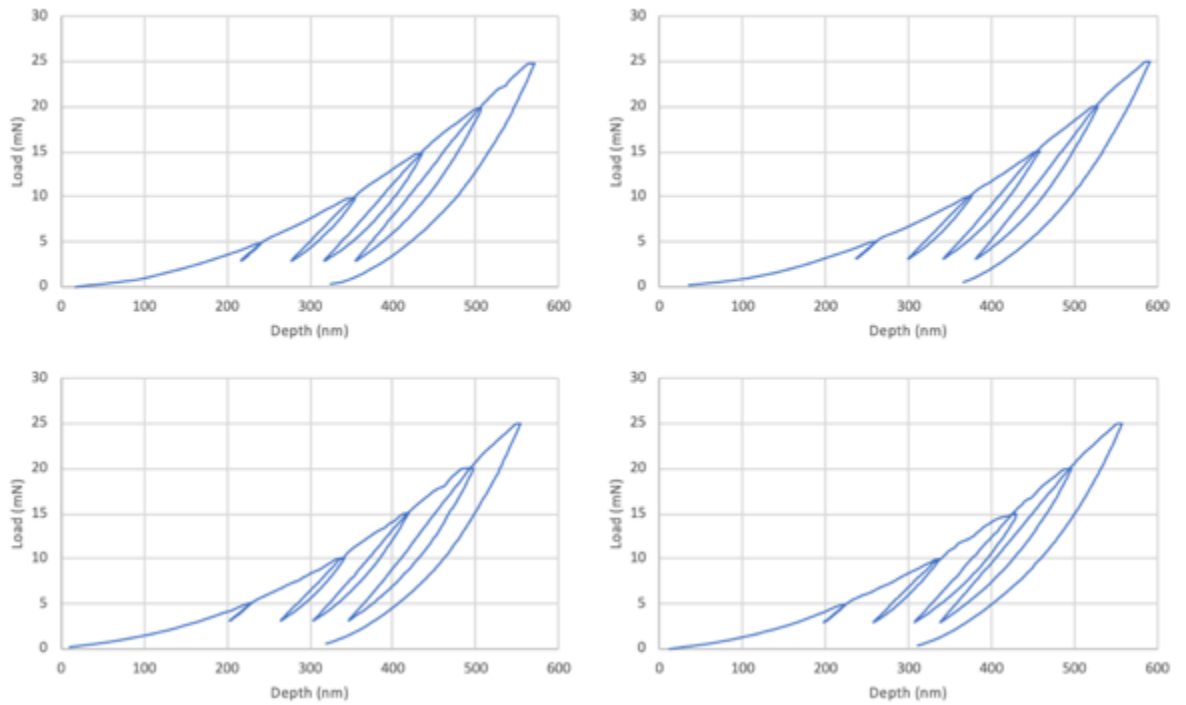


**Figure 7.4 – Superelastic NiTi load-depth curves**

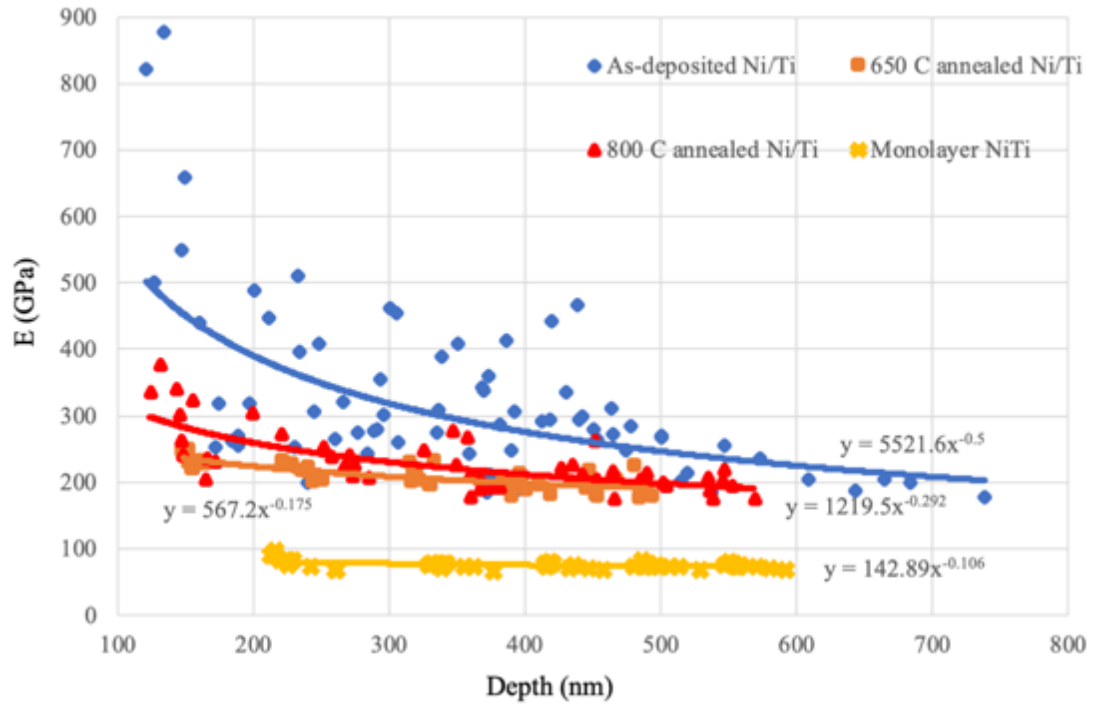


**Figure 7.5 – Elastic Modulus values for as-sputtered, 650 °C, and 800 °C nanolaminates and superelastic NiTi monolayer**

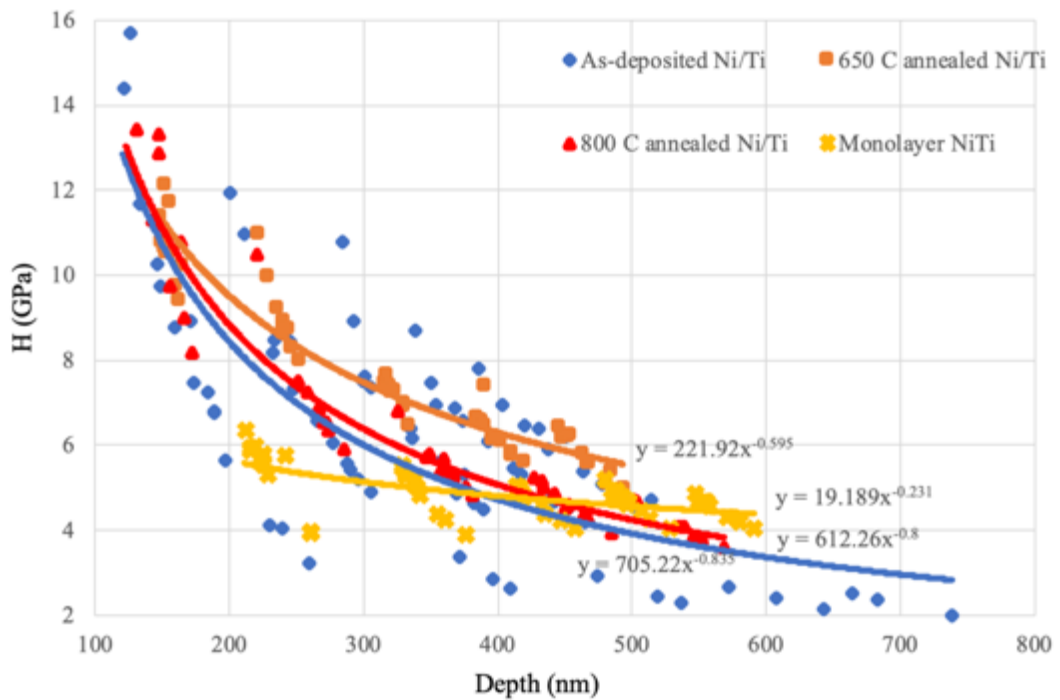


**Figure 7.6 – Hardness values for as-sputtered, 650 °C, and 800 °C nanolaminates and superelastic NiTi monolayer**

## 8.0 Appendix B – Scratch Test Scars

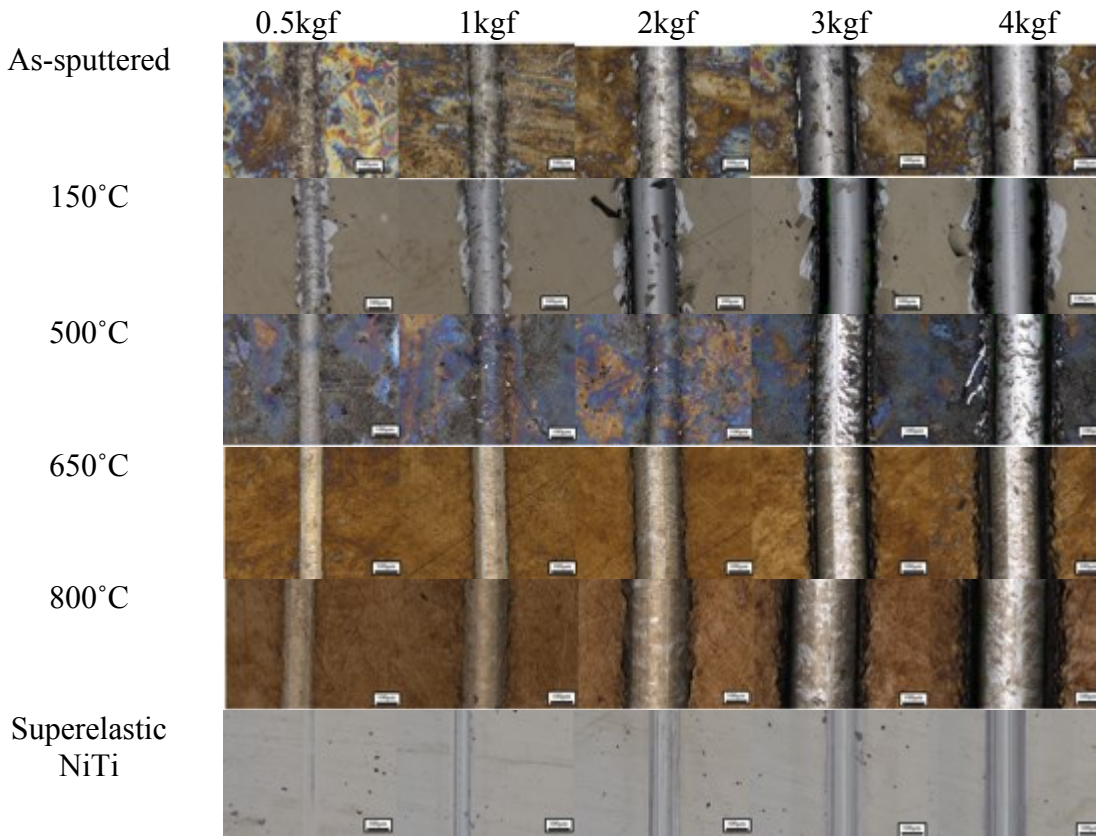


*Figure 8.1 – Single pass scars*

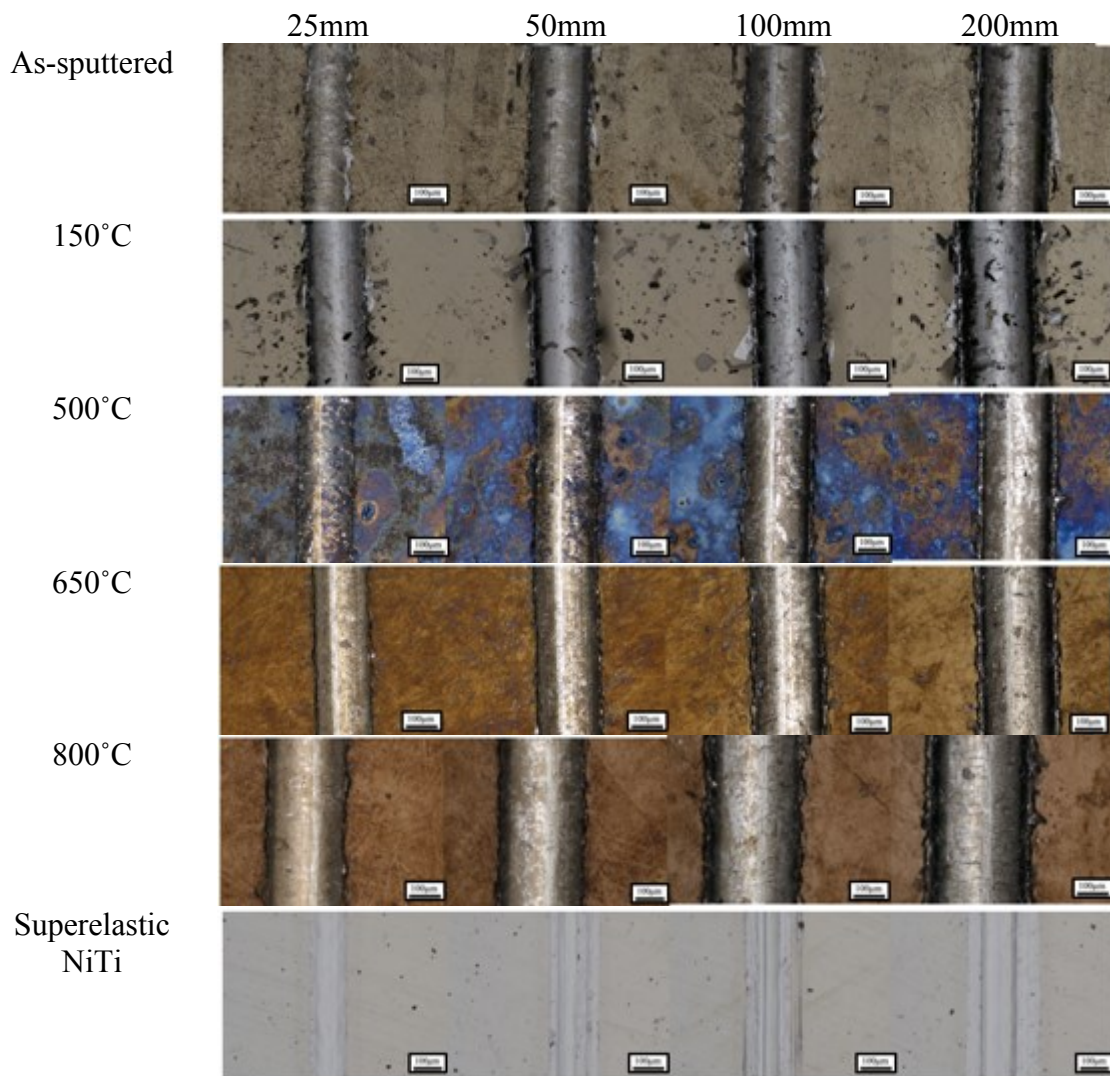


*Figure 8.2 – Multiple pass scars*

## 9.0 Appendix C – Hertzian Type Indents

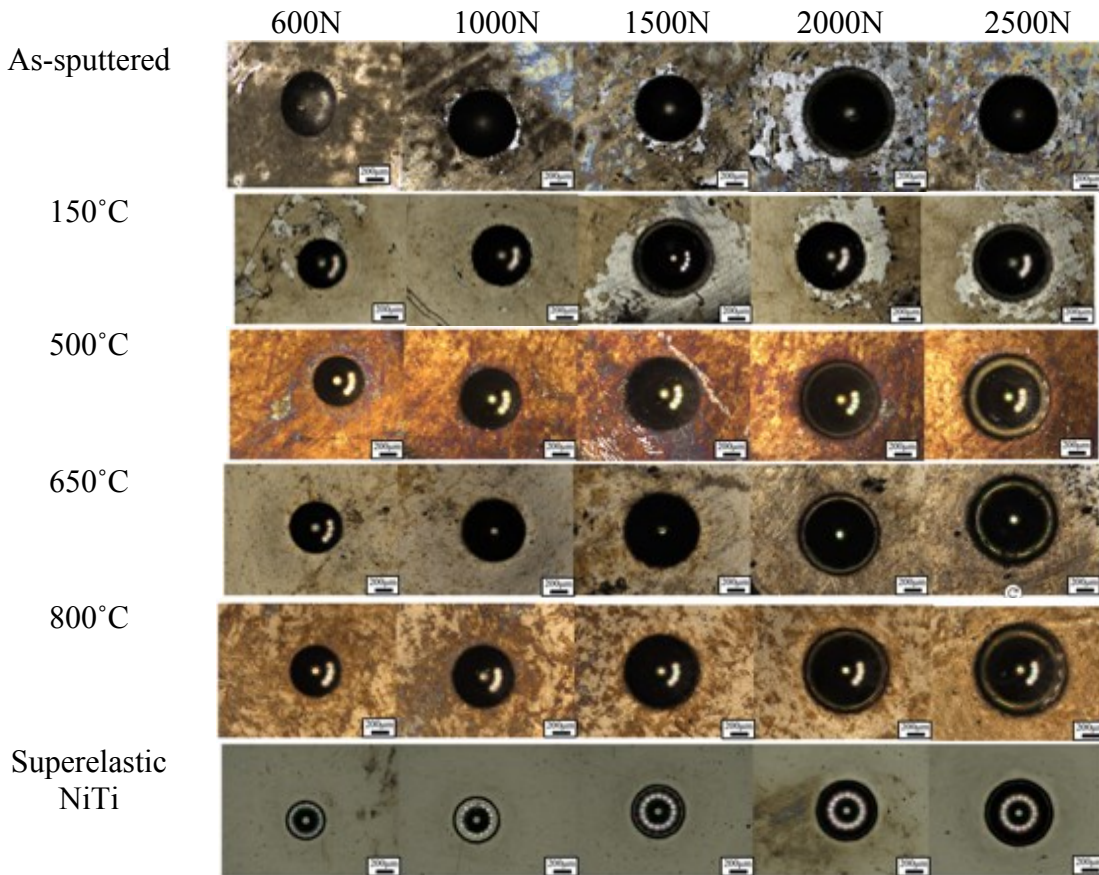


*Figure 9.1 – Hertzian indentations*

## 10.0 Appendix D – Single Particle Erosion

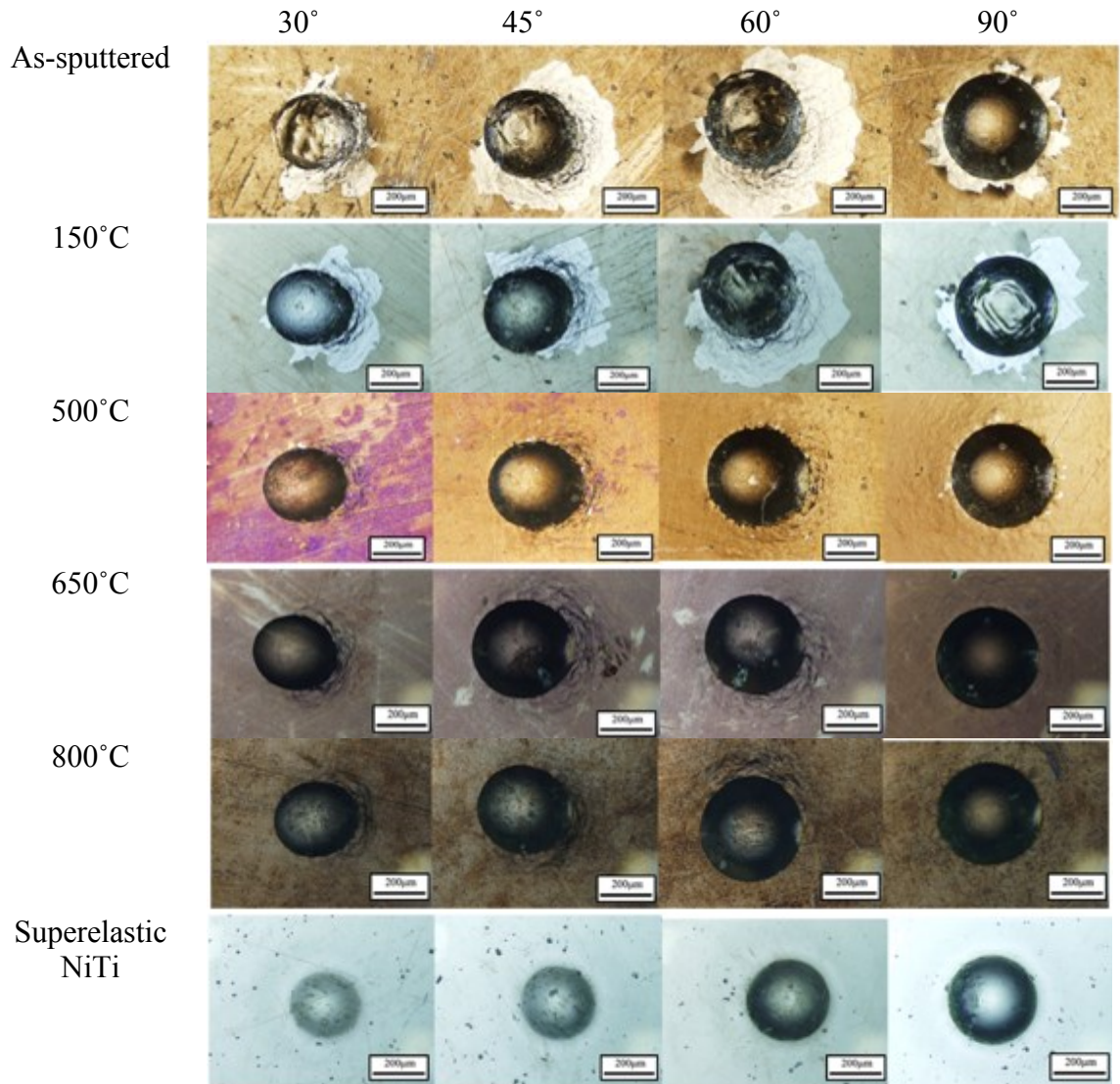


*Figure 10.1 – Single particle impact sites*